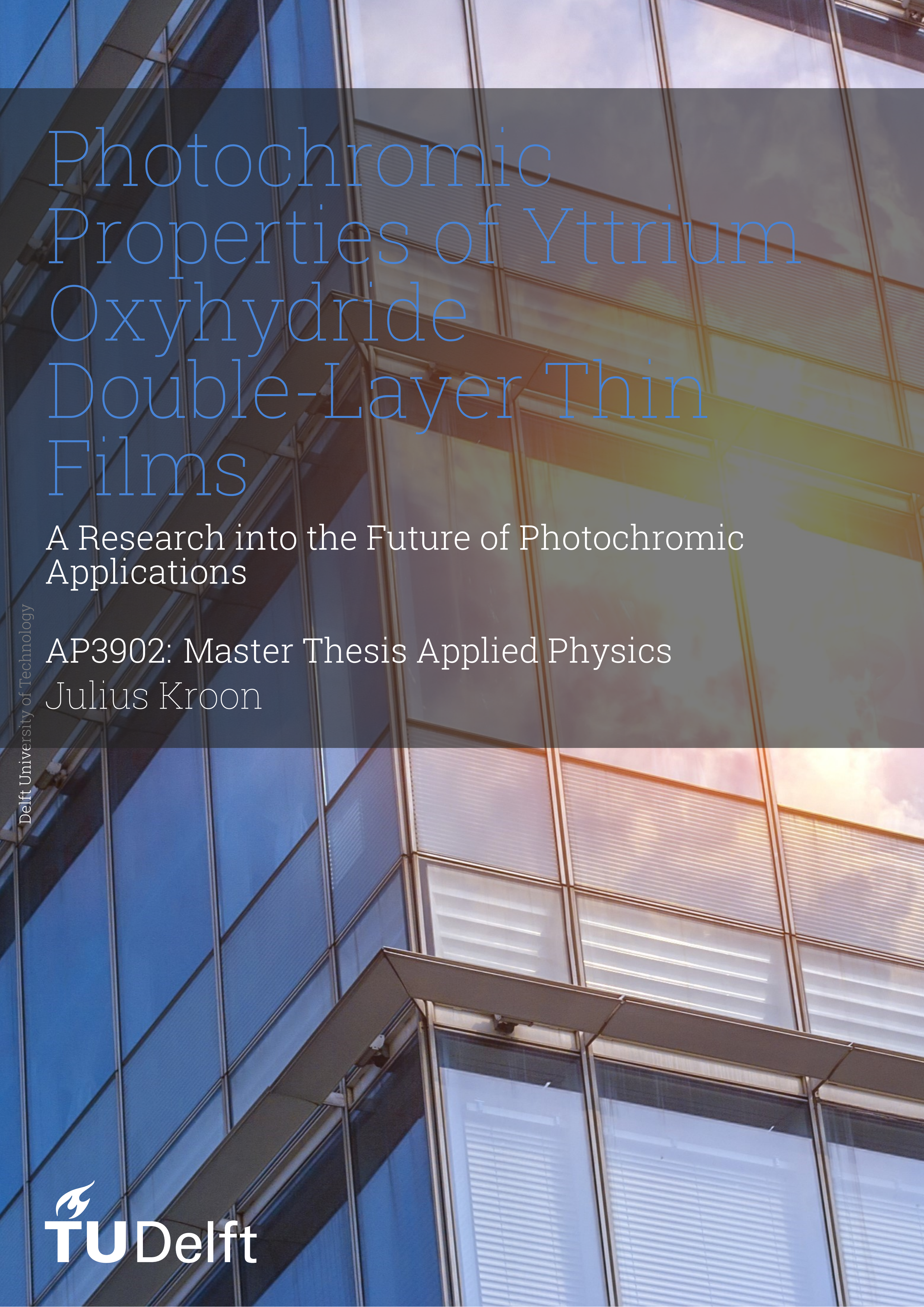

Photochromic Properties of Yttrium Oxyhydride Double-Layer Thin Films

A Research into the Future of Photochromic Applications

AP3902: Master Thesis Applied Physics

Julius Kroon

Delft University of Technology

Photochromic Properties of Yttrium Oxyhydride Double-Layer Thin Films

A Research into the Future of Photochromic Applications

by

Julius Kroon

to obtain the degree of Master of Science

at the Delft University of Technology,

to be defended at 14:30 on February 21st, 2025 in the Kronigzaal, building 58 (Applied Sciences) room A2.010

Student number:	4889282	
Project duration:	July 1, 2024 – February 14, 2025	
Thesis committee:	Dr. S.W.H. Eijt	TU Delft, supervisor
	Em.prof.dr. B. Dam	TU Delft
	Dr. H. Schut	TU Delft
Daily supervisor:	Dr. Z. Wu	TU Delft

TU Delft

Abstract

Photochromic materials, which exhibit reversible changes in transparency upon light exposure, have gained significant interest for their potential applications in smart window technologies. Among these materials, yttrium oxyhydride (YOH) stands out due to its stability and promising photochromic properties. A critical challenge in developing practical photochromic windows lies in balancing two key properties: high photochromic contrast (ΔT) and short bleaching time (τ_B). These properties are strongly influenced by the pressure during the thin film's deposition. This study investigates how thicker YOH films deposited at higher pressures (0.8Pa) affect photochromic performance and explores the impact of combining two layers in double-layer configurations to optimize the Photochromic properties.

YOH thin films were prepared using reactive DC magnetron sputtering at two deposition pressures: 0.5Pa and 0.8Pa. Single-layer samples were deposited at 0.8Pa with varying thicknesses (400nm, 600nm, and 800nm), while double-layer samples were created by stacking layers deposited at different pressures in two configurations: substrate/0.8Pa/0.5Pa (DL-1) and substrate/0.5Pa/0.8Pa (DL-2). The optical and structural properties of these films were characterized using a combination of transmission and reflection measurements, spectroscopic ellipsometry, X-ray diffraction (XRD), and Doppler Broadening Positron Annihilation Spectroscopy (DB-PAS). These techniques provided insights into the relationship between the material's oxidation state, atomic structure, and photochromic response.

The results revealed that single-layer films deposited at 0.8Pa exhibited lower photochromic contrast (11.4 ± 0.4% for 400nm) but faster bleaching time constants (0.6 hours) compared to those deposited at 0.5Pa, which achieved higher contrast (53.0 ± 0.4%) but slower bleaching time constants (5.1 hours). This trade-off aligns with previous findings, confirming the inverse relationship between deposition pressure and photochromic performance. While thicker films (600nm and 800nm) at 0.8Pa showed increased photochromic contrast, the 800nm sample suffered from inhomogeneity and a lower-than-expected contrast, highlighting the challenges of scaling up film thickness for practical applications.

In double-layer configurations, the properties of the bottom layer significantly influenced the overall photochromic performance. The DL-1 sample, with a 0.8Pa bottom layer, exhibited increased oxidation and inhomogeneity in the 0.5Pa top layer, resulting in a reduced photochromic contrast of 29.7 ± 0.4% and significantly lower transparent transmission (31.6 ± 0.2%). In contrast, the DL-2 sample, with a 0.5Pa bottom layer, allowed the 0.8Pa top layer to retain its intrinsic photochromic properties, achieving a contrast of 55.2 ± 0.4%, closely matching theoretical predictions of ≈52%. XRD measurements further supported these findings, showing a lattice constant increase of 0.026 ± 0.005Å in the DL-1 sample compared to 0.5Pa single-layer thin films, indicative of higher oxygen incorporation in the top layer. Additionally, both double-layer samples exhibited longer bleaching time constants compared to their respective bottom layers, suggesting that the capping of the bottom layer may influence hydrogen mobility within the film.

This study underscores the critical role of deposition pressure, film thickness, and layer sequencing in determining the photochromic properties of YOH thin films. Higher deposition pressures and thicker films lead to increased porosity and inhomogeneity, which can degrade photochromic performance. Additionally, careful control of layer stacking, particularly by using a less porous bottom layer (e.g., 0.5Pa), can result in a photochromic contrast similar to the stacking of layers. However, the bleaching time constant in negatively impacted.

Contents

Abstract i

1 Introduction 1

2 Theory 3

- 2.1 Optics 3
  - 2.1.1 Transmission, Reflection, and Absorption 3
  - 2.1.2 Snell's Law 4
- 2.2 Photochromic Effect 4
  - 2.2.1 Photochromic Contrast 4
  - 2.2.2 Bleaching Time Constant 6
  - 2.2.3 Memory Effect 7
  - 2.2.4 Darkening Time Constant 7
- 2.3 Rare-Earth Oxyhydrides 8
  - 2.3.1 Structure 9
  - 2.3.2 Properties and Differences 9
- 2.4 Bandgap 11
  - 2.4.1 Direct and Indirect Bandgap 11
  - 2.4.2 Burstein-Moss Effect 12
  - 2.4.3 Tauc Method 12
- 2.5 Proposed Mechanism 13
  - 2.5.1 H-rich Metallic Domains 13
  - 2.5.2 Anderson-Mott Insulator-to-Metal Transition 13
- 2.6 Electrodynamics 14
  - 2.6.1 Electromagnetic Radiation 14
  - 2.6.2 Interference 14
  - 2.6.3 Photon Flux 15
  - 2.6.4 Brewster Angle 15
- 2.7 Atomic Interaction 16
  - 2.7.1 Electron–Positron Annihilation 16
  - 2.7.2 Bragg's Law 17

3 Sample Deposition 19

- 3.1 Sample Parameters 19
- 3.2 Reactive DC Magnetron Sputtering 19
- 3.3 Deposited Samples 20

4 Experimental Methods 22

- 4.1 UV illumination 22
- 4.2 Optical Measurements 22
  - 4.2.1 Setup 22
  - 4.2.2 Data analysis 22
- 4.3 Spectroscopic Ellipsometry 23
  - 4.3.1 Setup 23
  - 4.3.2 Data analysis 23
- 4.4 X-Ray Diffraction 24
  - 4.4.1 Setup 25
  - 4.4.2 Data analysis 25
- 4.5 Doppler Broadening Positron Annihilation Spectroscopy 25
  - 4.5.1 Setup 26

4.5.2 Data analysis 26

5 Results 28

5.1 Optical Measurements 28
5.1.1 Single-layer Optical Measurements 28
5.1.2 Double-layer Optical Measurements 34
5.2 Spectroscopic Ellipsometry 39
5.2.1 Substrate 39
5.2.2 Single-layer Spectroscopic Ellipsometry 39
5.2.3 Double-layer Spectroscopic Ellipsometry 45
5.3 X-Ray Diffraction 50
5.3.1 Single-layer XRD 50
5.3.2 Double-layer XRD 51
5.4 Doppler Broadening Positron Annihilation Spectroscopy 54
5.4.1 Double-layer DB-PAS 54

6 Discussion 58

7 Conclusion 64

8 Recommendations 66

A Appendix: Optical Measurements 70

A.1 Bleaching Time Constant 70
A.2 Darkening Time Constant 73
A.3 Tauc Plots 74
A.4 Three Cycle Illumination 80
A.5 Multiple Cycle Illumination 82
A.6 Absorption coefficient 83
A.7 Measurement data 84

B Appendix: Spectroscopic Ellipsometry 86

B.1 CompleteEASE Software fit 86
B.2 Absorption coefficient 89
B.3 Measurement data 90

C Appendix: Doppler Broadening Positron Annihilation Spectroscopy 92

C.1 Fractional contribution 92
C.2 Count rate measurements 93

D Appendix: X-Ray Diffraction 94

D.1 Rietveld Refinement 94

1

Introduction

In the 1960s, researchers began exploring the photochromic effects of silver halide-doped glasses. Photochromic behaviour implies a reversible reduction in a thin film's transparency when exposed to light. This effect can be helpful in day-to-day applications, and while it is already used in sunglasses, large surface applications, such as windows, have proven difficult [31].

In the last 15 years, rare-earth (RE) metals, such as scandium (Sc), yttrium (Y), and the lanthanide group, have been researched as potential solutions for large-scale photochromic applications instead of silver halide-doped glasses. Particularly, the oxyhydride compounds of these RE metals are suitable, with their relative stability and performance under varying environmental conditions [31]. This research focuses on yttrium oxyhydride (YO_xH_{3-2x}), hereafter referred to as YOH, which is a promising coating material due to its high bandgap (ranging from 2.6eV [27] to 5.6eV [54]) and significant photochromic contrast.

Most YOH thin films discussed in the literature are prepared using reactive magnetron sputtering of yttrium at room temperature with argon and hydrogen gases in the chamber [27, 12, 38]. Initially, a YH_2 layer forms on the substrate. This layer undergoes oxidation when exposed to air, transforming from opaque YH_2 to transparent YOH. The oxidation process runs over an extended period. A significant increase in transparency is often observed within the first few minutes, after which the film oxidises more slowly over a more extended period. It is only after several days or even weeks that this oxidation stabilises.

The pressure during the deposition process greatly influences the final oxidation state and, consequently, the transparency of the film. The films are less porous at low pressures, limiting the oxidation process. On the other hand, films deposited at higher pressures show higher transparency due to increased porosity [31] and, consequently, increased oxidation. Research indicates that for optimal photochromic effects, the YOH layer should be deposited at pressures just above the critical pressure, which is 0.4Pa for YOH [35]. The strength of the photochromic effect is mainly expressed through photochromic contrast (ΔT), which is the difference in transparency before and after illumination. This contrast is highest at pressures just above the critical pressure and declines with increasing pressure. The photochromic effect also depends on the thickness of the YOH layers. Thicker films provide greater photochromic contrast, making them advantageous for photochromic applications, whereas thinner films, though more transparent, offer limited contrast [31]. Moreover, the bleaching time constant (τ_B), the time it takes for the photochromic layer to return to full transparency after illumination, also depends on the deposition pressure. Research by Colombi et al. [9] has demonstrated a direct correlation between the O:H ratio and τ_B. This research showed that τ_B decreased with higher deposition pressure.

Given the above, the overall photochromic contrast of YOH layers is highest just above the critical deposition pressure. Extensive research has been conducted on these layers at a deposition pressure of 0.5Pa. As already mentioned, it has been observed that the bleaching time constant (τ_B) depends on this pressure, decreasing at higher values. For practical surface applications of YOH on windows, a lower τ_B is desirable, as a rapid transition between the photo-darkened and bleaching states is necessary for real-world applications. This presents a dilemma where we must choose between a high photochromic contrast (ΔT) or a shorter bleaching time constant (τ_B) when choosing the deposition pressure.

Previous research by Montero-Amenedo [31] has demonstrated that layer thickness also affects photochromic contrast, which increases with thicker layers. This thesis addresses the previously stated dilemma by investigating the impact of an increased deposition pressure combined with thicker layers. Specifically, this paper will examine the photochromic contrast and bleaching time constant of YOH layers at a deposition pressure of 0.8Pa. At this pressure, the bleaching time is expected to decrease compared to the 0.5Pa thin films. By increasing the layer thickness, we aim to mitigate the initially lower photochromic contrast observed at higher pressures.

Following this, we will deposit double-layers of YOH, which will then be investigated. We ensure optimal oxidation throughout the YOH layer by allowing the first layer to oxidise before depositing the second layer. It also promotes the analysis of the results since it allows us to measure the first layer separately. This approach is expected to provide a thin film with greater transparency than a single deposition while keeping the enhanced photochromic contrast associated with thicker layers. Additionally, by varying the deposition pressure between the two layers, we will investigate if achieving both higher photochromic contrast and shorter bleaching time in the same sample is possible and whether interaction takes place between the two layers.

2

Theory

2.1. Optics

Understanding the principles of optics is necessary to understanding the photochromic effect, which describes the interaction between light and a material. Important topics include the transmission, reflection, and absorption of light, which allow us to describe the most important characteristics of a photochromic material.

2.1.1. Transmission, Reflection, and Absorption

When light interacts with a material, it can be transmitted (T), reflected (R) or absorbed (A). Each of these cases is expressed by a parameter which indicates the fraction of the light that undergoes one of the mentioned interactions. Given that these are the only possibilities for light interacting with a material, the sum of the transmission, reflection, and absorption parameters equals 1, or 100%. As can be seen in equation 2.1 [1].

$$T + R + A = 1 \tag{2.1}$$

The transmittance parameter defines the fraction of light that passes through a material. It is defined as the ratio between transmitted light (I_t) and incident light (I_0). A high value for the transmittance parameter would indicate a transparent material since a high percentage of light passes through.

The reflectance parameter is close to the opposite of the transmittance parameter and is given by the ratio between reflected light (I_r), and incident light (I_0). Materials with high reflectance, such as mirrors or polished metals, reflect a substantial portion of the incident light.

The absorption parameter shows how a material absorbs light and converts it to other energies, usually heat [37]. This is quantified by the absorption coefficient ($\alpha(\lambda, t)$), which depends on the material of the object and the wavelength of incident light. This formula and the formulas for transmission and reflection can be found in equation 2.2 [25].

$$T(\lambda, t) = \frac{I_t}{I_0} \qquad R(\lambda, t) = \frac{I_r}{I_0} \qquad A(\lambda, t) = 1 - e^{-\alpha(\lambda, t) \cdot d} \tag{2.2}$$

The transmitted light decreases exponentially as it passes through the material. The Beer-Lambert law (formula 2.3) describes the relationship between incident light, the absorption coefficient ($\alpha(\lambda, t)$) and material thickness (d).

$$I_t = I_0 e^{-\alpha(\lambda, t) \cdot d} \tag{2.3}$$

However, in our samples, a portion of the light will be reflected before entering the thin film. We thus have the account for this in the formula and rewrite to the following form:

$$T(\lambda, t) = (1 - R(\lambda, t))e^{-\alpha(\lambda,t)\cdot d} \tag{2.4}$$

2.1.2. Snell's Law

When light passes through a medium, the wave will bend upon transition from one medium to another with a different refractive index (n). Such bending, i.e. the change in the transmitted angle (θ_t), is described by Snell's Law [1]:

$$n_i sin(\theta_i) = n_t sin(\theta_t) \tag{2.5}$$

The speed of the light wave changes when entering a new medium at some angle, as the change in speed depends on differences between the refractive indices of the two media. A change in speed causes the light wave to bend. The amount of bending will be determined by the refractive indices and angles of incidence involved.

Suppose the light is incident from a medium with a higher refractive index onto a medium with a lower refractive index. In that case, there is a possible outcome that the incident light may be reflected entirely. The largest angle for which the light wave will propagate through the interface called the critical angle of total internal reflection, $\theta_{i,crit}$, can be evaluated from:

$$\theta_{i,crit} = arcsin(\frac{n_i}{n_t}) \tag{2.6}$$

2.2. Photochromic Effect

The photochromic effect is the reversibly changing transparency of a material after illumination. When exposed to light, a photochromic material darkens—a process referred to as photo-darkening. The effect is reversed when the light source is removed, and the material turns transparent again by bleaching.

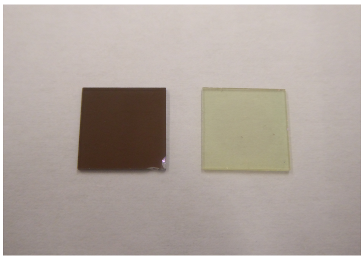

Figure 2.1: Comparison of transparency in double-layer samples. The left sample has undergone illumination for 2.5 hours, resulting in a significant change in its optical properties compared to the unilluminated sample on the right.

To compare different photochromic thin film depositions, we will have to investigate characteristics important in real-life applications. These characteristics include the photochromic contrast and the bleaching time constant.

2.2.1. Photochromic Contrast

The photochromic contrast (ΔT) refers to the difference in transparency between its transparent and photo-darkened state. The relative simple calculation of ΔT is shown below [9]:

$$\Delta T = T_0 - T_{dark} \tag{2.7}$$

The transmittance of a material is highly dependent on the wavelength (λ), implying that Equation 2.7 yields a different contrast for each wavelength. To still be able to draw meaningful conclusions from the transmission measurements, the results will be based on an average transmittance (formula 2.8) over a relevant wavelength range.

$$\langle \Delta T \rangle = \langle T_0 \rangle - \langle T_{dark} \rangle \qquad \text{with} \qquad \langle T \rangle = \frac{1}{(\lambda_2 - \lambda_1)} \int_{\lambda_1}^{\lambda_2} T(\lambda)\, d\lambda \tag{2.8}$$

Figure 2.2 presents an example of the photochromic contrast. This figure shows three lines representing the transmission spectrum for the transparent, photo-darkened, and bleached states. A clear difference in transmission is visible between the photo-darkened state and the other two states.

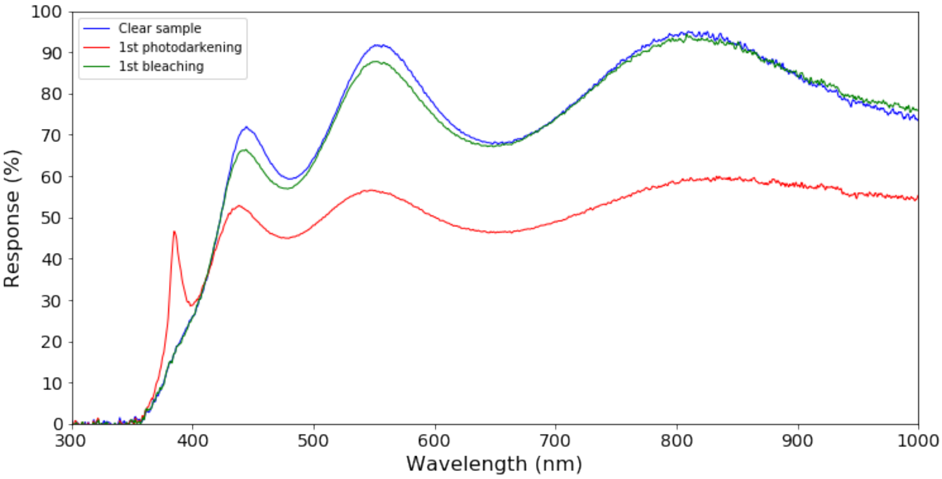

Figure 2.2: Transmission response of a 0.5Pa 400nm sample, showing the spectral behaviour before illumination, during photo-darkening, and after the first bleaching cycle.

The photochromic contrast is not constant for all photochromic thin films. It primarily depends on the material, the layer thickness, and the oxidation grade. For instance, light must pass through more material in a thicker layer, resulting in increased absorption, as can be deducted from equation 2.2. Due to this increased absorption, the thin film will have slightly lower transmission in the transparent state, and the photochromic contrast of the sample will increase. Montero-Amenedo has investigated this, and these findings are shown in figure 2.3 [31].

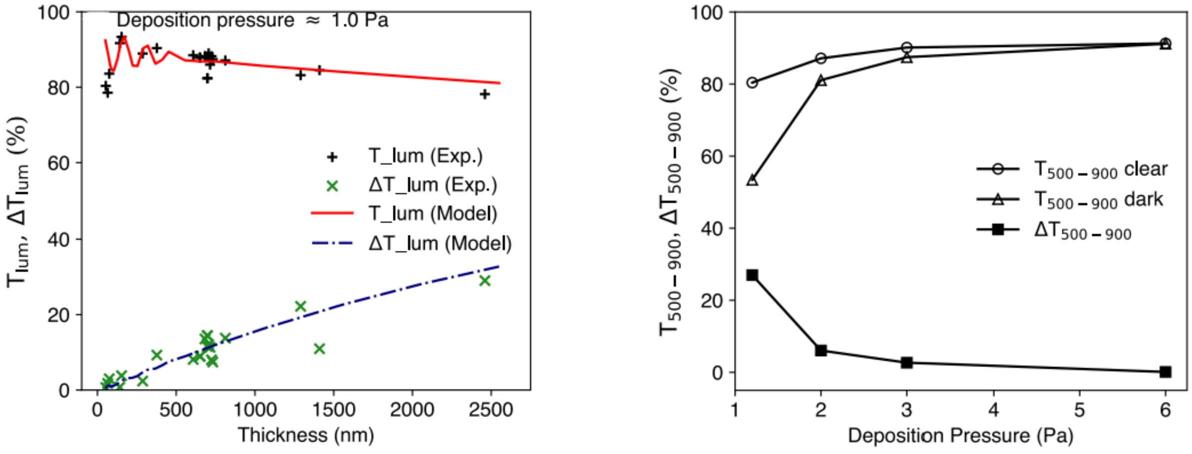

(a)

(b)

Figure 2.3: Transmission and photochromic contrast as a function of thickness and deposition pressure for YOH samples [31]

The deposition pressure also influences the optical properties. Nafezarefi et al. reported a critical pressure (P_c) required for REH2 thin films to oxidise, thus enabling the transition from a metal to a semiconductor when exposed to air [34]. For YOH, this critical pressure is approximately 0.4Pa [9] [31]. To create thin films with photochromic properties, the pressure should be higher than the critical pressure ($p > P_c$). This higher oxidation is due to the sample changing from a densely packed grain to a porous structure. This porosity allows oxygen to be more effectively incorporated into the lattice. As the structure becomes increasingly porous at higher pressures, oxidation also increases. This oxidation results in higher transmission in the transparent state. Consequently, it leads to a lower photochromic contrast, as shown in the right graph in figure 2.3.

2.2.2. Bleaching Time Constant

The second characteristic of the photochromic effect that we will examine is the bleaching time. The bleaching time can be described by the bleaching time constant τ_B, which indicates how long it takes for a material to transform from the photo-darkened state back to the transparent state. The bleaching of a sample can take a relatively long time, and previous research has shown that this time increases after each illumination cycle. After the fourth photo-darkening-bleaching cycle, the YOH sample exhibited a stabilised bleaching time constant [51].

The τ_B can be derived by combining and rewriting several equations [33]. We will start with rewriting the Lambert-Beer law, which we already discussed in section 2.1, equation 2.3, and which relates the transmission and absorption coefficient.

$$\frac{T}{T_0} = e^{-(\alpha-\alpha_0)\cdot d} = e^{-\Delta\alpha\cdot d} \tag{2.9}$$

$$ln(\frac{T}{T_0}) = -\Delta\alpha \cdot d \tag{2.10}$$

In the above formulas, T_0 and α_0 relate to the initial transmission and absorption coefficient, respectively. The change in absorption coefficient ($\Delta\alpha$), in turn, can be related to the cross-section ($\sigma(\lambda)$) and concentration ($c(t)$) of the absorption species.

$$\Delta\alpha(\lambda, t) = \sigma(\lambda) \cdot c(t) \tag{2.11}$$

We use the bleaching time constant (τ_B) to describe the concentration change through time, and assume first-order kinetics are adhered:

$$\frac{dc}{dt} = -\frac{1}{\tau_B}c \tag{2.12}$$

The solution to this differential equation follows exponential decay, starting from the metallic cluster concentration (c_0) at the end of the photo-darkening cycle and approaching zero over time, determined by τ_B.

$$c(t) = c_0 e^{-\frac{1}{\tau_B}t} \tag{2.13}$$

By combining equations 2.10, 2.11, and 2.13, we can construct the following expression:

$$\ln\left(-\ln\left(\frac{T}{T_0}\right)\right) = -\frac{1}{\tau_B}t + \ln(c_0\sigma d) \tag{2.14}$$

Equation 2.14 allows us to determine the bleaching time constant, since we only need the transmission data to retrieve the linear slope, which is determined by the bleaching time constant. Thus by determineing the slope, the bleaching time constant can be obtained.

Previous research by Colombi et al. [9] also shows a direct correlation between the O:H ratio and τ_B. This research demonstrated that τ_B decreases with higher deposition pressure (i.e. higher oxidation grade). This correlation is shown in figure 2.4.

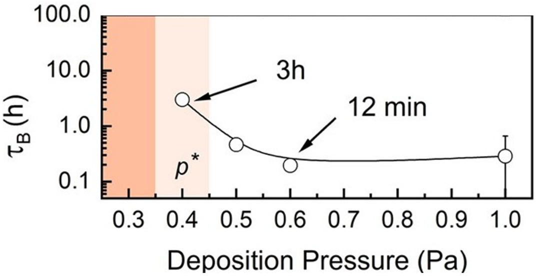

Figure 2.4: The relation between deposition pressure and the bleaching time constant (τ_B) for YOH. [9]

2.2.3. Memory Effect

The memory effect in photochromic materials refers to the phenomenon where previously illuminated areas of the thin film darken faster upon new illumination cycles. This effect is observed by a faster photo-darkening of the previously exposed area. In YOH thin films, this memory effect is also observed as the material's bleaching speed increases upon multiple cycles of light exposure. Even after complete bleaching, the material tends to darken faster when re-exposed to light, indicating a form of structural memory that persists over time. In figure 2.5, we see a paperclip that covers a YOH sample. Upon illumination, the paperclip is visible on the sample. The thin film turns transparent again when the sample is bleached, and the paperclip print disappears. However, if the sample is illuminated for a second time without the paperclip, the memory effect causes the paperclip to become visible again.

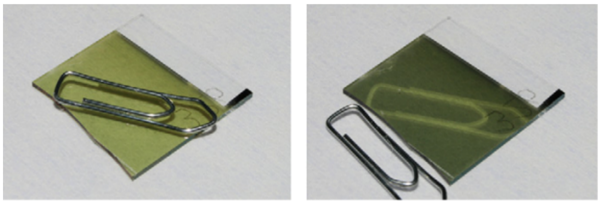

Figure 2.5: A YOH film before and after one hour of illumination, with a paperclip placed on the film to provide a visual contrast. [27]

2.2.4. Darkening Time Constant

Considering the memory effect, it may be useful to describe the darkening time constant (τ_D) in situations where the sample has not fully bleached back to its original transparency. The concentration of metallic clusters in a thin film is denoted by $c(t)$, with c_{sat} representing the saturated concentration. The relationship between the concentration and darkening time is described by the following formula:

$$\frac{c(t)}{c_{sat}} = 1 - e^{-\frac{t}{\tau_D}} \tag{2.15}$$

By combining this equation with equation 2.10 and 2.11, we obtain:

$$-ln(\frac{T}{T_0}) = c_{sat} \cdot \sigma(\lambda) \cdot d(1 - e^{-\frac{t}{\tau_D}}) \tag{2.16}$$

Using the Taylor series expansion for $t \ll \tau_D$ terms, this expression can be simplified to:

$$-ln(\frac{T}{T_0}) \propto \frac{t}{\tau_D} \tag{2.17}$$

Since c_{sat} and $\sigma(\lambda)$ are expected to remain constant for each sample, this method is only suitable for comparing different illumination cycles within the same sample. When comparing different samples, it cannot be assumed that c_{sat}, d, and $\sigma(\lambda)$ are identical, thus limiting τ_D comparison between samples.

2.3. Rare-Earth Oxyhydrides

Rare-Earth (RE) metals, including yttrium, scandium and the lanthanide group, have unique properties that make them important in some high-tech applications [48]. One interesting use for RE metals is in photochromic thin films, whose photochromic effect is largely attributed to RE oxyhydrides (REOH), which are created by the oxidation of RE hydrides.

All RE metal atoms are capable of absorbing up to three hydrogen atoms, leading to the formation of distinct phases. Figure 2.6a presents a phase diagram of the H/M ratio, where M represents RE metal atoms. This diagram shows three distinct equilibrium phases, which are referred to as the α-, β- and γ-phase. These three phases take the form of REH$_x$, but they occupy different regions with values for x that, besides temperature, also depend on the specific RE element. For yttrium, the α-phase is found in the range $0.12 \leq x \leq 0.22$, the β-phase in $2 \leq x \leq 2.1$, and the γ-phase around x=3 [46].

At low hydrogen concentrations, the α-phase is formed. In this phase, the hydrogen atoms occupy the tetrahedral interstitial sites within the metal lattice [46]. By increasing the H/M ratio, we enter into the β-phase (REH$_2$), which has a face-centred cubic (fcc) structure. This phase can coexist with the α-phase, exhibiting metallic-like properties. When the H/M ratio is first increased from the α- to β-phase, the resistivity increases slightly as an effect of impurity scattering [35]. However, the resistivity drops significantly when the ratio gets high enough, indicating that REH$_2$ is a better conductor than pure RE metals.

When the hydrogen content exceeds the capacity of the β-phase, the γ-phase is formed. This phase is typically seen in rare earth trihydrides (REH$_3$) and features a hexagonal close-packed (hcp) structure. In the γ-phase, hydrogen atoms occupy both tetrahedral and octahedral interstitial sites within the lattice [46]. This phase is distinct from the α- and β-phases due to its semi-conducting nature.

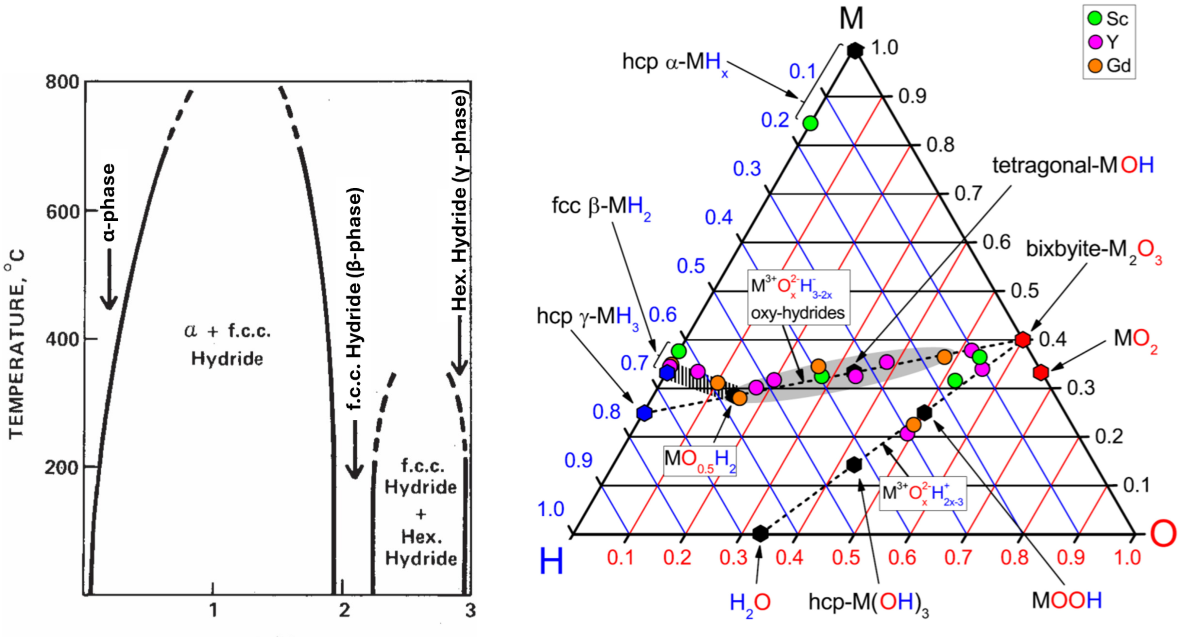

(a) Phase diagram of RE-hydrogen. [20]

(b) Chemical composition diagram of RE-O-H compositions, determined with scandium (Sc), yttrium (Y) and gadolinium (Gd). [11]

Figure 2.6: Phase and chemical composition diagram of RE metals.

The photochromic effect occurs in rare earth (RE) oxyhydrides, which are oxygen-containing RE hydrides. Cornelius et al., in their study ”Oxyhydride Nature of Rare-Earth-Based Photochromic Thin Films” [11], investigated the relationship between chemical composition and photochromism. They developed a composition-phase diagram that can be used to identify the optical properties of different compositions, which is shown in figure 2.6b.

In this diagram, we will focus on two groups, each characterised by their charge neutrality (indicated by the dotted line) while maintaining the following valencies: RE^{3+}, H^{-}, and O^{2-}. The first group is referred to as RE oxyhydrides, with the composition $\mathrm{M^{3+}O_x^{2-}H_{3-2x}^{-}}$ for $0.5 \leq x \leq 1.5$. This group is found on the line between γ-MH$_3$ and M$_2$O$_3$, which is also the region where the photochromic effect in thin films is observed (indicated by the grey area). A transformation is seen between the β-MH$_2$ and MO$_{0.5}$H$_2$ compositions, where samples transform through oxidation from the metallic β-MH$_2$ to the insulating MO$_{0.5}$H$_2$. This transition occurs at deposition pressures above P_c, allowing the sample to oxidise upon exposure to air, converting the metallic cations from M^{2+} to M^{3+}. The transition between metal and insulator was observed through the appearance of an optical bandgap in the sample [11]. RE oxyhydrides with an H/M ratio above 2, which should be located between MO$_{0.5}$H$_2$ and MH$_3$, were not observed.

The second group is called RE hydroxides, with the composition $\mathrm{M^{3+}O_x^{2-}H_{2x-3}^{-}}$ for $1.5 \leq x \leq 3$. This group can be found on the dotted line between M$_2$O$_3$ and M(OH)$_3$, and is created by increasing the oxygen fraction during the deposition process. These films are transparent and do not show any photochromic properties.

2.3.1. Structure

As is shown in figure 2.7, the MH$_2$ has an fcc structure where hydrogen ions occupy all eight tetrahedral sites. The composition transitions to MH$_3$ upon further hydrogenation, where hydrogen ions also fill the four additional octahedral sites.

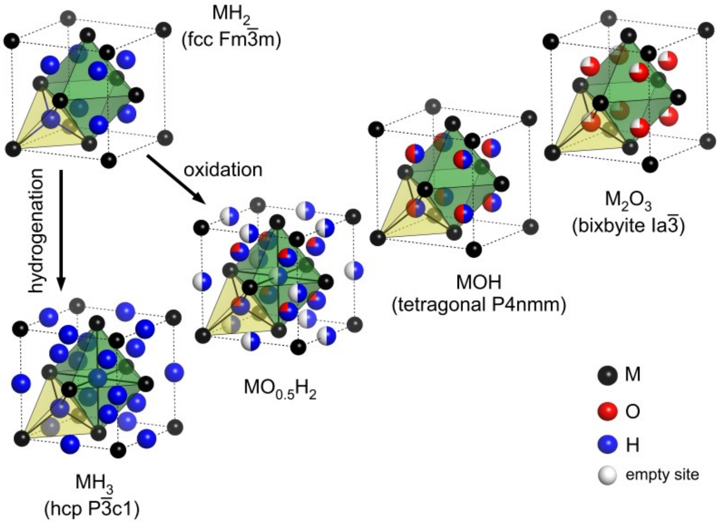

Figure 2.7: Schematic representation of the structure transformations in the M-O-H system. [11]

The MOH structure, visible in figure 2.7, involves a fcc lattice where RE cations occupy the lattice sites, just as in MH$_2$/MH$_3$. The anions, O^{2-} and H^{-}, are distributed within the tetrahedral and octahedral sites. The exact distribution depends on x in $\mathrm{M^{3+}O_x^{2-}H_{3-2x}^{-}}$ $(0.5 \leq x \leq 1.5)$. With an O^{2-} and H^{-} ratio of 1:1 (x=1), there is a transition point where all octahedral sites are empty and tetrahedral sites are fully occupied. For all x above 1, the octahedral sites remain empty, and the vacancies in the tetrahedral sites increase as the oxygen ratio increases. On the other hand, all x below one will have fully occupied tetrahedral sites and mostly filled octahedral sites [11].

2.3.2. Properties and Differences

As previously mentioned, properties such as the photochromic contrast and bleaching time depend on the thin film's RE element and the O:H ratio.

In figure 2.8, we observe three commonly used RE metals in photochromic thin films: scandium (Sc), yttrium (Y) and gadolinium (Gd). Various measurements were conducted on these samples, with variations in deposition pressure. Increasing this pressure results in a higher O/H ratio. We observe that both the Y and Gd samples exhibit a promising photochromic contrast of 28% and 34%, respectively,

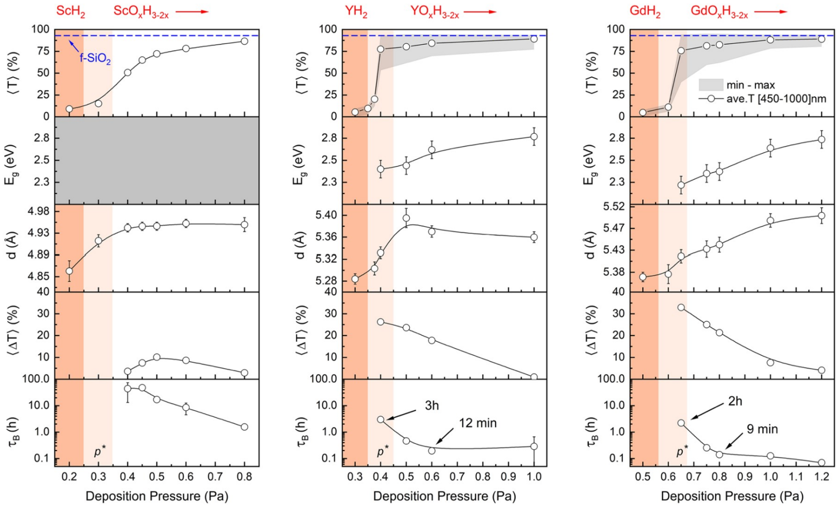

Figure 2.8: Comparison of three RE metals (ScH$_x$, YH$_x$, and GdH$_x$) under varying deposition pressures. The plots show trends in average transmittance ($\langle T \rangle$), optical bandgap energy (E_g), lattice spacing (d), photochromic contrast (ΔT), and bleaching time constant (τ_B). [9]

at depositions just above the critical pressure. Additionally, both samples have bleaching time constants of 3 and 2 hours, respectively, just above the critical pressure. As discussed in section 2.2, the photochromic contrast decreases with higher pressure in both cases, but the bleaching time also decreases. Consequently, we face a trade-off in optimising both important characteristics of photochromic materials.

Research by Cornelius et al. [11] has shown that the bandgap increases with higher oxygen ratios. A larger bandgap implies that more energy is required to excite the electrons from the valence band to the conduction band. It follows that the thin film absorbs less energy since the material does not absorb lower energy levels. This increase in bandgap is also observed in figure 2.8, where the bandgap for both Y and Gd increases at higher pressures, indicating a clear relation between oxygen ratio and bandgap.

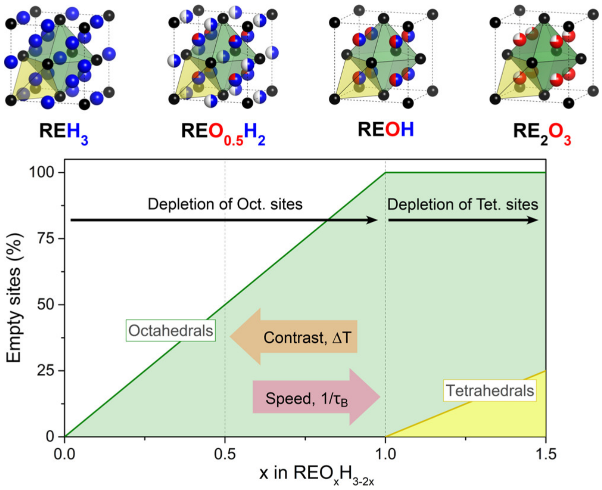

Figure 2.9: Photochromic properties and site depletion as a function of the O/H ratio in REO$_x$H$_{3-2x}$. [9]

In addition to section 2.3.1, figure 2.9 illustrates the structural transformation and properties of rare-earth oxyhydrides (REO$_x$H$_{3-2x}$) as the O/H ratio increases. The schematic representation of some oxyhydrides compositions from figure 2.7 are shown above the graph, highlighting the depletion of octahedral and tetrahedral sites. Figure 2.9 shows the fraction of empty octahedral (green) and tetrahedral (yellow) interstitial sites versus the O/H ratio. As this ratio increases, the octahedral sites deplete first, followed by the tetrahedral sites at x>1, impacting the material's photochromic properties, implying that the photochromic contrast (ΔT) and bleaching speed (1/τ_B) vary with the occupancy of these octahedral and tetrahedral sites. Higher O/H ratios result in increased bleaching speed and decreased contrast, indicating the role of interstitial site occupation in the photochromic behaviour.

2.4. Bandgap

The bandgap of a material is a measure of energy needed to promote an electron. It corresponds to the energy difference between the edge of the valence band (where electrons are usually located) and the edge of the conduction band (where electrons can move around). The bandgap is one of the important principles in semiconductors; it is crucial to a material's electrical and optical characteristics.

Within an atom, electrons are arranged around the nucleus, and they can occupy specific energy levels. However, such energy levels are quantized in that only a few are available, while no energy levels are available in between these levels. The energy levels are located at different distances from the nucleus; the furthest and greatest energy levels are in the valence band. When electrons are energized, they are able to break orbitals from the valence band and occupy the conduction band, resulting in holes, and move on to become charge carriers in the conduction band. Materials are electrified and charged due to these free charge carriers, after which electrical current can pass through materials.

Materials can be classified as conductors, semiconductors, and insulators based on their bandgap and the energies of their conduction and valence bands. The inter-bandgap positions and the associated energy for these three categories are shown in figure 2.10.

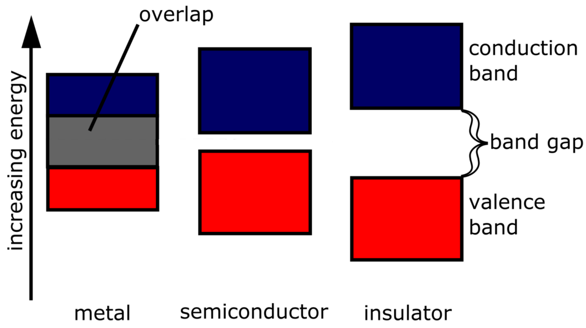

Figure 2.10: Bandgap types in materials: metals (no bandgap), semiconductors (finite bandgap), and insulators (large bandgap). [45]

As is evident from the figure, the valence and conduction band overlap in conductors, and thus there is no bandgap. Since electrons do not need extra energy to jump from the valence into the conduction band, moving between the bands is easy, and thus, the electrical conductivity is very high. Also, in semiconductors, the bandgap is moderate in value, but because it is small, electrons can jump from the valence band to the conduction band with relatively low energy input. A large bandgap is found for insulators. Because of this large bandgap, the flow of electric current is impossible under normal conditions, making insulators ideal for avoiding electrical conduction.

The Fermi level in a semiconductor represents the energy level at which there is a 50% chance of finding an electron at absolute zero temperature. It is used as a reference point for the energy distribution of electrons within the material and can be altered by its composition. In intrinsic semiconductors, the Fermi level lies near the middle of the bandgap, whereas, in n-type or p-type doped semiconductors, it shifts closer to the conduction band or valence band, respectively.

2.4.1. Direct and Indirect Bandgap

Materials with a direct bandgap (figure 2.11a) have the lowest point of the conduction band directly above the highest point of the valence band in the momentum space (same k-vector). This means that the electron can be excited quickly through energy absorption without the need for a change in momentum.

Materials with an indirect bandgap (figure 2.11b) have the lowest point of the conduction band and the highest point of the valence band at different points in the momentum space. Therefore, when electrons transition between these bands, they need to change their momentum in addition to obtaining the bandgap energy. This is typically done by interacting with phonons (vibrations in the lattice). The materials used in this research will also have an indirect bandgap.

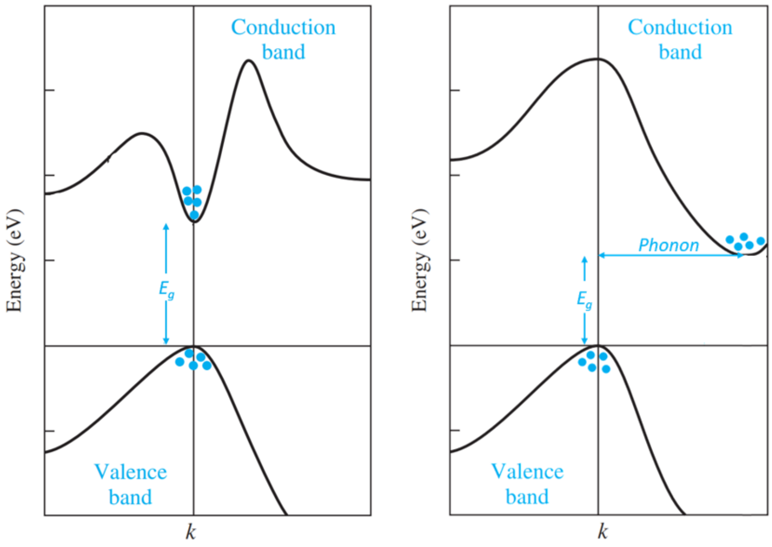

(a) Direct bandgap **(a)** Indirect bandgap

Figure 2.11: Direct and indirect bandgaps. (a) Direct bandgap: conduction and valence band extrema align in k-space, enabling direct transitions. (b) Indirect bandgap: extrema differ in k-space, requiring phonon assistance. [14]

2.4.2. Burstein-Moss Effect

As we previously discussed, the conductivity can also be modified by adding impurities to the semiconductor. This change is due to the alteration in the number of charge carriers in the material.

In the case of heavily doped n-type semiconductors, the fermi level is raised to the point that it sits in the conduction band. In this shift, electrons are moved to the lowest energy states in the conduction band. This means any new electrons excited from the valence band have to move into higher energy states in the conduction band because the excited electrons already occupy the lower ones. Meaning that more energy is required for these excitations, increasing the energy gap between the valence and conduction bands.

$$\Delta E_g = \frac{h^2}{8m^*_{eh}} \left(\frac{3n_{CB}}{\pi} \right)^{2/3} \tag{2.18}$$

$$m^*_{eh} = \frac{(m^*_e \times m^*_h)}{(m^*_e + m^*_h)} \tag{2.19}$$

This bandgap shift is known as the Burstein-Moss shift and may be measured by the Burstein-Moss formula 2.18 [15] where h is Planck's constant, m^*_{eh}, (see formula 2.19) defined as reduced effective mass is the mass of the charge carriers. Moreover, n_{CB} is the electron density in which the conduction band resides.

2.4.3. Tauc Method

The Tauc method is used to determine the optical bandgap of semiconductors. This method uses the relation between the absorption coefficient (α) and the photon energy ($h\nu$) to determine the bandgap of a material [23]. This is done by creating a Tauc plot with formula 2.20 on the y-axis and $h\nu$ on the x-axis, and identifying the linear portion of this plot and extrapolating it to intersect the x-axis, which will give you the bandgap energy of the material. An example of a Tauc plot can be seen in figure 2.12.

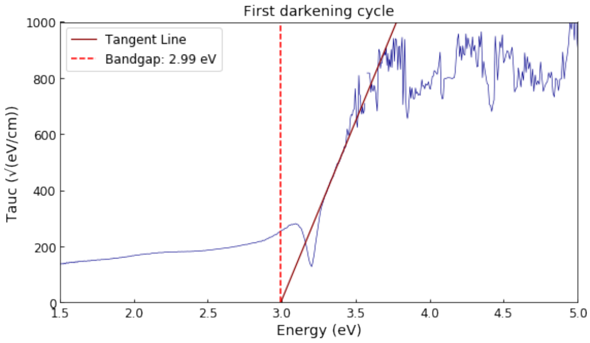

Figure 2.12: Tauc plot for a 0.5Pa 400 nm sample after the first illumination cycle, showing the bandgap energy of 2.99eV determined using the tangent line method.

$$(\alpha h\nu)^{\frac{1}{\gamma}} = B(h\nu - E_g) \tag{2.20}$$

The absorption coefficient in the above formula can be determined by extracting the transmission and reflection during optical measurements (section 4.2) and rewriting the formula 2.4. Alternatively, we can use formula 2.21, which requires the wavelength (λ) and the imaginary part of the complex refractive index (k), that both can be determined in spectroscopic ellipsometry measurements (section 4.3).

$$\alpha = \frac{4\pi k}{\lambda} \tag{2.21}$$

Furthermore, formula 2.20 requires the input of constants B and γ, of which the latter one is linked to the bandgap of the material. Direct and indirect bandgaps require a value of $\frac{1}{2}$ and 2 for γ, respectively.

2.5. Proposed Mechanism

Since the first paper reporting the photochromic effect in yttrium oxyhydride by Mongstad et al. [27], an exact mechanism for this effect has not been found. Many experimental methods have been used to analyze the film while it is being illuminated with the expectation that a mechanism might be found. Although Mongstad recognized the relationship between oxidation state and photochromism, no mechanism was ever reported. Meanwhile, Chuan You et al. [52] investigated the photoconductivity under light and pointed out that the photochromism is caused by the metallic clusters formed. Two mechanisms have been discussed: one suggests the creation of H-rich domains in the YOH layer and the second is based on an insulator-to-metal transition. Both proposed mechanisms are depicted in figure 2.13.

2.5.1. H-rich Metallic Domains

The first mechanism shows that metallic domains in the thin film are created by the process of neutral hydrogen diffusion within the sample. Upon illumination, electron-hole pairs are generated. The holes tend to recombine with H^- ions, which are subsequently released from their octahedral sites [10], resulting in the formation of neutral hydrogen (H^0). This H is highly mobile within the layer and moves to regions with low oxygen concentration, where it forms metallic clusters [50]. These regions with low oxygen concentration will typically form metallic clusters when there is a O:H ratio for YH_2O_x below $x < 0.5$ [49]. Thus, the resultant layer has hydrogen-rich areas comprising metallic clusters and hydrogen-poor areas of a higher concentration of oxygen [2].

2.5.2. Anderson-Mott Insulator-to-Metal Transition

The second mechanism involves an insulator-to-metal transition in the thin film. Upon illumination, neutral hydrogen atoms are formed that are very mobile within the layer, as discussed in section 2.5.1. These hydrogen ions leave positively charged vacancies (V_{H^+}) on the octahedral sites, acting as a potential well for electrons [36], which in turn capture the higher energy state (e_g) electrons from the

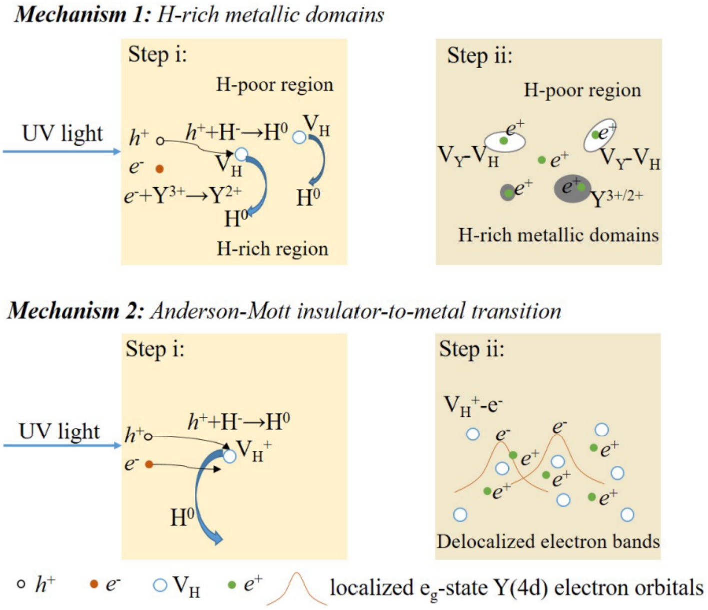

Figure 2.13: Two mechanisms explaining photochromic behaviour: (1) formation of H-rich metallic domains and (2) Anderson-Mott insulator-to-metal transition. Both mechanisms detail UV light-induced processes involving hydrogen and electron interactions. [49]

nearby yttrium (Y-4d-e_g) orbitals [12]. This process continues during illumination, and when enough electrons have been captured in the potential wells, their orbitals start to overlap, and metallic behaviour sets in.

2.6. Electrodynamics

2.6.1. Electromagnetic Radiation

The electromagnetic spectrum ranges from long-wavelength radio waves to short-wavelength gamma rays. Electromagnetic (EM) radiation, as the name states, consists of electric and magnetic energy waves and is a form of energy that travels at the speed of light, exhibiting wave-like and particle-like properties. The foundation for EM radiation was laid by Maxwell, who proved the connection between both electric and magnetic waves through the Maxwell Equations [53].

Some wave-like properties that play an important role in characterising EM radiation are the wavelength (λ) and frequency (f), linked through the following formula:

$$c = \lambda f \tag{2.22}$$

$$E = hf \tag{2.23}$$

In addition, EM radiation is composed of photons, meaning we can use Planck's equation (eq 2.23) to describe the energy these photons carry. Combing both formulas gives us a relation between the energy and wavelength:

$$E = \frac{hc}{\lambda} \tag{2.24}$$

2.6.2. Interference

When two waves travel through the same medium simultaneously, they will interact with each other, which is called interference. This interaction between two waves can be constructive or destructive depending on the phases of both waves.

Constructive interference occurs when two waves, which are in the same phase collide with on another. Meaning that the crests and troughs of both waves amplify each other. This alignment causes the amplitudes of the individual waves to add together, resulting in a wave with a higher amplitude.

Destructive interference, on the other hand, is the exact opposite of constructive interference. This process occurs if a crest and a trough coincide and cancel each other, resulting in a lower amplitude.

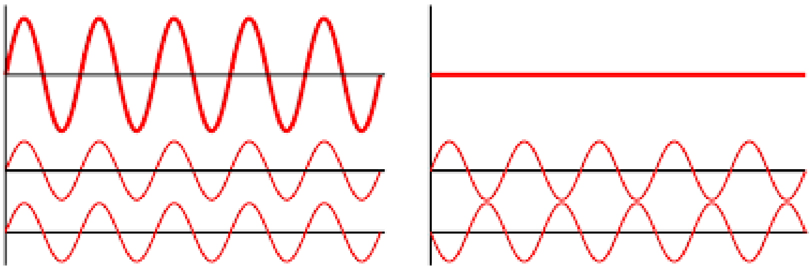

Figure 2.14: Constructive (left) and destructive (right) interference, illustrating the superposition of waves leading to amplified or cancelled amplitudes. [32]

The interaction that waves have with each other largely depends on their phase relative to each other. For waves of the same wavelength, a half wavelength (π) phase difference results in destructive interference, and a full wavelength (2π) phase difference results in constructive interference. Everything in between is a combination of both and can be calculated simply by adding the amplitudes together [19].

2.6.3. Photon Flux

As discussed in section 2.6.1, EM radiation consists of photons carrying energy. We will quantify the power EM radiation produces by looking at joules per second per meter squared (J/m^2s or W/m^2), called the irradiance (I). The photon flux can be obtained from irradiance by dividing through the energy of a single photon, which is expressed by the formula 2.23.

Spectral irradiance should be used to measure sources that emit over a spectrum of wavelengths. Spectral irradiance shows the irradiance per wavelength ($W/m^2/nm$), so total irradiance is then found by integrating the spectral irradiance over the range of wavelengths that are emitted:

$$I = \int_{\lambda_1}^{\lambda_2} I(\lambda) d\lambda \tag{2.25}$$

So the photon flux will be determined by dividing formula 2.25 through the photon's energy:

$$\Phi = \int_{\lambda_1}^{\lambda_2} \frac{\lambda I(\lambda)}{hc} d\lambda \tag{2.26}$$

2.6.4. Brewster Angle

When light is incident on a material, it can be refracted, meaning it goes through the material, and it can be reflected. The Brewster angle is a specific angle at which unpolarised light that is incident on a material becomes polarised in its reflected ray and partially polarised in its refracted ray. So, when unpolarised light hits a surface at the Brewster angle, the reflected light will be completely s-polarised (perpendicular to the plane of incidence). The refracted and reflected light will always be perpendicular to each other at this angle.

$$\theta_B = arctan(\frac{n_2}{n_1}) \tag{2.27}$$

The Brewster angle can be calculated through the formula 2.27, where n_1 and n_2 are the refractive indices of the medium and material, respectively.

Considering light travelling from air ($n_1 = 1$ [1]) into YOH ($n_2 \approx 2.18$ [55], depending on the O/H ratio). Filling in formula 2.27 gives us a θ_B of approximately 65°.

2.7. Atomic Interaction

2.7.1. Electron–Positron Annihilation

Annihilation occurs when an electron and its counterpart, a positron, collide and annihilate, which will create two gamma particles.

$$e^+ + e^- \longrightarrow \gamma_1 + \gamma_2 \tag{2.28}$$

A positron initially diffuses when it is injected into a material. The atomic and electronic structure of the material influences the positron's path during diffusion. The path of the positron is not straightforward. It is affected by collisions with atoms, defects, and variations in the electron density, losing most of its kinetic energy through these interactions. This drunkard's walk in the material continues until the positron encounters an electron.

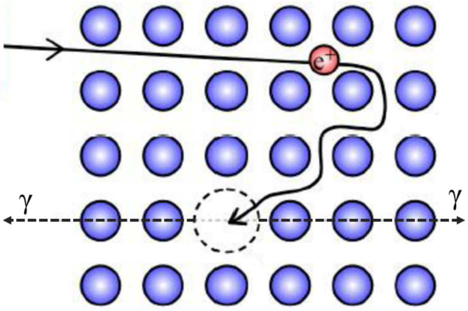

Figure 2.15: The lifetime of a positron in a material, showing its trajectory and eventual annihilation, emitting gamma radiation. [39]

Due to their opposite charges, an electron and a positron will be attracted to one another. As the two particles approach one another, the chance of annihilation increases. Once the particles come close enough, they will annihilate, which is a process resulting in the production of gamma rays (see equation 2.28). These two gamma rays are emitted from where the annihilation took place, each with an energy of approximately 511keV, travelling in opposite directions since momentum must be conserved.

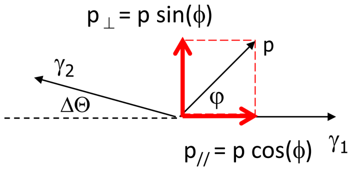

Figure 2.16: Schematic of electron–positron annihilation, illustrating the emission of two gamma photons and the relationship to electron momentum (p). [41]

Figure 2.16 displays the collision's kinetics. The momentum of the positron can be ignored because it has nearly stopped immediately before annihilation. The formula 2.29 can be used to express the total energy for the collision. The electron's momentum is responsible for the $\sqrt{p^2c^2}$ term in this equation. The entire energy will be preserved and converted into E_{γ_1} and E_{γ_2} gamma rays.

$$\sqrt{m_0^2c^4 + p^2c^2} + m_0c^2 \tag{2.29}$$

Furthermore, momentum is preserved during the impact. The momentum on the right side of the equal sign in equation 2.30 indicates the momentum following annihilation, whereas the momentum on the left indicates the momentum prior to the collision.

$$cp_{//} = E_{y1} - E_{y2}\cos(\phi) \qquad cp_{\perp} = E_{y2}\sin(\phi) \tag{2.30}$$

By combining these equations, we can get the deviation angle ($\Delta\Theta_{\gamma_1-\gamma_2}$) and the energies of both gamma rays ($E_{\gamma_1} + E_{\gamma_2}$), as shown in figure 2.16.

$$E_{\gamma_1} = \frac{m_0c^2 + \sqrt{m_0^2c^4 + p^2c^2} + pc\cos(\phi)}{2} \qquad E_{\gamma_2} = \frac{m_0c^2 + \sqrt{m_0^2c^4 + p^2c^2} - pc\cos(\phi)}{2} \tag{2.31}$$

$$\Delta\Theta_{\gamma_1-\gamma_2} = \frac{2pc\sin(\phi)}{pc\cos(\phi) + m_0c^2 + \sqrt{m_0^2c^4 + p^2c^2}} \tag{2.32}$$

Although these are still estimates, they should be considered fairly accurate. To simplify the calculations, we say that $\Delta\Theta_{\gamma_1-\gamma_2}$ is relatively tiny and that $pc \ll m_0c^2$. The following equations result from applying these simplifications to the formulas:

$$E_{\gamma} = m_oc^2 \pm \frac{1}{2}p_{//}c \qquad \Delta\Theta_{\gamma_1-\gamma_2} = \frac{p_{\perp}}{m_oc} \tag{2.33}$$

According to the gamma energy equation, if the electron had no momentum, its energy would be exactly 511keV. Not all electrons, however, exhibit this behaviour, leading to a normal distribution around 511keV.

2.7.2. Bragg's Law

Bragg's law gives us a method to analyse atomic structures by using X-rays to reveal the arrangement of atoms in a crystal structure: the law describes the conditions necessary for constructive interference of X-rays that have been scattered by the layers of atoms in a crystal and how these scattered waves combine to either reinforce or cancel each other out: when X-rays hit a crystal lattice at a particular angle (θ) they interact with the atoms in the crystal in a way that's shown in Figure 2.17.

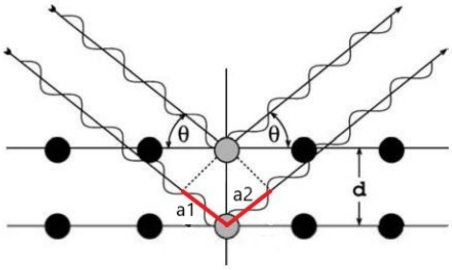

Figure 2.17: Incident X-rays interacting with crystal lattice planes, illustrating Bragg's law with incident angle (θ) and interplanar spacing (d). [43]

The figure shows two lattice planes positioned one above the other, separated by a distance d. Each of these planes scatters a different X-ray wave that is hitting the crystal at the same angle θ: by using some basic geometry we can observe that the wave striking the lower plane travels a distance of $a1+a2$ farther than the wave scattered from the top plane: both of these distances $a1$ and $a2$ can be described as:

$$a1 = a2 = dsin(\theta) \tag{2.34}$$

The nature of the interference (whether constructive or destructive) between these two scattered waves depends on the extra distance travelled by the lower wave. If this distance ($2d\sin(\theta)$) is exactly an integer multiple (n) of the X-ray wavelength (λ), then constructive interference will occur, which means that both waves will amplify each other's intensity as explained in section 2.6.2. This relationship is precisely what Bragg's law expresses [43]:

$$2dsin(\theta) = n\lambda \tag{2.35}$$

3

Sample Deposition

Our samples will be created using the DC magnetron sputtering setup available at the Materials for Energy Conversion and Storage (MECS) group within the Chemical Engineering department at the TU Delft. The YH_2 layer will be deposited on a fused silica (f-SiO_2) substrate, which is available in small 10mm by 10mm formats.

3.1. Sample Parameters

We began with the first batch of samples, depositing a single 400nm layer at a pressure of 0.5Pa. The second batch consists of depositions at 0.8Pa and varying the samples' thicknesses between 400, 600, and 800nm. Finally, a third batch was produced, consisting of double-layer samples. We created two double-layer samples with a total thickness of 600nm. Two layers of 300nm will be deposited on each other, with varying configurations of 0.5Pa and 0.8Pa layers.

Before any measurements were conducted on these samples, we ensured they had oxidised for at least 10 days.

Batch	#	Layer type	Pressure (Pa)	Power (W)	Thickness (nm)	Layer 1 (nm)	Layer 2 (nm)
1	1	Single	0.5	75	400	400	n.a.
2	2	Single	0.8	75	400	400	n.a.
	3	Single	0.8	75	600	600	n.a.
	4	Single	0.8	75	800	800	n.a.
3	5	Double	0.5 / 0.8	75	600	300	300
	6	Double	0.8 / 0.5	75	600	300	300

Table 3.1: Deposition parameters for all samples used in the study, including batch number, layer type, deposition pressure, power, total thickness, and individual layer thicknesses.

It should be noted that the aimed thickness is not guaranteed due to the wide variety of parameters that influence it. The final thickness will be determined using profilometry.

3.2. Reactive DC Magnetron Sputtering

Reactive DC magnetron sputtering is a technique where thin films can be deposited onto substrates. The process occurs under vacuum conditions to obtain an environment as controlled as possible. An overview of our setup is schematically shown in figure 3.1. The material to be deposited is called the ”target” and is placed at the cathode, in our case, yttrium (Y). The thin film forms at the anode on the other side where the f-SiO_2 substrate is placed.

Within the chamber, two gases are present. The first is argon, used as a sputtering gas to create plasma and bombard the target. The second is hydrogen, which serves as a reactive gas for the creation of a

YH_2 layer. The hydrogen flow can be regulated with a valve; if this valve is closed, a pure yttrium thin film will be created.

To start the sputtering process, a DC power source will apply a high voltage between the cathode and anode to develop an electric field. This voltage ionises the argon into a plasma of positive ions (Ar^+) [18].

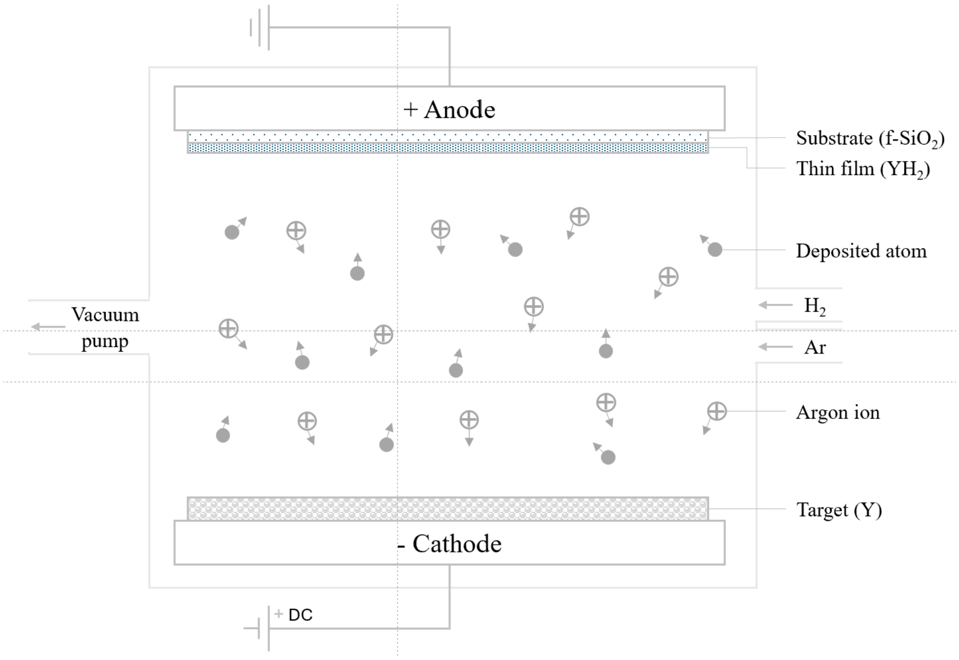

Figure 3.1: Schematic overview of the reactive DC sputtering setup used for thin film deposition.

Initially, the substrate is covered with a shield to allow the plasma to stabilize without forming an inhomogeneous layer. To improve uniformity among the samples within the same batch, the substrate is rotated at 60 rpm. After two minutes, the shield is removed, and the deposition process begins on the substrate.

During sputtering, the electric field accelerates the positive argon ions towards the yttrium target. The impact of the argon ions causes the yttrium to be ejected from the target, travelling towards the substrate placed at the anode, forming the required thin film by gradual build-up. The thickness of our samples depends on sputtering time and power, which is usually linearly dependent on these parameters. Both can be varied depending on the needs. Lower power implies a slower deposition rate; the same thickness requires longer sputtering. Some tape will be added to one of the samples to perform profilometry measurements, leaving a region without the YH_2 layer.

3.3. Deposited Samples

As mentioned in the above section, the sample thickness depends on various parameters and should be measured using profilometry. The measured layer thicknesses of our samples are presented in table 3.2. These values represent the average of three measurements per sample, rounded with 5nm accuracy.

A deviation in the deposition speed for the 0.8Pa samples resulted in a lower thickness than expected. The thinner samples' will have minimal effect on the results, and comparisons can still be made. In this report, the targeted thickness will be used when referring to samples.

In the table, the double-layer samples are also presented as separate single-layers. During the deposition of each layer in the double-layer samples, two transparent f-SiO_2 substrates were placed in the deposition chamber. This approach allows the measurement of each individual single-layer that constitutes the double-layer sample, which will help us examine the double-layer samples since we can obtain the properties of both single-layers.

Batch	#		Layer type	Thickness (nm)
1	1		Single	370
2	2		Single	305
	3		Single	475
	4		Single	750
3	5		Double	555
		a	Single(0.8Pa)	295
		b	Single(0.5Pa)	260
	6		Double	545
		a	Single(0.5Pa)	240
		b	Single(0.8Pa)	305

Table 3.2: Sample thicknesses obtained using profilometry.

The deposited samples, with their different parameters, have their own observable characteristics in the transparent phase. In figure 3.2, we can see the samples from batches 1, 2 and 3 from left to right.

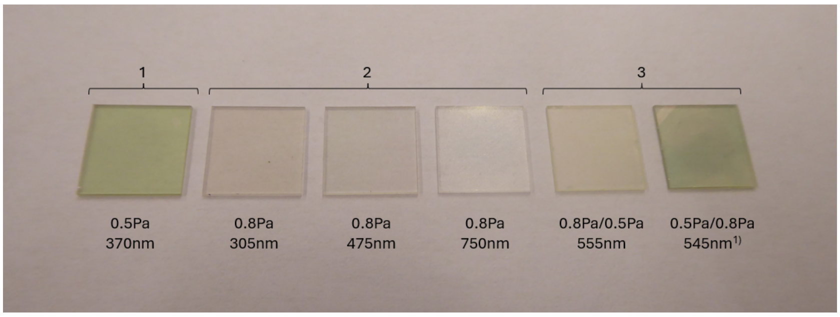

Figure 3.2: Photograph of all samples in their transparent phase.
1) Sample has been illuminated, and is at the end of its bleaching process, hence the slightly darker circle in the middle.

The 0.5Pa sample is yellowish, whereas the 0.8Pa samples look almost colourless. The 0.8Pa 800nm is observably different from the thinner 0.8Pa samples, which might indicate an inhomogeneous thin film (not visible in this image), as we will discuss in the results. Both double-layer samples have their own colour, and the substrate/0.8Pa/0.5Pa looks very opaque when looking through the sample (also not visible in image).

4

Experimental Methods

4.1. UV illumination

In this research, we investigate the properties of photochromic materials by conducting measurements before, during, and after illumination. Not all measuring setups are equipped with an LED lamp for investigations of this type. If the setup calls for it, we use an LED lamp that will suit both in- and ex-situ measurements. In this study, we use the M385LP1 by Thorlabs for all our illuminations, with an intensity of 30mW/cm², placed at 15cm.

4.2. Optical Measurements

Optical measurements were performed on the PHOCS 2 setup, located at the MECS group in the Chemical Engineering department. This setup consists of a light source used for sample illumination and two detectors, one for transmission and the other for reflection (see formula 2.2). By retrieving data from these detectors, we can accurately model other parameters characteristic of photochromic thin films, such as the absorption and bleaching time constant.

We illuminated the samples at an intensity of 30mW/cm² during our experiment. Using formula 2.26, this corresponds to a photon flux of 5.8$\cdot 10^{16}$photons/cm². Additionally, for both transmission and reflection, we used the relevant equation from formula 2.8, focusing on a specific wavelength range. The wavelength range considered in this work lies between 450 - 1000nm.

4.2.1. Setup

The transmission and reflection measurements were performed using an Ocean Optics DH-2000BAL light source and Ocean Optics HR4000 and USB2000+ detectors for the transmission and reflection data, respectively. Both detectors have a wavelength range between 200 - 1100nm and make measurements as a function of wavelength, as can be seen in figure 2.2. Additionally, the illumination of the sample was carried out using a Thorlabs M385LP1 LED light, which has a wavelength of 385nm. To achieve the desired intensity of 30mW/cm², the current of the light source was set to 170mA.

4.2.2. Data analysis

These measurements can provide a large amount of data, as explained in section 2.1. We will analyse this data using four different Python scripts that each display different parameters. The first two scripts will plot the transmission and reflection data points as a function of time and wavelength, respectively.

We will also create a Python script to calculate the bleaching time constant from equation 2.13. In this script, the left side of this equation will be plotted against time on the vertical axis (y-axis), and the slope coefficient will allow us to extract the bleaching time constant.

Finally, we will obtain the bandgap for different moments in time. If we rearrange the Beer-Lambert Law (equation 2.3), we can also get the absorption coefficient as a function of the wavelength. The wavelength can then be transformed into the energy of a photon (equation 2.24), leading to the appearance

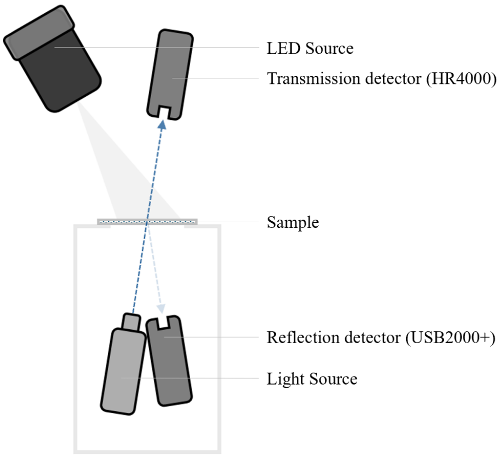

Figure 4.1: Schematic representation of the optical measurement setup.

of a Tauc plot. This plot, as described in section 2.4.3, allows us to extract the bandgap.

4.3. Spectroscopic Ellipsometry

Spectroscopic Ellipsometry (SE) measurements can be used to define a material's optical characteristics. During the measurements, a light beam is passed through a polariser, which only allows s- and p-polarised light to pass through. These two polarised beams are perpendicular to each other, have equal amplitude, and have no phase difference.

As the s- and p-polarized beams reach the sample, they are reflected at the surface, leading to the change in amplitude and phase. This change is illustrated by the complex reflectance ratio (ρ), which denotes the ratio between the variables r_p and r_s. The r_p and r_s correspond to the normalised amplitude of the reflected waves relative to the initial amplitude concerning the p- and s-polarised light, respectively. Reflectance ratio can also be expressed with formula 4.1, where Δ is the phase difference and tan(Ψ) describes the amplitude ratio of the wave after it has been reflected.

$$\rho = \frac{r_p}{r_s} = tan(\Psi)e^{i\Delta} \tag{4.1}$$

The detector measures the values of Δ and Ψ, after which the data are processed through simulation and modelling (section 4.3.2). This analysis allows for determining the complex refractive index, composed of the refractive index (n) and the extinction coefficient (k), representing the real and imaginary parts, respectively. The extinction coefficient can then be used to calculate the absorption coefficient (see formula 2.21).

4.3.1. Setup

Our research used the J.A. Woollam M-2000 Ellipsometer in the ESP lab at TU Delft. This SE setup is capable of measuring wavelengths ranging from 191nm to 1688nm. In order to enhance the precision of the measurement, the areas were measured at three different angles. The angles of the measurements, as a rule, should be close to the Brewster angle. The Brewster angle, as calculated in section 2.6.4, is approximately equal to 65 degrees. It was decided to take three measurements ranging from 60 to 70 degrees in 5-degree steps.

4.3.2. Data analysis

The data obtained from our measurements will need to be analysed using the accompanying CompleteEASE software. This software allows us to fit the measured data in various ways, with the goal of describing it as accurately as possible while ensuring a physically correct model and the best possible fit with the measured data, which is indicated by the Mean Squared Error (MSE). In previous research,

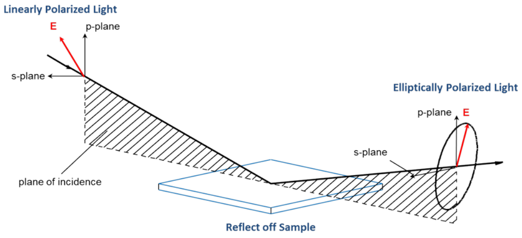

Figure 4.2: Schematic representation of the SE setup. [6]

the YOH thin films were modelled using the Cauchy or general oscillator (GenOsc) model, which we will use in our research.

Cauchy model

When examining the optical constants of transparent layers, the Cauchy model is commonly used to describe the material's optical characteristics. This model operates under the assumption that the extinction coefficient (k), which corresponds to absorption, is approximately zero. The refractive index (n) is then determined using the formula below, with the parameters A and B being fitted accordingly [6].

$$n(\lambda) = A + \frac{B}{\lambda^2} \tag{4.2}$$

To model the material near the absorption edge, where the assumption $k = 0$ is no longer valid, we add an Urbach tail in combination with the Cauchy model. The Urbach tail accounts for the absorptive behaviour of the film and allows for modelling the extinction coefficient with the following formula:

$$k = k_{amp} \cdot e^{\text{exp}(E - \text{Bandedge})} \tag{4.3}$$

General oscillator model

Besides the Cauchy method, it is also possible to model the data using General Oscillators (Gen-Osc). This method makes it possible to use one or multiple oscillators to fit the measured data optimally. Commonly used oscillators in this approach include the Lorentz, Tauc-Lorentz, Gaussian, and Drude oscillators. The general equation for the dielectric function ($\epsilon = \epsilon_1 + i\epsilon_2$) is expressed as a sum of these oscillators, each affecting n and k across specific energy or wavelength ranges.

Research conducted by Zubkins et al. [55] also explored YOH samples. They successfully modelled the photo-darkened state using a Drude oscillator (DO) combined with 3–4 Lorentz or Gaussian oscillators (GO). Conversely, the bleached state was represented using a combination of one Tauc-Lorentz oscillator (TLO) and one GO.

Effective medium approximation model

The Effective Medium Approximation (EMA) model is applicable when the sample exhibits inhomogeneities in its material composition. The influence of voids or other material inclusions alters the resulting optical constants. By employing the EMA model, up to two additional compounds can be integrated into the previously discussed Cauchy model. This approach allows for estimating the fraction of metallic clusters and voids within the sample, and fits the influence of each additional compound on the resulting optical constants.

4.4. X-Ray Diffraction

We used an X-Ray Diffraction (XRD) setup to examine the molecular crystal properties of our samples. The XRD measurement uses an X-ray directed at the sample at a specific angle and, when reflected, detected at the same angle on the opposite side. Due to interference resulting from Bragg's Law (section 2.7.2), we can gain insights into the crystal structure of the sample.

The incident X-ray undergoes a specific phase shift at certain angles, which, as shown in figure 2.17, can be attributed to the lattice spacing. By rotating the X-ray over an angular range between 0 and 90 degrees, a pattern is obtained that peaks at specific angles, indicating that constructive interference has occurred at these angles. This information provides insights into the lattice spacing and parameters. The relationship between the angle and the lattice spacing is described by Bragg's law (equation 2.35).

4.4.1. Setup

In the setup we use, both XRD arms have the same angle (θ), and is therefore called a 2θ XRD measurement. We used the PANalytical X-pert Pro diffractometer located at the Reactor Insitute Delft. The source in this diffractometer is made of copper and produces an X-ray with a wavelength of 1.541Å. Figure 4.3 shows a schematic overview of the setup we used in this research.

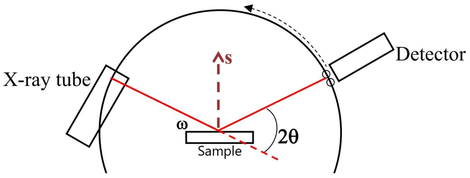

Figure 4.3: Schematic representation of the XRD setup. [42]

Since not all angles are important, we decided to make a scan between 20 and 70 degrees. The current and voltage were set to $40mA$ and $45kV$, respectively.

4.4.2. Data analysis

The data collected from the measurements were analysed using FullProf software. The 'WinPlotr' tool was used to plot the data, after which the background noise was selected manually. This background data file will be imported into the 'EdPCR' tool, where a Rietveld refinement was carried out. This refinement is performed by modelling the measured data using the least squares approach [40], thus minimising the MSE of the model to the measurement.

The refinement process gives the lengths of the cell edges (a, b, c), which are identical due to the cubic nature of the cell. Additionally, FullProf's database allows for matching the peaks in our original diffraction pattern to specific crystal orientations. Further literature will be studied to attribute any remaining peaks to known crystal orientations.

4.5. Doppler Broadening Positron Annihilation Spectroscopy

Doppler Broadening Positron Annihilation Spectroscopy (DB-PAS) is a nondestructive analytical technique used to detect open-volume defects, such as vacancies and voids, in thin films. This method involves the interaction between positrons and electrons in the material, leading to annihilation and the emission of gamma rays. The energy distribution of these gamma rays provides detailed insights into the nature of the defects present in the material.

$$^{22}_{11}\mathrm{Na} \longrightarrow {}^{22}_{10}\mathrm{Ne} + \mathrm{e}^{+} \tag{4.4}$$

Positrons are generated through the decay of ^{22}Na (equation 4.4). These positrons are emitted at various energies in different directions. To control the implementation depth of the positrons, the energy has to be moderated. This is done by first passing the positrons through a tungsten (W) moderator, reducing their kinetic energy. All low-energy positrons emitted through the moderator will now pass through an electric field, guiding the positrons to the sample using the Lorentz force. A slight bend in the pipe is introduced to eliminate any remaining high-energy positrons that did not lose enough energy. These high-energy positrons will travel in a straight line and not bend towards the sample. In addition to guiding the positrons to the sample, the electric field can also accelerate positrons, increasing their kinetic energy and thus their implementation depth (also see figure 2.15).

The entire setup operates under Ultra-High Vacuum (UHV) conditions. This vacuum environment is essential to minimising collisions between positrons and residual gas atoms, which could otherwise lead to unwanted collisions and annihilations before reaching the sample.

As discussed in section 2.7.1, the diffused positrons will annihilate with electrons in the sample. This annihilation creates two gamma rays with a combined energy of 1022keV. During normal annihilation conditions, both gamma rays' energy equals 511keV. However, as we can conclude from formula 2.31, small shifts in this energy can be caused by the initial electrons' momentum. Electrons in high-vacancy regions have lower momentum and thus have energies close to 511keV. On the other hand, electrons in a densely packed lattice structure have a higher momentum, indicating the production of gamma rays with a higher deviation from the previously mentioned 511keV.

4.5.1. Setup

The DB-PAS measurements in this research were performed with the setup located at the RID. As previously mentioned, this setup uses a ^{22}Na source and is able to perform Variable Energy Positron(VEP) measurements. For our VEP measurements we will measure between 0.1 and 22keV increasing the energy as following:

$$E(n) = 0.1 + \sum_{j=0}^{N-2} 0.14 * 1.10^{j} \tag{4.5}$$

In figure 4.4, we depicted a simplified image of our DB-PAS setup. The vacuum in the chamber will be pumped until a UHV of at least 10^{-6}mbar.

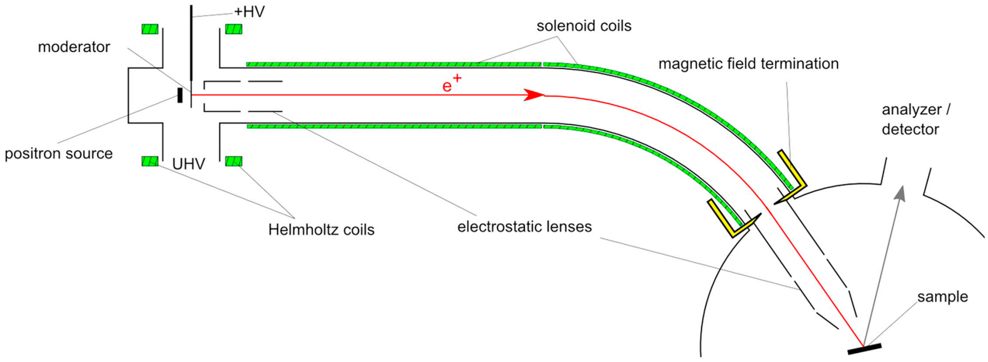

Figure 4.4: Schematic representation of the DB-PAS setup. [17]

4.5.2. Data analysis

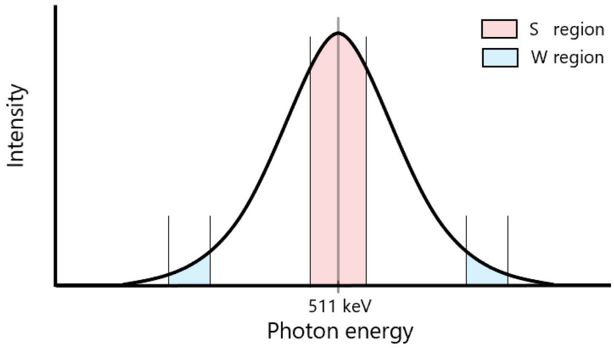

Figure 4.5: Energy distribution of gamma particles, highlighting the S and W regions in colour.

After performing a large number of measurements (40,000), an energy spectrum of gamma rays can be constructed for each implementation energy. This energy spectrum has the form of a normal distribution around 511keV, and looks similar to figure 4.5. The S- and W-parameters can be extracted from the energy spectrum, each representing a fraction of the total energy spectrum within a defined region. The momentum windows are $|p| < 3.0 * 10^{-3} m_0 c$ and $8.2 * 10^{-3} m0c < |p| < 23.4 * 10^{-3} m_0 c$ for the S- and W-parameter, respectively. Both parameters are determined with the fractions given in formula 4.6.

$$S = \frac{S_{region}}{A_{total}} \qquad W = \frac{W_{region}}{A_{total}} \tag{4.6}$$

The energy spectrum analysis for each implementation energy is done using the VEPFIT software [47]. This software creates an implementation profile for the measured samples and optimises the fitting of the data by minimising the MSE. To ensure this analysis runs smoothly, we only need the density and diffusion length of the materials in our sample, which are provided in the table below:

Material	Density (g/cm^3)	Diffusion Length (nm)
YOH	4.15 [38]	47 [38]
f-Si (fused silica)	2.2 [13]	25

Table 4.1: Material properties used in VEPFIT software.

5

Results

5.1. Optical Measurements

Two different types of illumination cycles were selected for our optical measurements. The first type consists of 150 minutes of illumination, followed by bleaching for 1200 minutes (20 hours). This process will be repeated three consecutive times. The second type of measurement will study the film's capability to undergo more rapid changes in transparency. The sample will undergo 18 cycles, each consisting of 120 minutes of photo-darkening followed by 120 minutes of bleaching.

We will consider the samples' transparency and photochromic contrast in these results. It is important to note that the photochromic contrast presented here is not a direct application of equation 2.7 but is normalised to the initial transparent state transmission to compare with other studies. The normalisation in this regard is done using the formula below:

$$\frac{\Delta T}{T_0} = \frac{T_0 - T_{dark}}{T_0} \tag{5.1}$$

5.1.1. Single-layer Optical Measurements

Figure 5.1 shows the transmission spectra of both 400nm samples before and after 150 minutes of illumination and after 1200 minutes of bleaching. Shorter wavelengths - thus higher energies (see formula 2.24) - are absorbed by the thin film since its energy is above the bandgap, leading to a low transmission of these wavelengths. For wavelengths corresponding to energies below the threshold value, the transmission never reaches 100% due to reflection from the silicon oxide substrate and the thin film. This reflection also interferes with the incident light, causing a wavelike pattern in the transmission spectrum.

Besides the usual wavelike transmission spectrum, both graphs show an additional peak between 380 and 400nm during illumination. The 0.8Pa sample's spectrum would indicate light emissions around this wavelength since the detected intensity is higher than the transmitted intensity. This peak can be attributed to the LED source illuminating the samples since it is visible in both the transmission and reflection spectrum during illumination.

During illumination, both the transmission and reflection gradually decrease over time. When applying equation 2.1, this means that the absorption increases. Montero-Amenedo [31] studied how an increased absorption increases the temperature of the thin film. This increased temperature, in combination with the environmental temperature, affects photochromic kinetics, accelerating the bleaching process. Therefore, the photo-darkening and bleaching effects are in a constant battle until an equilibrium state is reached, indicating the maximum photochromic contrast. Moreover, placing the sample in a higher temperature environment will impact photo-darkening and bleaching characteristics [16]. Baba et al. [3] reported that a YOH thin film will have a higher photochromic contrast when cooled down to a temperature of 5K compared to the contrast at room temperature.

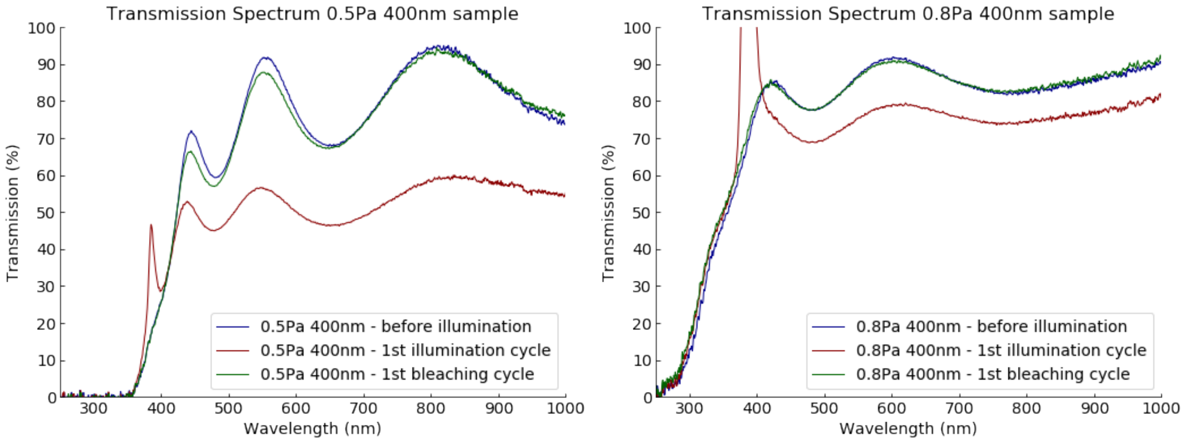

(a) 400nm thick sample deposited at 0.5Pa

(b) 400nm thick samples deposited at 0.8Pa

Figure 5.1: Transmission spectra of 400nm thick samples deposited at (a) 0.5Pa and (b) 0.8Pa, shown for three states: before illumination, after the first illumination cycle, and after the first bleaching cycle.

For the 0.5Pa sample, we observe that it has not fully bleached back to its original transparency. Similar research by Beek [5] showed that the 0.5Pa sample takes about 1200 minutes to return to its original state. Nevertheless, the samples used here are not exactly the same; hence, slight deviation may be allowed. On the other hand, the 0.8Pa sample has completely bleached back well within 1200 minutes.

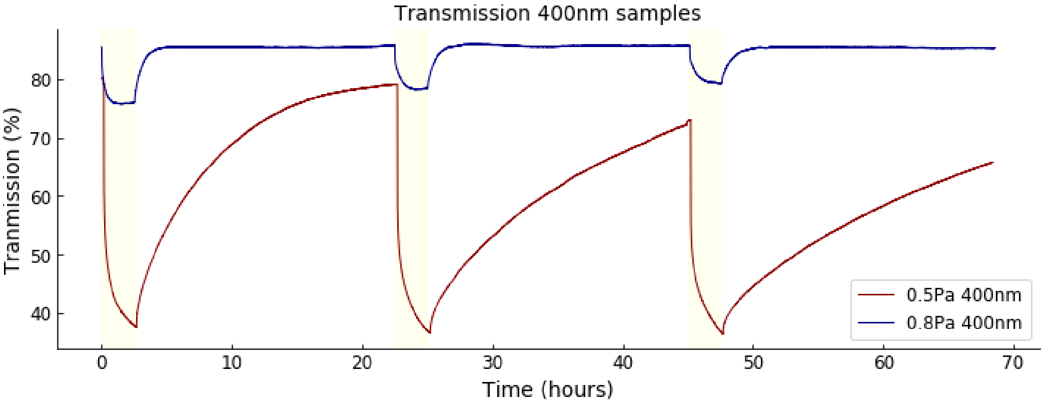

Figure 5.2: Transmission as a function of time for 400nm samples deposited at 0.5Pa and 0.8Pa, measured over three illumination cycles. The samples were illuminated for 2.5 hours and bleached for 20 hours per cycle.

The transmission data for both 400nm samples in figure 5.2 shows that the 0.5Pa sample exhibits a larger photochromic contrast. However, as discussed previously, it does not have time to fully bleach back to its original transparency within 20 hours. This effect is then magnified over multiple cycles with an increasing bleaching time. Moreover, a slightly higher photochromic contrast can be observed in each cycle. Since the transmission curve is not completely flat after each illumination cycle, we could argue that the maximum contrast has not yet been obtained. The decreasing darkening time constants, calculated using formula 2.17, of 20.6, 17.5 and 14.7 hours at the end of each illumination, respectively, indicate an increased photo-darkening activity at the end of each cycle. These characteristics suggest the presence of a memory effect [27]. In contrast to the 0.5Pa sample, the 0.8Pa sample shows a lower photochromic contrast but a faster bleaching time, which aligns with the expected behaviour (see section 2.2).

The higher oxidation grade in the 0.8Pa sample increased its transparency in the transparent state, compared to the 0.5Pa sample [55, 31]. While the 0.5Pa sample has a slight increase in photochromic contrast after multiple illumination cycles, we see a decrease in contrast for the 0.8Pa sample.

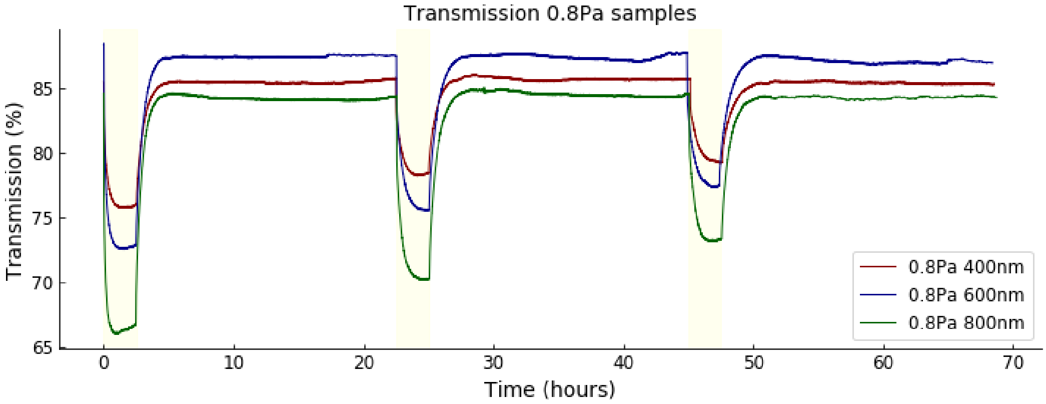

Figure 5.3: Transmission as a function of time for all three 0.8Pa samples, measured over three illumination cycles. The samples were illuminated for 2.5 hours and bleached for 20 hours per cycle.

Concerning the transmission data of the 0.8Pa samples with various layer thicknesses shown in figure 5.3, we can see a direct correlation between the thin film thickness and the induced photochromic contrast. This indicates that photochromic contrast is not only determined by the state of oxidation (i.e. deposition pressure) but also by the thickness of the film. This is expected since the light will have to travel through more material, increasing the absorption. Following this reasoning, we would expect a 400nm sample to have the highest transmission in the transparent state, which is not the case. However, slight deviations can be expected since not all layer depositions are 100% identical.

Besides its effect on the photochromic contrast, the film thickness could also affect the quality of the film. When looking at the 0.8Pa samples used in this research, the 800nm sample was visibly different from the other two. While the 400nm and 600nm samples showed a clear and transparent layer, the thicker 800nm sample was slightly more opaque, suggesting the presence of inhomogeneity. This is in line with the research by Montero-Amenedo [31], which states the relation between inhomogeneity and thicker films deposited at high pressures.

It was observed that the decreasing photochromic contrast upon cycling occurs in all samples deposited at 0.8Pa. Previous research by Moldarev et al. [26] investigated the interaction of YOH thin films with their surroundings and detected hydrogen effusion during illumination. All proposed mechanisms emphasise the critical role of hydrogen in maintaining the photochromic contrast. Based on our measurements, it could be reasoned that the amount of hydrogen in the samples decreases with each cycle, thereby reducing the contrast. However, the exact events leading to decreased photochromic contrast remain unknown.

Sample	1st Darkening	2nd Darkening	3rd Darkening
0.5Pa 400nm	$53.0^{1)} \pm 0.4\%$	$54.4^{1)} \pm 0.4\%$	$54.5^{1)} \pm 0.4\%$
0.8Pa 400nm	11.4 ± 0.4%	8.4 ± 0.4%	7.3 ± 0.4%
0.8Pa 600nm	18.0 ± 0.4%	14.4 ± 0.4%	12.4 ± 0.4%
0.8Pa 800nm	21.8 ± 0.4%	16.8 ± 0.4%	13.4 ± 0.4%

Table 5.1: Photochromic contrast from figure 5.4 for samples with different deposition pressures and thicknesses, measured across three darkening cycles. Errors of transmission measurement calculated with $\sigma = \frac{\mu}{SNR}$ [22]
$^{1)}$ Not fully bleached back

In figure 5.4a, we plotted the normalised photochromic contrasts resulting from our first type of measurement. The 0.5Pa sample shows a contrast comparable to the ≈49% findings of Mongstad et al. [27], who studied samples deposited at 0.4Pa. No directly comparable data for the 0.8Pa samples was found. However, previous research by Montero-Amenedo [31] indicates that a similar magnitude of the

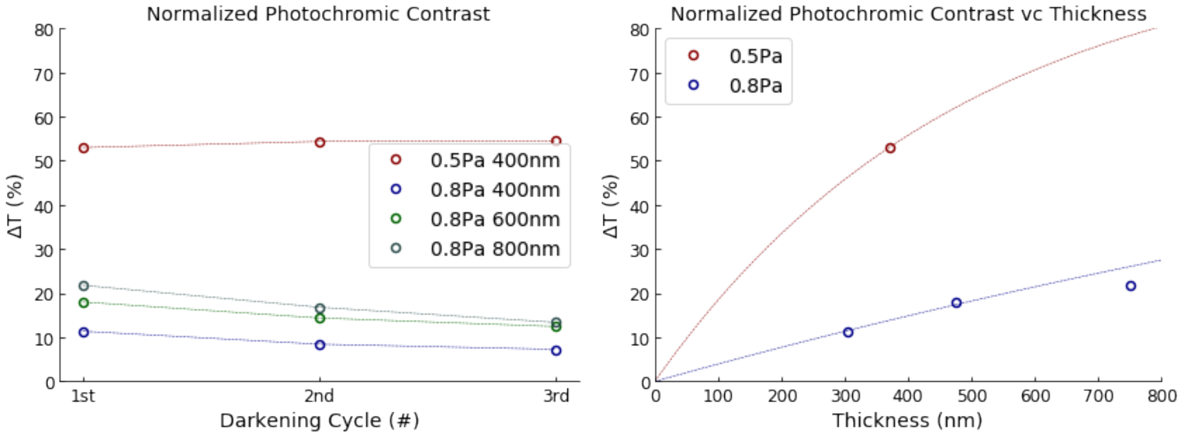

(a) Normalised photochromic contrast (ΔT) as a function of darkening cycles for samples with varying deposition pressures and thicknesses.

(b) Normalised photochromic contrast (ΔT) as a function of sample thickness for deposition pressures of 0.5Pa and 0.8Pa.

Figure 5.4: Combined analysis of normalised photochromic contrast (ΔT).

contrast can be expected considering other pressures and thicknesses.

When comparing the 0.8Pa samples, the photochromic contrast of the 400nm and 600nm align with what we would expect. The solid lines in figure 5.4b indicate the expected photochromic contrast compared to the sample thickness. This line uses the thinnest sample of both pressures as a reference point. As for the 800nm sample, the measured photochromic contrast is a bit lower than expected. Since the sample already looked different from the other two, a deviation in contrast could be expected.

The bleaching time constants for the first type of measurement are shown in figure 5.5. These constants were determined by plotting equation 2.14 and extracting the bleaching time constant by solving the gradient (appendix A.1). For all samples, the bleaching time constant increases after multiple cycles [11]. The 0.5Pa sample shows a more significant increase in absolute and relative terms compared to the 0.8Pa samples. The bleaching time constant for the 0.5Pa sample is of the same order of magnitude as previous research indicated [3, 5]. However, slight value differences could be attributed to variations in deposition chambers and measurement conditions.

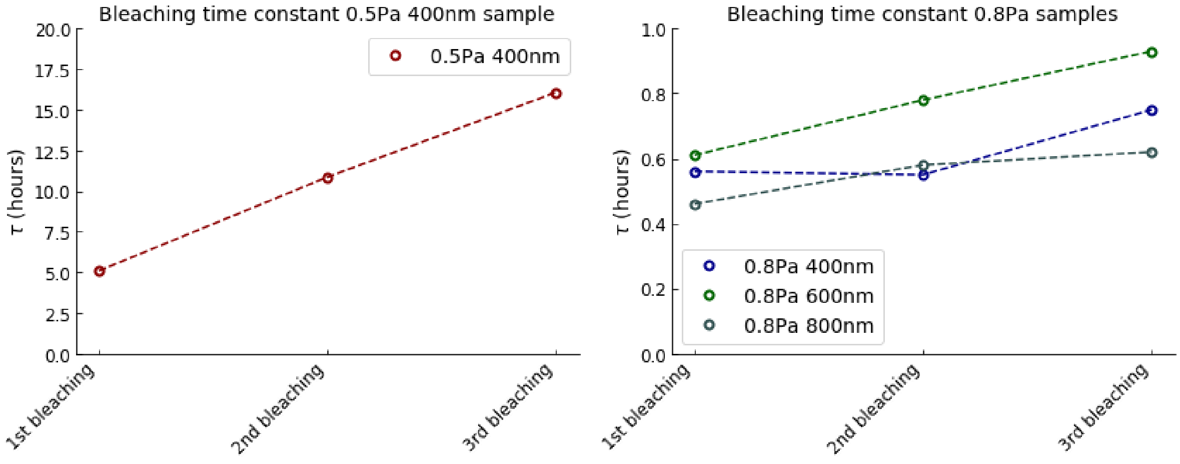

(a) 400nm thick sample deposited at 0.5Pa

(b) Samples deposited at a pressure of 0.8Pa

Figure 5.5: Bleaching time constants (τ_B) calculated using formula 2.14 for three bleaching cycles.

In contrast, the values of the time constants are much smaller for the 0.8Pa samples than for the 0.5Pa sample, as expected from previous studies [3]. This confirms that more oxygen beneficently affects the bleaching time constant [9].

The Tauc plots, used to determine the bandgap for each sample after photo-darkening and bleaching, are listed in appendix A.3. The calculated bandgaps for our samples were found to be 2.59 $\pm$ 0.03eV for the sample deposited at 0.5Pa and between 2.74 - 2.79eV for the samples deposited at 0.8Pa, with an equal error margin. These values are consistent with other studies, which show that the bandgap increases with the oxygen content in the sample.

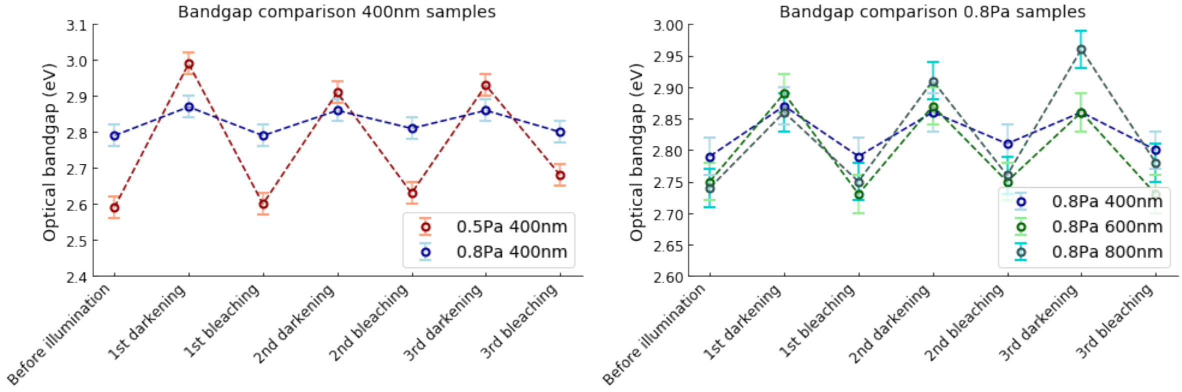

(a) 400nm thick samples

(b) Samples deposited at a pressure of 0.8Pa

Figure 5.6: Bandgap analysis for single-layer samples during three illumination cycles, determined using Tauc plots. Details on Tauc plot calculations can be found in appendix A.3.

Literature previously reported an approximate bandgap of about 2.6eV depending on the oxygen content of YOH samples [28]. Cornelius et al. [11] conducted experiments on the optical bandgap of YOH and found a bandgap of 2.6eV for $x = 0.7$ and 4.9 eV for $x = 1.4$, showing that the bandgap increases for higher oxygen content.

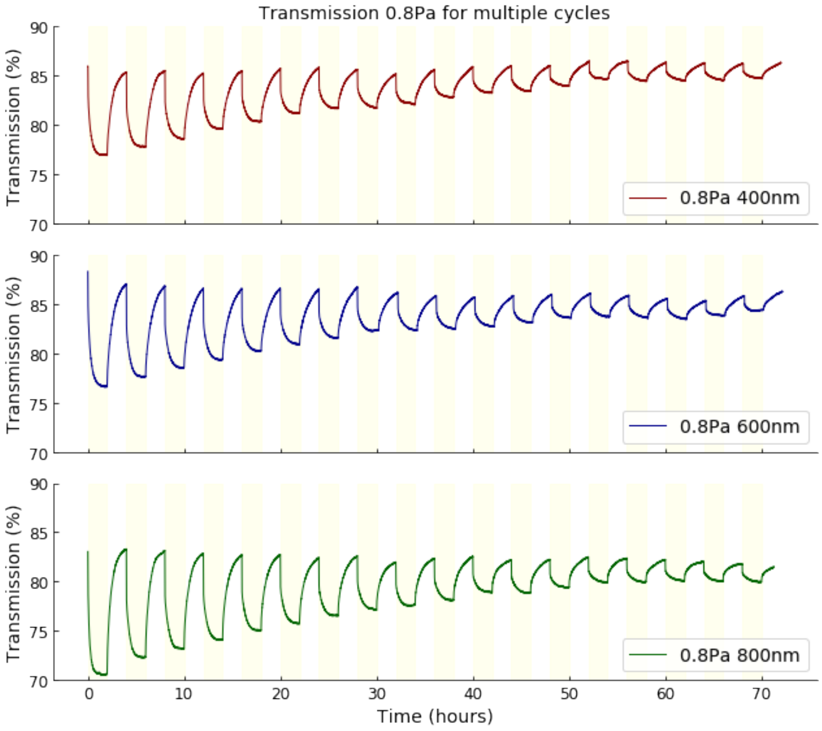

Figure 5.7: Transmission as a function of time for 0.8Pa samples with thicknesses of 400nm, 600nm, and 800nm over 18 illumination and bleaching cycles. Each cycle consists of 2 hours of illumination followed by 2 hours of bleaching.

Under illumination, a distinct rise in bandgap was seen in all samples. This increase is probably due to the Burstein-Moss effect described in section 2.4.2, where electrons are photo-excited to higher states, filling the conduction band's lower energy levels, thereby increasing the effective bandgap. The shift in bandgap is significant for the sample with low oxygen contents. The bandgaps before and after illumination are approximately equal for all of the 0.8Pa samples, consistent within the error margins. The only significant exception is the 800nm sample in the last photo-darkening cycle, which has a slightly higher bandgap than expected.

The second type of optical measurement (faster cycling) performed for the 0.8Pa samples is depicted in figure 5.7. As previously noted, a decrease in photochromic contrast is observed after multiple cycles for all thicknesses. This reduction in contrast continues for approximately 13–14 cycles, after which it appears to stabilise. The transmission in the transparent state remains constant, with only slight deviations that may be attributed to minor variations in the measurement environment.

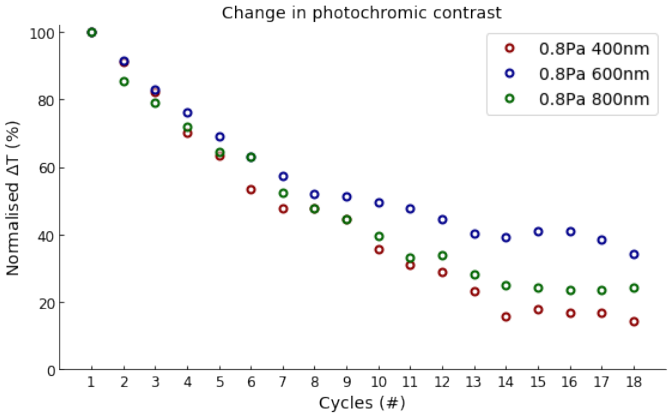

Figure 5.8: Relative decrease in photochromic contrast (ΔT) for 0.8Pa samples with thicknesses of 400nm, 600nm, and 800nm, normalised to the contrast observed in the first photo-darkening cycle, over 18 cycles from figure 5.7.

This decrease is normalised in figure 5.8 to the contrast observed in the first cycle to allow for comparison between the different samples. All samples exhibit a similar degradation pattern during the first nine cycles, after which minor deviations emerge. After 18 cycles, the samples stabilise between 20–40% of their initial photochromic contrast. However, additional cycles are necessary to draw more definitive conclusions.

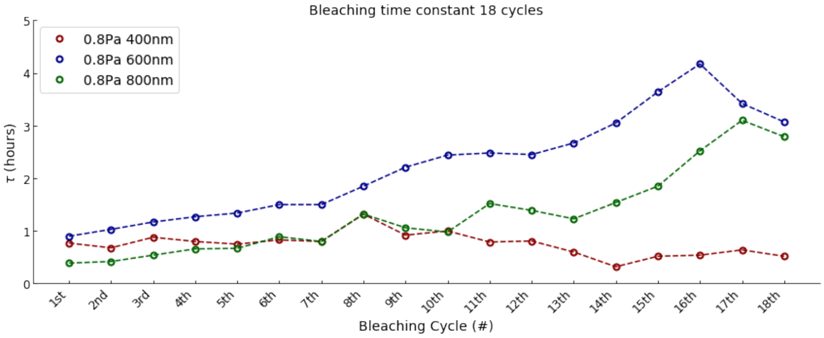

Figure 5.9: Bleaching time constants (τ_B) for 0.8Pa samples with thicknesses of 400nm, 600nm, and 800nm, observed across 18 bleaching cycles.

The bleaching time constants of the 600nm and 800nm samples increases gradually through the cycles—meaning the longer the cycles run, the longer it takes for the samples to bleach back to their original transparency. This bleaching time constant does not increase for the 400nm sample. The exact cause for this different behaviour remains unclear.

5.1.2. Double-layer Optical Measurements

The double-layer samples were first measured using the first type of measurement, consisting of three cycles. As discussed in section 3.1, we have two different double-layer samples. The first sample, referred to as DL-1 in the results, consists of a first layer deposited at 0.8Pa, followed by a second layer deposited at 0.5Pa. The second sample, DL-2, has the opposite layer order, with the first layer deposited at 0.5Pa and the second at 0.8Pa.

In figure 5.10, the transmission spectra for both double-layer samples are shown. When comparing both spectra, we see a big difference. The DL-2 sample has a transmission of 79.5 ± 0.2% in its transparent state, whereas the DL-1 sample has a significantly lower transmission of 31.6 ± 0.2%. Implying a difference of 47.9 ± 0.4% in transmission before any photochromic effects has occurred. We also measured the as-deposited single-layers within the double-layer sample separately, allowing us to make predictions about the expected transmission, and if the double-layers are described by stacking two single-layers on top of each other. The expected transmission can be obtained with the formula 5.2, which accounts for the substrate's contribution to the transmission of each single-layer sample. Since the single-layer samples have approximately the same thickness as the layers within the double-layer thin films, it is not necessary to account for thickness in the formula.

$$T_{DL} = (\frac{T_{0.5Pa}}{T_{substrate}} \cdot \frac{T_{0.8Pa}}{T_{substrate}}) \cdot T_{substrate} \tag{5.2}$$

In formula 5.2, the $T_{0.5Pa}$ and $T_{0.8Pa}$ parameters are the transmission for both single-layers and the $T_{substrate}$ is the substrates transmission, which is 93.1 ± 0.2%. Filling these values, we obtain an expected transmission of ≈73% in the transparent state.

Comparing the expected transmission to the measured value, we can conclude that the DL-2 sample has a higher transmission in the transparent state than expected. The transmission of DL-1, on the other hand, is much lower, which could be caused by inhomogeneity that occurs during the second layer's deposition.

The reflection is also reduced to 2.7 ± 0.2% in the DL-1 sample, which is lower than the ≈14% measured for the single-layer and DL-2 samples. This low transmission and reflection for the DL-1 sample would indicate a high absorption according to formula 2.1. This could be attributed to the top layer not being fully oxidised, partially consisting of metallic cluster ($YH_{2-\delta}$), which contributes to the observed absorption. Alternatively, part of this theoretical high absorption following from formula 2.1 could be attributed to the limitations of the measurement setup, which detects reflected light at a single point and does not account for light scattering caused by surface roughness.

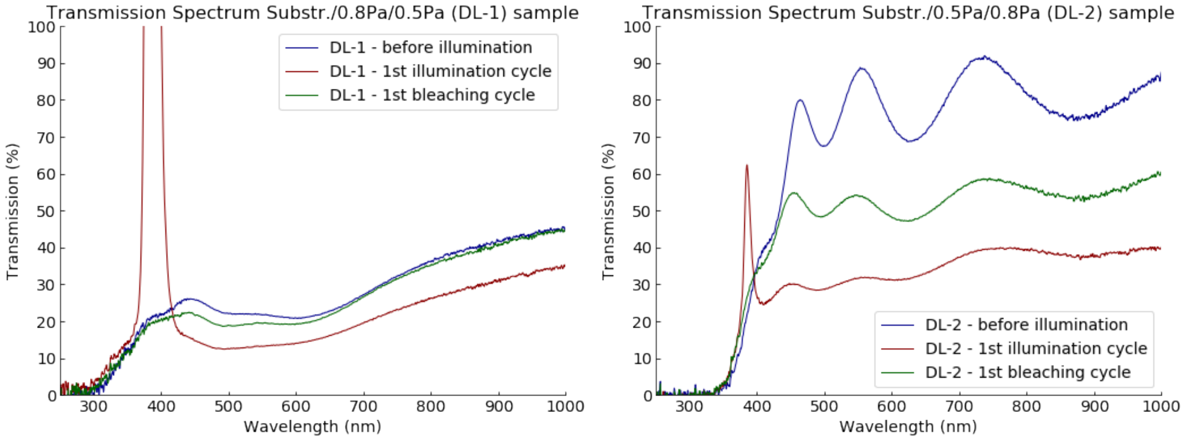

(a) 400nm thick sample deposited at 0.5Pa

(b) 400nm thick samples deposited at 0.8Pa

Figure 5.10: Transmission spectra of double-layer samples (a) substrate/0.8Pa/0.5Pa(DL-1) (b) substrate/0.5Pa/0.8Pa(DL-2), shown for three states: before illumination, after the first illumination cycle, and after the first bleaching cycle.

The transmission spectrum for DL-1 shows a small interference region between λ = 400 - 700nm, creating a wavelike pattern also visible in the single-layer samples (figure 5.1). However, no interference is observed at higher wavelengths. This could be attributed to the inhomogeneity of the sample (figure 3.2) and the distance between these inhomogeneous regions (d), limiting interaction between waves when the wavelength exceeds this distance ($\lambda > d$). On the other hand, the DL-2 sample does show a wavelike pattern for the complete wavelength spectrum. The interference fringes are placed closer when compared with the 400nm samples in figure 5.1. This aligns with the expectation that thicker samples have more closely spaced fringes, which is also observed in the thicker 0.8Pa samples. Additionally, during illumination, we see the peak of the LED light around 385nm for both illumination spectra, just as we observed for the single-layer samples.

After illumination, the DL-1 sample fully bleaches back to its original transparency, whereas the DL-2 sample is only halfway through its bleaching process after 20 hours. Slow bleaching, where samples do not fully bleach back after 20 hours, was also observed for 0.5Pa samples in this and previous research [5], although not to this extent.

In figure 5.11, we see the three-cycle measurement for both double-layer samples and the expected contrast of a combined 0.5Pa and 0.8Pa layer according to the three-cycle measurement of the two separate single-layers. Figure 5.12b shows these measurements and the expected combined transmission curve. This curve of the double-layer was calculated using the formula 5.2. Comparing all three curves, a clear resemblance between the DL-2 sample and the expected curve is seen. As expected from the big difference in its transparent state transmission, the DL-1 sample follows a different trend, incomparable to the expected transmission curve.

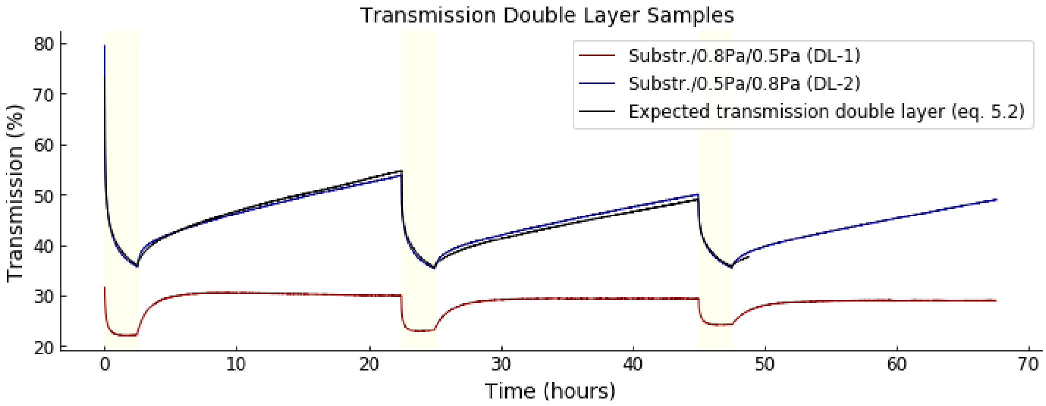

Figure 5.11: Transmission as a function of time for double-layer samples, measured over three illumination cycles. The samples were illuminated for 2.5 hours and bleached for 20 hours per cycle.

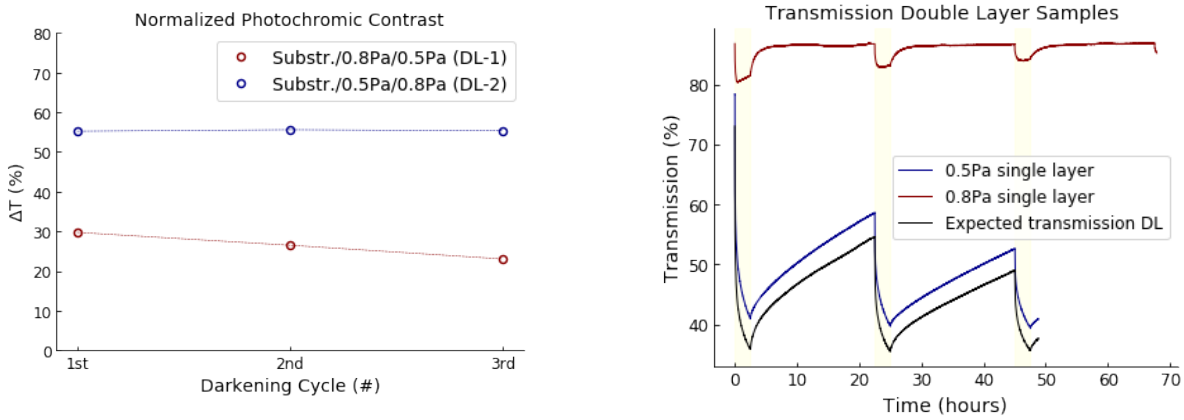

(a) Normalised photochromic contrast (ΔT) as a function of darkening cycles for samples with varying deposition pressures and thicknesses.

(b) Construction of expected transmission for double-layer samples following formula 5.2.

Figure 5.12: Combined analysis of normalised photochromic contrast (ΔT) and transmission for double-layer samples.

Upon closure inspection of the DL-1 sample, we see a decreasing photochromic contrast after each cycle, revealing the influence of the 0.8Pa layer on the photochromic contrast. This same decrease is not visible in the DL-2 sample, which shows a constant contrast of ≈55.2% for all three cycles, while not fully bleaching back after 20 hours. The measured constant contrast may result from the simultaneous increase and decrease in contrast of the 0.5Pa and 0.8Pa single-layers, respectively. The darkening time constant for DL-2 remains almost constant at the end of all illumination cycles, with values of 25.8, 25.6 and 27.5 hours for the three cycles, respectively. This is not in line with the previously observed decreasing darkening constant in figure 5.2. However, the 0.5Pa single-layer sample, which represents the first layer of DL-2, has a similar trend as its associated double-layer sample, with darkening time constants of 19.7, 21.4 and 20.5 hours.

Besides the photochromic contrast, we see some similarities with the single-layer samples during bleaching. Both samples show bleaching characteristics corresponding to the first deposited layer. The DL-1 sample returns to its original transparency within a few hours, although its bleaching time (5.8 hours) and time constant (1.6 hours) are slightly longer than those of the 0.8Pa single-layer sample (4.0 hours and 1.0 hour, respectively). In contrast, the DL-2 sample takes longer and is only halfway after 20 hours, consistent with the 0.5Pa single-layer sample. In terms of bleaching time constant, an increase is measured for the DL-2 sample compared to the 0.5Pa single-layer sample, as is depicted in figure 5.13.

It is evident that both double-layer samples primarily exhibit the characteristics of their first layer. The DL-1 sample has lower photochromic contrast and a fast bleaching process, while the DL-2 sample has a high contrast and a long bleaching process. However, the low overall transmission of sample DL-1 cannot be explained in this way.

Sample	**1st Darkening**	**2nd Darkening**	**3rd Darkening**
Substrate/0.8Pa/0.5Pa (DL-1)	29.7 ± 0.4%	36.5 ± 0.4%	23.1 ± 0.4%
Substrate/0.5Pa/0.8Pa (DL-2)	$55.2^{1)}$ ± 0.4%	$55.6^{1)}$ ± 0.4%	$55.4^{1)}$ ± 0.4%

Table 5.2: Photochromic contrast from figure 5.11 for double-layer samples, measured across three darkening cycles. Errors of transmission measurement calculated with $\sigma = \frac{\mu}{SNR}$ [22]
$^{1)}$ Not fully bleached back

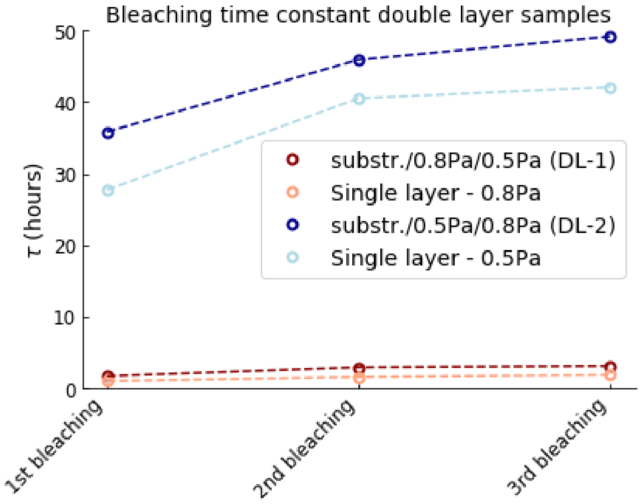

Figure 5.13: Bleaching time constants (τ_B) calculated using formula 2.14 for three bleaching cycles.

Figure 5.14 shows the bandgap for the DL-1 sample, which looks inconsistent and low compared to the single-layer samples from figure 5.6. These bandgaps are determined using the transmission and reflection data from the PHOCS setup. As we already discussed, there may be an error in the reflection data of sample DL-1 since the scattered reflection has not been detected. This would mean that the absorption coefficient was overestimated, leading to a reduction in the bandgap calculated using the Tauc plot method (equation 2.20). Besides this slightly uncertainty in the data, we see a clear trend, where the bandgap increases during illumination.

The DL-2 sample shows a constant bandgap of approximately 2.76eV in its transparent state. During illumination, the bandgap increases due to the Burstein-Moss effect, which was also observed in the single-layer samples. This bandgap aligns with the 0.8Pa single-layer samples, indicating a higher oxidation grade. During illumination, the bandgap increases to approximately 2.95eV, matching the bandgap of the 0.5Pa 400nm samples after illumination (figure 5.6).

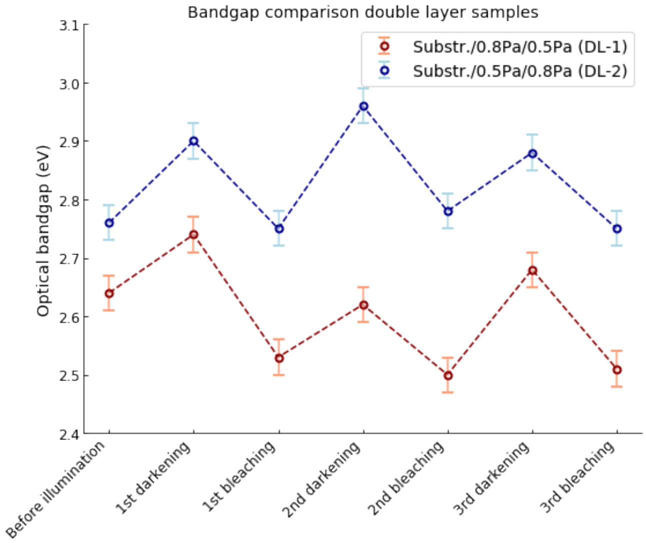

Figure 5.14: Bandgap analysis for double-layer samples during three illumination cycles, determined using Tauc plots. Details on Tauc plot calculations can be found in appendix A.3.

Due to decreased photochromic contrast in the DL-1 sample, we also performed a multiple short-cycle measurement (second type) on the DL-1 sample. Due to complications with the LED source, which disconnected from the computer during the measurement, the program was aborted after 11 cycles. This, however, still allowed us to investigate the degradation trend in the thin film.

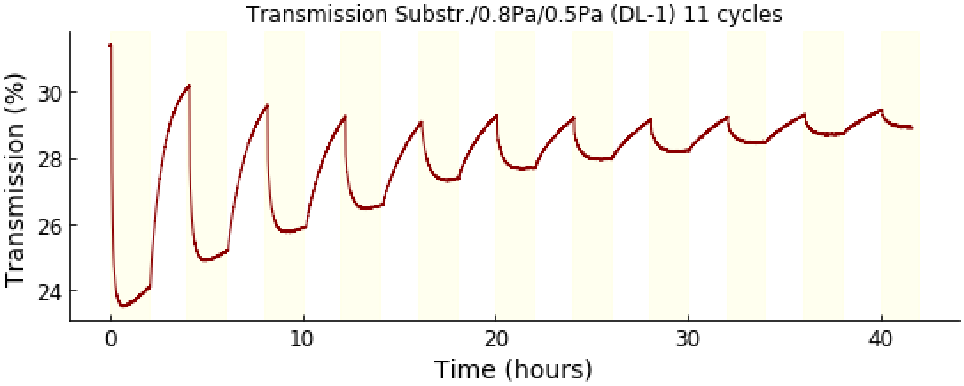

Figure 5.15: Transmission for substrate/0.8Pa/0.5Pa (DL-1) as a function of time over 11 illumination and bleaching cycles, with each cycle consisting of 2 hours of illumination and 2 hours of bleaching.

The decreasing contrast from the single-layer samples in figure 5.8 was fitted in Python using a five-component polynomial function. The resulting polynomial is given by equation 5.3 and shown as a red line in figure 5.16.

$$y = 1.128827 - 0.138234x + 0.012316x^2 - 0.000861x^3 + 0.000035x^4 \tag{5.3}$$

We observe that the DL-1 sample has approximately the same layer degradation as the 0.8Pa samples, underlining the influence of the 0.8Pa layer (the first layer) on the sample's photochromic contrast. Since the photochromic contrast of the DL-1 sample decreases so significantly, we may wonder if the deposited 0.5Pa layer has any photochromic effects since we expect these effects to significantly contribute to the contrast and not diminish over time. Additionally, the 0.5Pa layer would take significantly longer to bleach back to its transparent state compared to the DL-1 sample.

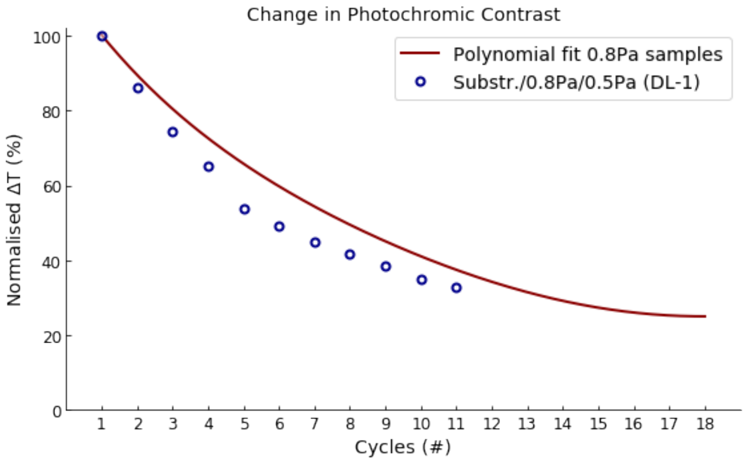

Figure 5.16: Relative decrease of photochromic contrast for the Substrate/0.8Pa/0.5Pa (DL-1) sample in figure 5.7, normalised to the contrast observed in the first photo-darkening cycle. The contrast decrease is compared to the polynomial representation of the decrease in the 0.8Pa samples.

The bleaching time constant for the double-layer sample after multiple cycles is visible in figure 5.17 and increases more rapidly than for the 0.8Pa samples.

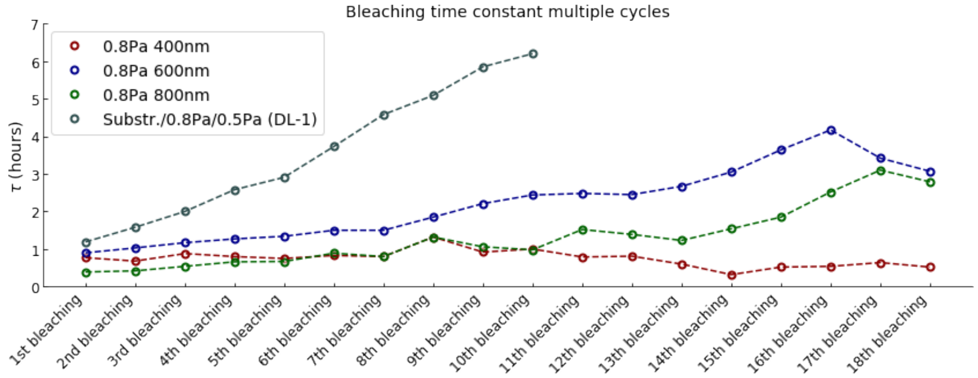

Figure 5.17: Bleaching time constants (τ_B) for double-layer sample DL-1 and single-layer samples with thicknesses of 400nm, 600nm, and 800nm, observed across the 1st to 10th bleaching cycles.

5.2. Spectroscopic Ellipsometry

The Spectroscopic Ellipsometry (SE) measurements were conducted before and after illumination, as well as at specific time intervals during illumination. In this study, we measure the thin film at intervals of 10, 30, 60, 90, 120, and 150 minutes of illumination. These intervals were selected to enable direct comparison with prior research by Beek [5]. To prevent possible interference, the LED light was turned off for 2 minutes at the end of each interval to measure during photo-darkening. Although this pause introduces a slight break in the illumination, and the thin film undergoes bleaching in this brief interval, the short bleaching of the film is expected to have minimal impact on the measurements.

As discussed in section 4.3.2, the EMA model will be used for analysing the photo-darkened states. This EMA model combines the B-spline or Cauchy-fitted transparent state sample with the presence of metallic clusters and voids. While the SE model for voids is already available within the modelling software, the metallic clusters are not. To determine the fraction of metallic clusters in the sample, we have the option to select from the optical parameters corresponding to three metallic compositions, namely Y, YH_2, and YH_x, which were already measured and subsequently modelled in previous research. Beek examined the resulting Mean Squared Error (MSE) for each of these three models and concluded that the photo-darkened EMA layer is best modelled with the presence of YHx metallic clusters. Additionally, Beek researched these models with and without voids and found that the YH_x model including voids provided the best approximation.

5.2.1. Substrate

As previously mentioned, fused silica is used as the substrate. The CompleteEase software enables modelling of the substrate to accurately represent the thin film and substrate system. This is most effectively achieved by first measuring the substrate without any deposition, allowing for precise identification of the substrate's contribution to the measurement. Similar to the transparent YOH layer, the fused silica is best estimated with the Cauchy model, resulting in A = 1.445 and B = 0.00428. This indicates a refractive index n of close to 1.445, as A provides a good approximation for n. This result is in line with the theoretical refractive index of fused silica, which ranges between 1.4446 and 1.4878 across wavelengths of 300–1500nm [44, 24].

5.2.2. Single-layer Spectroscopic Ellipsometry

As mentioned in section 4.3.1, the ellipsometry measurements were performed between $60°$ and $70°$ in steps of $5°$. The setup then measures the Ψ and Δ values over this angle range for different wavelengths in the range of 300-1500nm, whose profiles are depicted in figure 5.18. It is observed that measurements at two angles ($60°$ and $70°$) give rise to almost identical patterns over the complete wavelength range, whereas one angle ($65°$) displays a pattern different from the other two, confirming the presence of the Brewster angle near the middle of our angle range. As discussed in section 2.6.4, the theoretical value of this Brewster angle is located at $65°$, confirming our measurement.

Besides the measured Δ and Ψ values, visible in figure 5.18, our model is also displayed and indicated by the dotted line. The 0.8Pa samples of 400nm and 600nm were fitted using a Cauchy and Gen-Osc model in the transparent state. The Cauchy model was combined with an Effective Medium Approximation (EMA) model to model the photo-darkened states. Meanwhile, the samples of 0.5Pa 400nm and 0.8Pa 800nm were fitted using the EMA model during photo-darkening, with a B-spline in a transparent state. A schematic drawing of these models is depicted in figure 5.19. The 800nm sample, however, was more problematic to fit due to the inhomogeneity of the sample, which was also observed visually.

For the Cauchy models, we obtained A = 1.793 and A = 1.784 for the 400nm and 600nm samples, respectively. These values are slightly lower than the A value of 1.881 reported in previous studies by Montero [29] and Beek [5] for 0.5Pa samples, indicating a somewhat lower refractive index approximation. The same samples were also modelled using oscillators, specifically the Lorentz (LO) and Tauc-Lorentz (TLO) oscillators [29, 30, 5, 55]. Additionally, the photo-darkened states of the 0.5Pa 400 nm sample were modelled using four Gaussian (GO) and one Drude (DO) oscillator [55]. The same article also recommended using one TLO and one GO for the transparent state; however, this approach yielded no successful results.

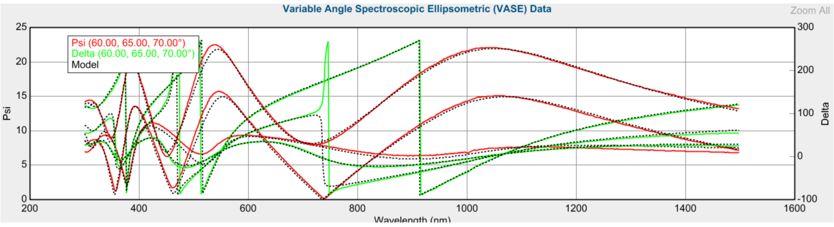

(a) Δ and Ψ fit before illumination, with a MSE of 12.94

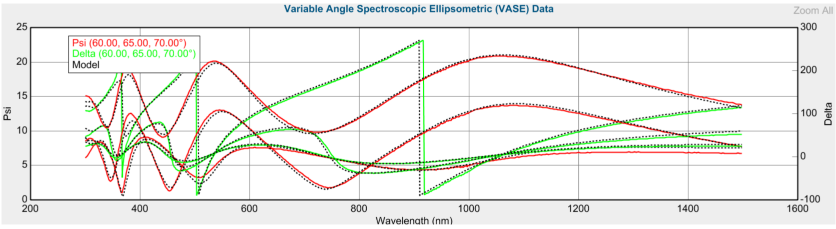

(b) Δ and Ψ fit after 150 minutes illumination, with a MSE of 13.92

Figure 5.18: Two CompleteEase Software fits for the 0.8Pa 400nm sample, using a Cauchy EMA layer.

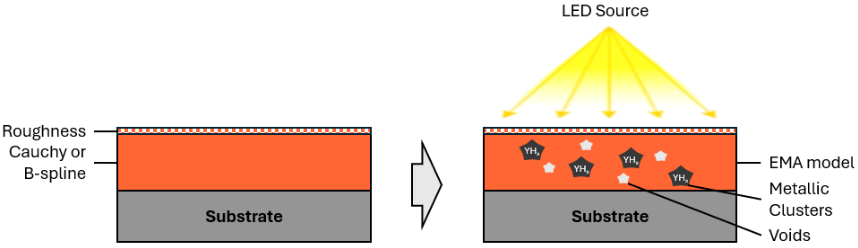

Figure 5.19: Schematic model of single-layer samples used in the CompleteEase software, illustrating the initial layer with roughness modelled by Cauchy or B-spline and the illuminated layer with an EMA model containing metallic clusters.

Sample	Model	Parameters	Thickness (nm)	Roughn. (nm)	MSE
0.5Pa 400nm	B-spline	–	376.9	11.7	11.64
	GenOsc$^{1)}$	1 DO, 4 GO	416.8	14.4	12.69
0.8Pa 400nm	Cauchy	A = 1.793, B = 0.01408	339.6	10.2	12.94
	GenOsc	1 TLO, 1 LO	338.7	9.9	13.35
0.8Pa 600nm	Cauchy	A = 1.784, B = 0.01521	480.8	9.8	13.82
	GenOsc	1 TLO, 1 LO	480.1	10.1	14.96
0.8Pa 800nm	B-spline	–	754.9	15.0	40.19

Table 5.3: Model parameters and characteristics for various samples in transparant state, including thickness, roughness, and mean squared error (MSE) values. The models used include Tauc-Lorentz Oscillator (TLO), Lorentz Oscillator (LO), Gaussian Oscillator (GO), and Drude Oscillator (DO).
$^{1)}$ Only found acceptable model between 30 and 150 minutes (MSE at 30 minutes).

The optical constants for the 0.8Pa 400 nm sample using the EMA model are presented in Figure 5.20. The extinction coefficient k for the transparent states (0 min and bleached) is lowest and approaches zero beyond 500 nm, which indicates minimal light absorption in these states. This is in line with the transparency of these states, as lower k values correspond to reduced film absorption.

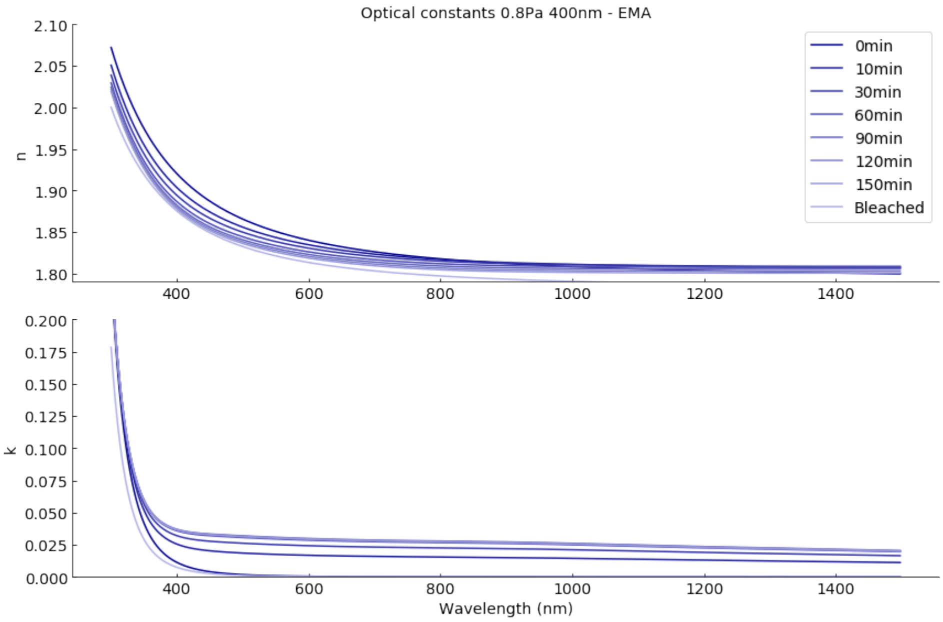

Figure 5.20: The optical constants $n(\lambda)$ and $k(\lambda)$, determined using Cauchy and EMA layers, respectively, before, during, and after illumination for the 0.8Pa 400nm sample.

During optical measurements, a reduction in transparency was observed, primarily attributed to increased absorption (section 5.1.1). This relationship is reflected in the rising k values at high wavelengths as illumination progresses. Furthermore, the convergence of k near the bandgap wavelength ($\lambda \approx$ 450nm) confirms that the film absorbs strongly for wavelengths below this threshold, as theoretically expected.

The refractive index n for $\lambda \lesssim$ 650nm appears to decrease during illumination and does not fully recover upon complete bleaching. This behaviour is consistent with observations reported by Beek [5], who analysed the same time intervals. Comparatively, the n values are lower than those reported by Beek [5], which aligns with studies by Colombi et al. [8] and Zubkins et al. [55], given that the higher deposition pressure used in this work results in increased oxygen content within the sample.

It should also be noted that unlike the research conducted by Beek [5] and Montero [29], the majority of prior ellipsometry measurements have been performed solely in the transparent state. Consequently, these studies report k values approaching zero for $\lambda \gtrsim \lambda_{gap}$, indicating the absence of absorption in this wavelength range.

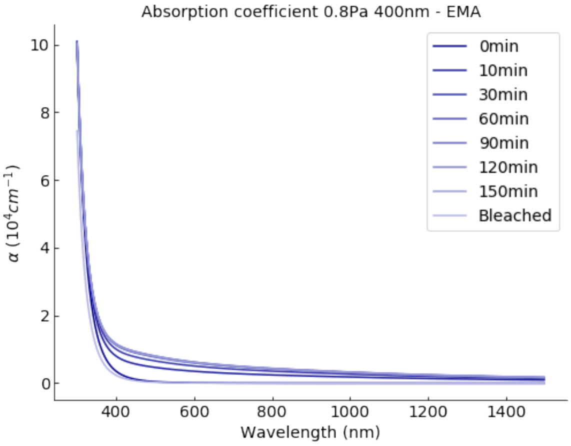

Figure 5.21: Absorption coefficient $\alpha(\lambda)$ determined using the complex refractive index from figure 5.20 and formula 2.21 for the 0.8Pa 400nm sample.

The absorption coefficient graph for the 0.8Pa, 400 nm sample under the EMA model is shown in figure 5.21. The measured k-value can be used to derive the absorption coefficient since the two are linked through equation $\alpha = \frac{4\pi k}{\lambda}$. In addition, we find an absorption coefficient close to zero for longer wavelengths since the modelled k also approaches zero for these wavelengths.

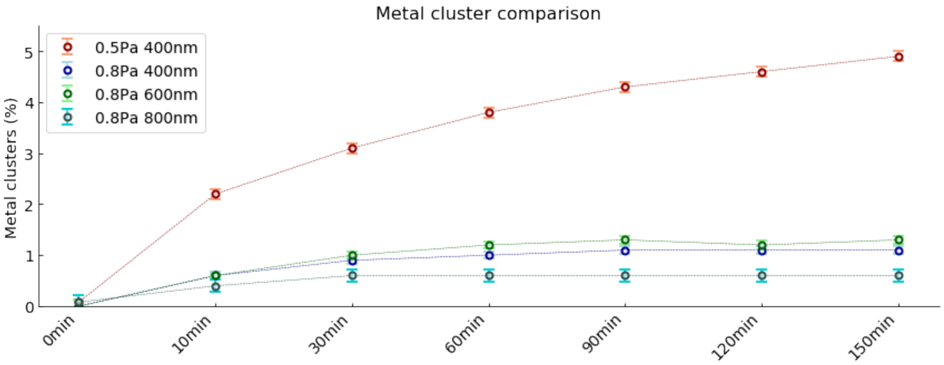

(a) Percentage of metal clusters determined using the EMA model for all four samples, measured over time during illumination.

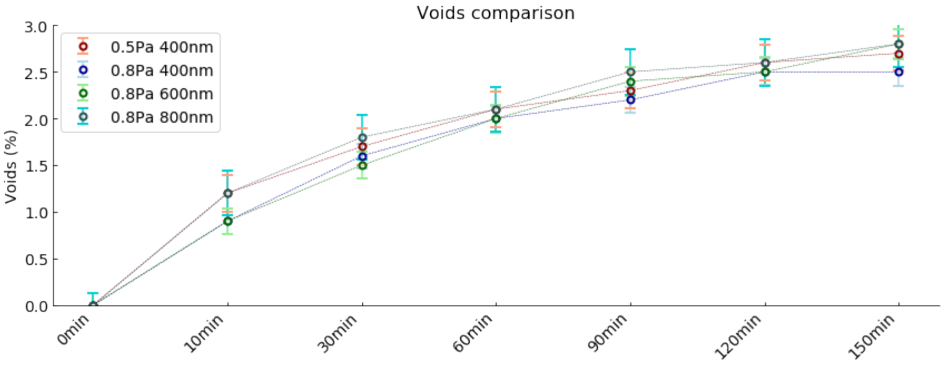

(b) Percentage of voids determined using the EMA model for all four samples, measured over time during illumination.

Figure 5.22: Comparison of metal clusters and voids percentage determined using the EMA model for samples with different thicknesses (400nm, 600nm, and 800nm) deposited at 0.5Pa and 0.8Pa, measured over 150 minutes.

The YH_x metallic cluster fraction and void content of the 0.5Pa 400nm sample were analysed with the EMA model. The metallic domains percentage was modelled at 2.2% after 10 minutes of illumination, increasing to 4.9% after 150 minutes. The MSE of this model averaged around 23.2, indicating an acceptable fit with the measured data. These results are consistent with those reported by Montero et al. [30], where the YOH sample showed an increase in the modelled fraction of metallic clusters to 2% and 6% after 8 and 64 minutes of illumination, respectively.

Moreover, the spectroscopic ellipsometry data for both the 0.8Pa 400nm and 600nm samples were modelled in the same way, resulting in a fraction of 0.6% metallic clusters after 10 minutes of illumination, which, after 150 minutes, increased to 1.1% and 1.3%, respectively. The EMA model for the 400nm and 600nm samples had a good MSE, averaging 11.9 and 14.2, respectively. The metallic fraction after illumination is lower than the 0.5Pa samples, corresponding to the lower photochromic contrast. The 800nm sample showed a significant MSE during modelling and ended up with a lower metallic cluster percentage of 0.6% after illumination.

The modelled metallic clusters over time are depicted in figure 5.22a, and the modelled voids in figure 5.22b. According to the results of this model, the thin film's fraction of voids is not dependent on the deposition pressure. The voids content is modelled at $\approx$ 1% after 10 minutes and increases to $\approx$2.8% after 150 minutes of illumination This is slightly lower than Beek's model [38], who observed an increase to 4% after a full illumination cycle of 150 minutes. It should be noted that these are only models and in no way a 100% correct observation of the materialistic properties. While various models may provide an acceptable fit to the data, not all represent feasible real-world materials.

The EMA model can be used to determine the metallic cluster percentage during illumination since it uses the initial transparent Cauchy model as a base for YOH. This, however, prevents us from looking at the metallic clusters in the thin film in its transparent state. We know this percentage will be close to zero, and we can try to make an estimation linking the absorption coefficient to the metallic cluster fraction with formula 5.4. This formula is an adaptation of formula 2.11. An indication of the metallic cluster content at 0min in figure 5.22a is then made by: $f_0 = \frac{\alpha_0}{C}$

$$\Delta\alpha = C \cdot f_m \tag{5.4}$$

Using the constant C, this equation links the metallic cluster fraction (f_m) to the change in absorption coefficient ($\Delta\alpha$). The absorption coefficient in this formula can be obtained from the SE measurements just as we have done in figure 5.21, and by analysing the optical measurements from section 5.1 using equations 2.1 and 2.2. Detailed absorption coefficients for the corresponding time intervals from SE and optical measurements are provided in B.2 and A.6, respectively. The $\Delta\alpha$ is then calculated by the difference in absorption coefficient between 450 and 1000nm.

When considering photochromic materials, a nearly linear connection is expected as we look at the photochromic contrast and metallic clusters percentage when the photochromic contrast is low ($\frac{\Delta T}{T} \ll 1$). Combining equation 2.9 and 5.4 gives:

$$f_m = \frac{1}{dC} ln(\frac{1}{1 - \frac{\Delta T}{T}}) \tag{5.5}$$

Figure 5.23 plots the modelled metallic cluster content versus photochromic contrast for the different samples. It is observed that, for the 0.8Pa samples, the thin film reaches its maximum photochromic contrast and metallic cluster percentage after 60 minutes of illumination. Equation 5.5 indicates that the photochromic contrast initially increases linearly with small metallic cluster percentages before an additional quadratic term sets in. This linear relationship is visible in the 0.8Pa samples, while the quadratic correction begins to appear in the 0.5Pa sample. The fitted curves based on equation 5.5 are also displayed in the figure. The SE curve for the 0.8Pa 800nm sample is missing due to the high MSE in the model.

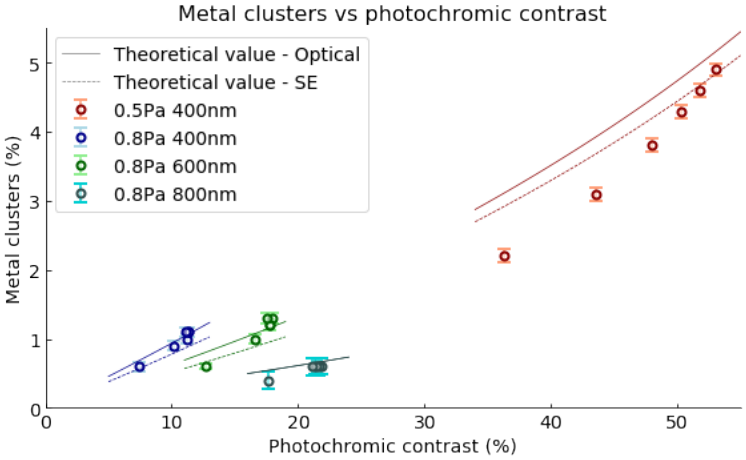

Figure 5.23: Comparison of metal clusters versus photochromic contrast for samples with different thicknesses and deposition pressures. The theoretical values from both optical and Spectroscopic Ellipsometry (SE) measurements are also plotted for reference using formula 5.5.

The C-values are presented in table 5.4 and for the first three samples range between $3.55 \cdot 10^7 m^{-1}$ and $4.02 \cdot 10^7 m^{-1}$ for the optical measurements, and between $4.29 \cdot 10^7 m^{-1}$ and $4.44 \cdot 10^7 m^{-1}$ for the SE

Sample	C**-values Optical** ($10^7 m^{-1}$)	C**-values SE** ($10^7 m^{-1}$)
0.5Pa 400nm	4.02	4.29
0.8Pa 400nm	3.69	4.44
0.8Pa 600nm	3.55	4.31
0.8Pa 800nm	5.58	$2.12^{1)}$

Table 5.4: Resulting C-constant from formula 5.5 for single-layer samples in figure 5.23. The different C-values are calculated with the absorption coefficient resulting from the optical (appendix A.6) and spectroscopic ellipsometry measurements (appendix B.2), respectively.

$^{1)}$ Not visible in figure 5.23 due to high MSE.

measurements. Since the C-value directly relates to the metallic cross-section (σ), we can confirm that the cross-section of for the first three samples is approximately constant. The 800nm sample exhibits a higher and lower C-value for the optical and SE measurement, respectively.

Since we saw a decline in photochromic contrast after a certain amount of cycles, we decided to measure some older samples, which had already been through multiple illumination cycles. After performing the type 1 and 2 optical measurements, we performed one additional measurement using the SE setup.

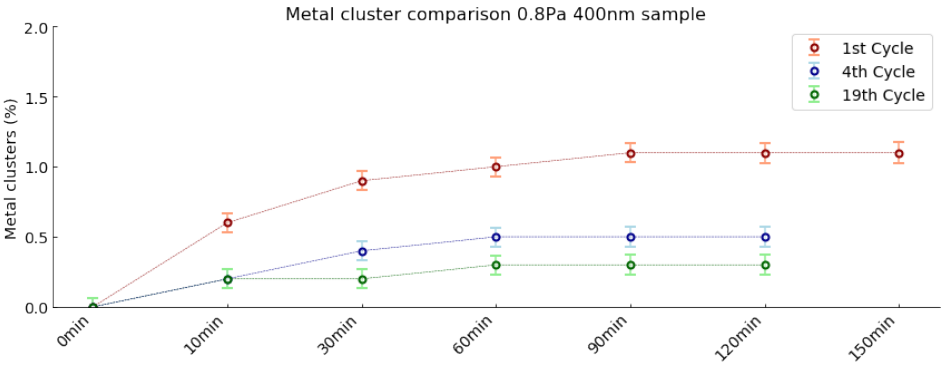

(a) Percentage of metal clusters determined using the EMA model for a 0.8Pa 400nm sample, measured across the 1st, 4th, and 19th cycles.

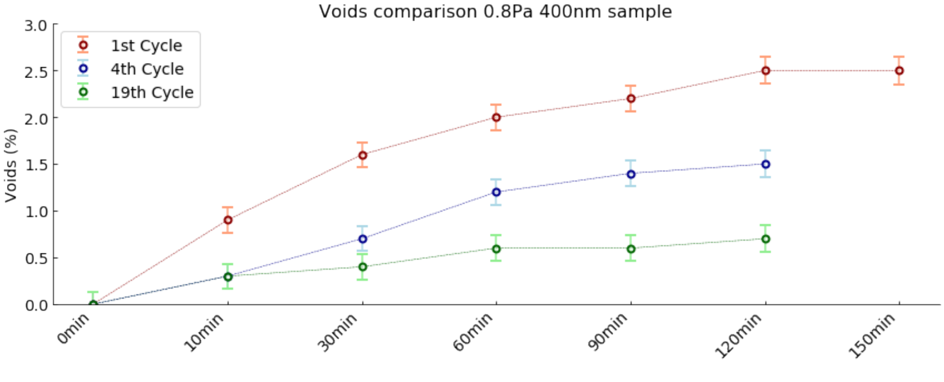

(b) Percentage of voids determined using the EMA model for a 0.8Pa 400nm sample, measured across the 1st, 4th, and 19th cycles.

Figure 5.24: Comparison of metal clusters and voids percentage for a 0.8Pa 400nm sample, determined using the EMA model across the 1st, 4th, and 19th cycles.

These results are depicted in figure 5.24, showing a decreasing metallic cluster percentage after multiple cycles. After 120 minutes of illumination, the metallic cluster percentage decreased from 1.1% to 0.5% and 0.3% for the 4th and 19th illumination cycle, respectively.

Since the photochromic contrast of the fourth cycle is 70% of the first cycle (figure 5.8), we can determine the expected metallic cluster percentage using equation 5.5. Filling in this equation for both obtained C-values gives and expected percentage range of 0.56-0.68%, close to the modelled 0.5%. As for the older sample, which has already been through 19 cycles, the expected metallic cluster percentage ranges between 0.11-0.14%, slightly lower than the modelled 0.3%. A similar decrease is seen for the modelled voids after multiple cycles. During the SE measurements, it was not possible to obtain the transmission directly. Therefore, the photochromic contrast of samples from the same batch was used to enable the application of equation 5.5.

5.2.3. Double-layer Spectroscopic Ellipsometry

We could not retrieve data from the DL-1 sample during the spectroscopic ellipsometry measurements on the double-layer samples. This is a consequence of the low reflection of the sample, leading to a too low intensity at the detector, preventing the extraction of the Ψ and Δ data. The SE results will, therefore, be limited to the DL-2 (substrate/0.5Pa/0.8Pa) sample only. The measured Ψ and Δ are depicted in figure 5.25 for both the transparent and photo-darkened states.

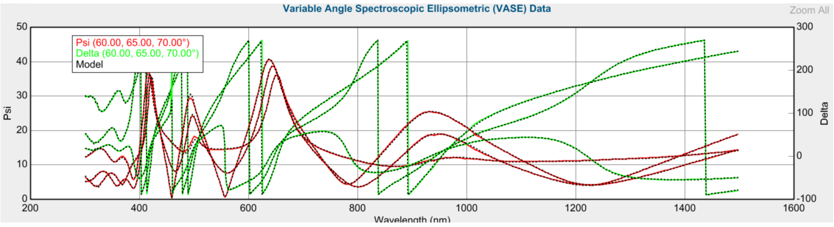

(a) Δ and Ψ fit before illumination, with a MSE of 7.32

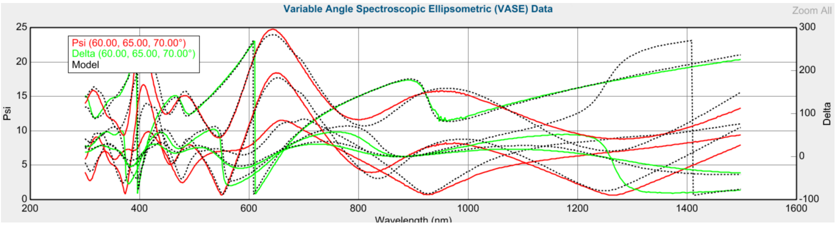

(b) Δ and Ψ fit after 150 minutes illumination, with a MSE of 34.13

Figure 5.25: Two ComepleteEase Software fits for the substrate/0.5Pa/0.8Pa (DL-2) sample made before and after illumination using a Cauchy EMA layer

The dotted line in the figure indicates the model we used to fit our measurement. In creating the transparent state model, we also measured the single-layer thin films, which the double-layer is composed of, separately. This provided a B-spline and Cauchy model for the 0.5Pa and 0.8Pa thin film, respectively. Combining these models to analyse the double-layer sample resulted in an unacceptable MSE. We eventually used three layers for the optimal model, all visible in figure 5.26. The 0.8Pa and 0.5Pa layers are modelled using a Cauchy layer, whereas an additional third boundary B-spline layer is inserted between the 0.5Pa and 0.8Pa layer to optimise the model.

The resulting models and their important parameters are presented in table 5.5. We modelled the single 0.5Pa layer with a B-spline, while the 0.5Pa layer in the double-layer sample was modelled more effectively with the Cauchy model. The attempt to model the single 0.5Pa layer using a combination of a Cauchy layer and a B-spline layer did not yield a comparable model.

The model's thickness indicates that the modelled boundary layer corresponds to the top of the 0.5Pa layer, which could be modified by the deposition of the 0.8Pa layer. The reason why the deposition would affect the top layer is unclear, and it seems more likely that the roughness layer of ≈10nm on top of the 0.5Pa layer has a disordering effect on the base of the 0.8Pa layer, creating the boundary layer of ≈40nm. Since we are working in a model, the exact physical location of the boundary remains unknown.

The A-parameter for the 0.8Pa top layer is approximately constant in both models, with a value between

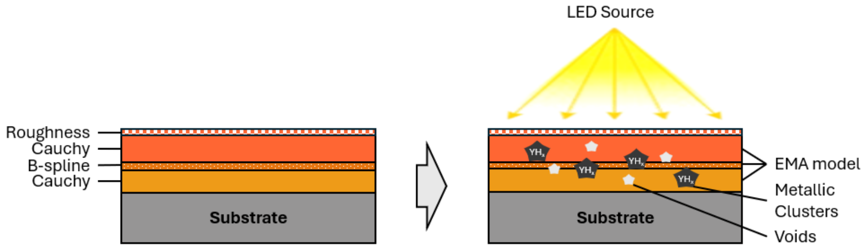

Figure 5.26: Schematic model of double-layer samples used in the CompleteEase software, illustrating the three layer (Cauchy and B-spline) used to model the sample, and with an EMA model containing metallic clusters during photo-darkening.

Sample		**Model**	**Parameters**	**Thickn. (nm)**	**Roughn. (nm)**	**MSE**
Single-layer						
0.8Pa 305nm		Cauchy	A = 1.766 B = 0.013	318.1	5.21	9.78
0.5Pa 240nm		B-spline	–	241.9	7.1	16.16
Double-layer						
Subs/0.5Pa/0.8Pa		–	–	522.0	8.1	7.68
–	0.8Pa 305nm	Cauchy	A = 1.787 B = 0.019	305.9	–	–
–	Boundary	B-spline	–	38.0	–	–
–	0.5Pa 240nm	Cauchy	A = 2.235 B = 0.082	178.1	–	–

Table 5.5: Transparent state model parameters and characteristics for single and double-layer samples, including thickness, roughness, and mean squared error (MSE) values. Models used include Cauchy and B-spline.

1.766 and 1.787. This aligns with our results from the single-layer samples in table 5.3. The 0.5Pa bottom layer is modelled with a relatively high A parameter of 2.235, indicating a high refractive index n. This refractive index is higher than the reported value of 1.881 for 0.5Pa thin films by Motero [29] and Beek [5]. Considering this parameter, it should be noted that the CompleteEASE software only provides parameters corresponding to an optimal fit and in no way measures the actual values.

After creating the models for the transparent state, the EMA model can be used to model the photo-darkened states. Since we cannot apply the EMA model to the whole sample, we must convert each layer into an EMA model separately. Just as we did for the single-layer samples, we created an EMA model with metallic clusters (YH_x) and voids since this approach results in the lowest MSE.

The resulting optical constants for the Cauchy and EMA models are shown in figure 5.27. As we already saw in the A-parameters, the refractive index of the 0.8Pa sample is lower than the 0.5Pa sample. While it is questionable whether the index is that high, we notice a higher refractive index for the 0.5Pa layer, which is expected with the lower oxygen ratio [8]. We see a sudden shift in refractive index for both samples after the first minutes of illumination. After this, the n decreases slightly during illumination for both layers. Following the bleaching of the sample, we model a significant decrease in n. This was also observed in the single-layer samples, and research by Beek [5]. Only in the 0.5Pa layer do we see a knot around λ = 1100nm, after which the n increases during illumination.

A clear difference can be seen for both layers' extinction coefficients k. Since we use a Cauchy layer combined with an Urbach tail in the model, the initial extinction coefficient value goes to zero with increased wavelength. During illumination, the extinction coefficient increases for both layers. We, however, see a more intense increase in the 0.5Pa layer. This is in line with our expectations since

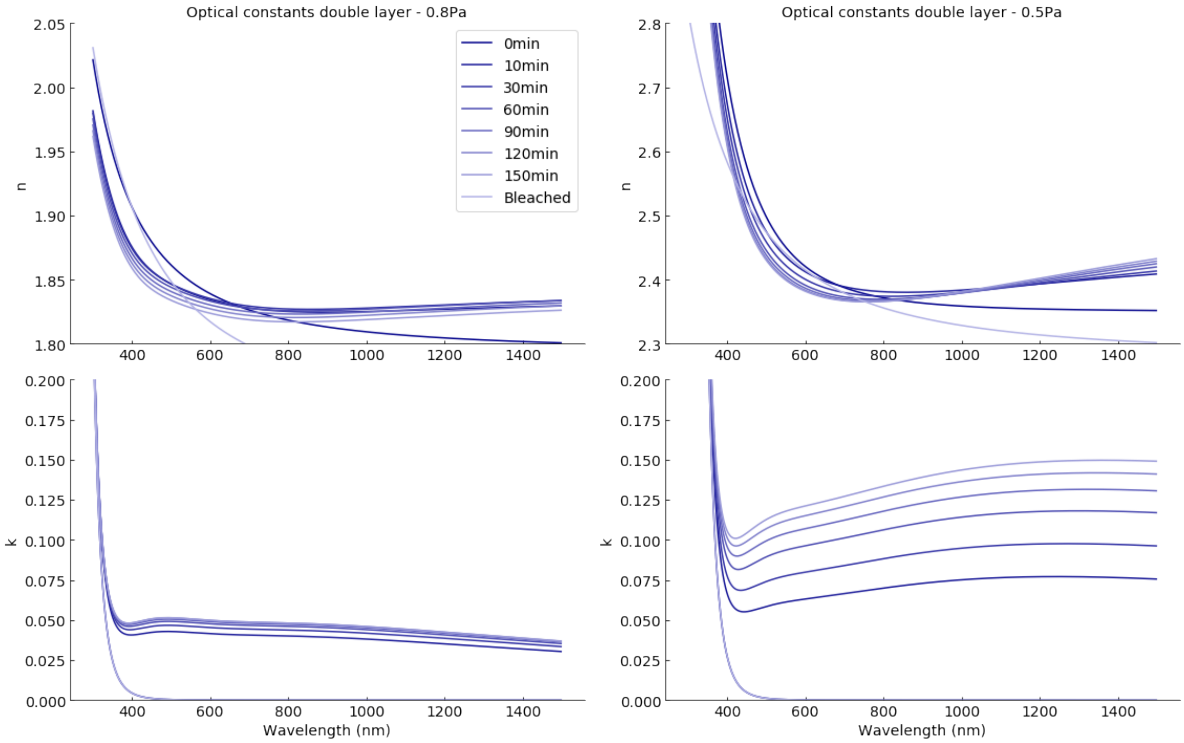

(a) Optical constants $n(\lambda)$ and $k(\lambda)$ for 0.8Pa single- layer in the double-layer sample

(b) Optical constants $n(\lambda)$ and $k(\lambda)$ for 0.5Pa single- layer in the double-layer sample

Figure 5.27: Optical constants ($n(\lambda)$ and $k(\lambda)$) for double-layer samples, measured at 0.8Pa and 0.5Pa deposition pressures, across multiple time intervals.

the extinction coefficient is directly related to the absorption, which is higher for 0.5Pa samples after illumination, hence the stronger photochromic contrast.

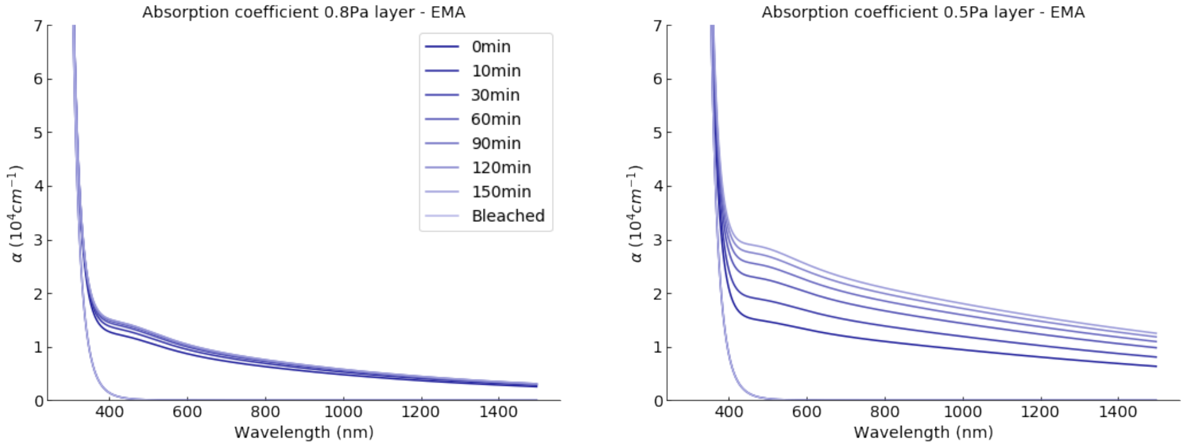

(a) Absorption coefficient $\alpha(\lambda)$ for the 0.8Pa layer in the double-layer sample.

(b) Absorption coefficient $\alpha(\lambda)$ for the 0.5Pa layer in the double-layer sample.

Figure 5.28: Absorption coefficients ($\alpha(\lambda)$) determined using the complex refractive index from figure 5.27 and formula 2.21 for double-layer samples consisting of 0.8Pa and 0.5Pa layers measured over time, calculated using the EMA model.

In figure 5.28, it is evident that the maximum absorption for the 0.8Pa layer is obtained faster, and stabilises after 10 minutes, compared to the 0.5Pa layer, which continues to increase within the time interval of 10–150 minutes. This increase is also reflected in the photochromic contrast, which continuos to increase after 150 minutes (see figure 5.11). These observations align with the metallic cluster model in figure 5.22a, where the metallic clusters of both pressures increase accordingly.

The behaviour of the k-value contributes to the absorption coefficient, which is obtained with formula 2.21. Additionally, for both layers, the absorption coefficient (figure 5.28) seems to converge to zero for longer wavelengths.

Since we have different EMA models for the three layers, we will calculate the metal cluster fraction as a weighted average of the three layers according to their modelled thickness. This is done using formula 5.6, where the sample's thickness (d_{sample}) is 522nm, and the 0.5Pa, boundary and 0.8Pa layers are 178, 38 and 306nm, respectively. The metallic cluster fraction for each layer is determined with the EMA model and also depicted in figure 5.29a.

$$f_m = f_{m,0.5layer} \cdot \frac{d_{0.5layer}}{d_{sample}} + f_{m,boundary} \cdot \frac{d_{boundary}}{d_{sample}} + f_{m,0.8layer} \cdot \frac{d_{0.8layer}}{d_{sample}} \tag{5.6}$$

In addition to the double-layer sample, we measured both 0.8Pa and 0.5Pa single-layer samples separately during illumination. We can compare the modelled difference in metallic cluster content using the EMA model. When comparing the single-layer samples to the samples in figure 5.22a, we observe an increase in metallic clusters for the 0.5Pa sample and a small decrease for the 0.8Pa sample. The exact difference in metallic cluster content can be found in appendix B.3.

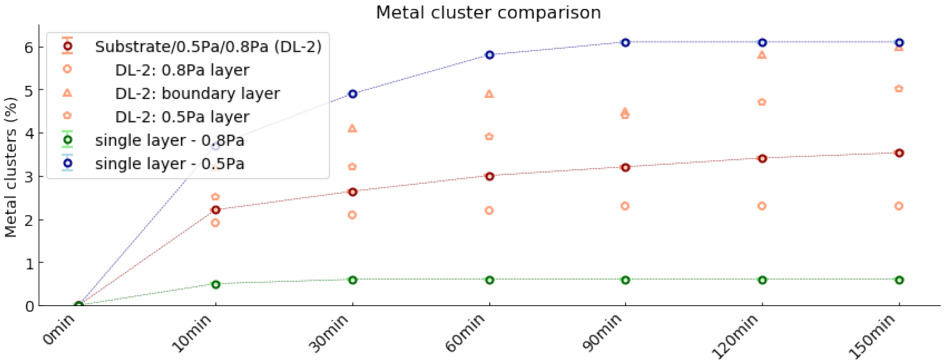

(a) Percentage of metal clusters determined using the EMA model for double-layer samples, as well as the single-layer samples deposited in the same batch, measured over time.

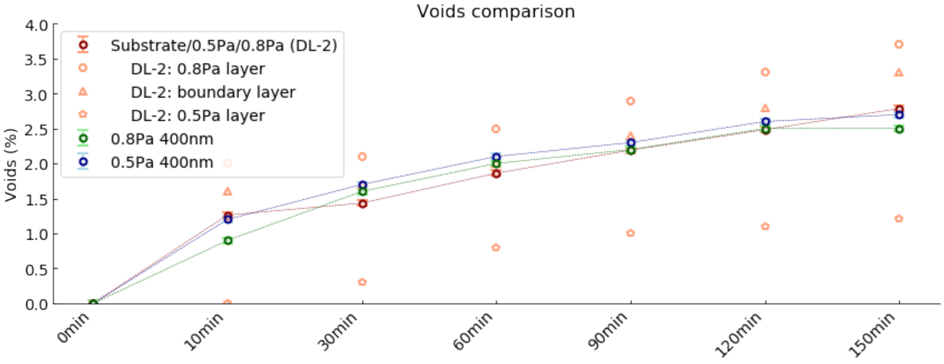

(b) Percentage of voids determined using the EMA model for double-layer samples, as well as both 0.5Pa and 0.8Pa 400nm samples discussed in section 5.2.2, measured over time.

Figure 5.29: Comparison of metal clusters and voids percentage determined using the EMA model for double-layer and single-layer samples, measured over 150 minutes with various deposition pressures.

As for the modelled voids in the sample, we apply the same method to obtain the total voids in the sample as we did for the metallic clusters. This results in a total void percentage between 1.3% and 2.8% during illumination, which is in line with all previous samples. When comparing the two layers within the double-layer model, we observe a significantly higher void percentage in the 0.8Pa top layer compared to the capped 0.5Pa bottom layer of sample DL-2. This difference could be expected with the higher porosity of the 0.8Pa layer, which could have more voids due to the not perfectly staking layer when the 0.8Pa sample is deposited.

The modelled 0.5Pa, boundary and 0.8Pa layers in the double-layer sample are also shown in figure 5.29a. The metallic cluster percentages are lower for the 0.5Pa layer and higher for the 0.8Pa layer compared to the single-layer samples produced in the same batch. The weighted average metallic cluster content for DL-2 starts at 2.2% after 10 minutes and increases to 3.5% after 150 minutes. This cluster content of the double-layer is right between the 0.8Pa and the 0.5Pa layer, which is to be expected since these layers both have a high contribution to the weighted average.

Using the formula 5.5, we are able to create a plot where the metallic cluster content is a function of the photochromic contrast. We created this plot for the double-layer and both separate single-layers. Just as in table 5.4, we calculated the C-values with both the absorption resulting from the optical and SE measurements, which can be found in table 5.6. The single-layer C-values resulting from both measurements are approximately in line with our findings in table 5.4. For the double-layer sample it is not possible to do optical measurements on each as deposited layer separately. However, by evaluating the C-values for both Cauchy single-layer models representing the 0.5Pa and 0.8Pa layers within DL-2, we can confirm that the resulting $4.16 \cdot 10^7 m^{-1}$ could be an approximate average of the 0.5Pa and 0.8Pa layers, with SE obtained C-values of $4.64 \cdot 10^7 m^{-1}$ and $3.87 \cdot 10^7 m^{-1}$, respectively. This also confirms the consistent cross-section of the metallic clusters within all samples.

Sample	**C-values Optical ($10^7 m^{-1}$)**	**C-values SE ($10^7 m^{-1}$)**
Single-layer		
0.5Pa 240nm	3.65	3.59
0.8Pa 305nm	3.95	3.06
Double-layer		
Subs/0.5Pa/0.8Pa (DL-2)	4.16	(-)
- 0.5Pa	(-)	4.64
- 0.8Pa	(-)	3.87

Table 5.6: Resulting C-values from formula 5.5 for the single-layer and double-layer samples in figure 5.30.

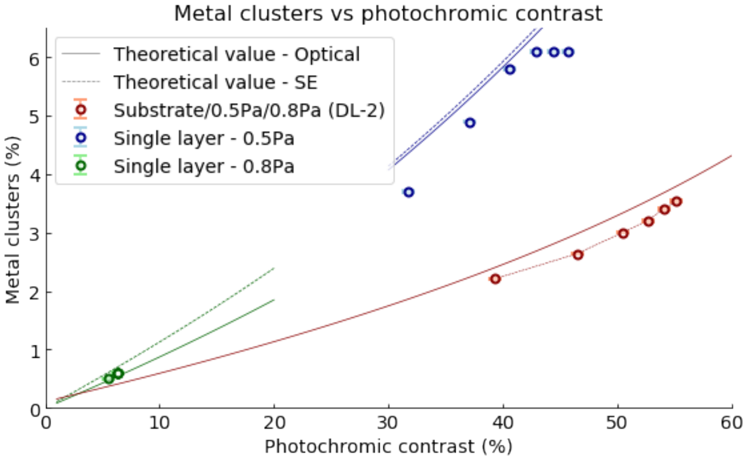

Figure 5.30: Metal clusters versus photochromic contrast for various samples, including double-layer samples (DL-2) and single-layer samples.

We can also clearly see the influence of the sample thickness in this model. With increasing thickness, we observe a flattening of the curve, meaning that a higher contrast is reached with the same metal cluster fraction, which is expected for thicker samples.

5.3. X-Ray Diffraction

The X-Ray Diffraction (XRD) pattern was measured from $2\theta = 20^\circ$ to 70° for three states of the 0.5Pa and 0.8Pa samples. Initially, the transparent sample was measured without having undergone any illumination cycles. After this, the sample was illuminated for 150 minutes before being measured again right after illumination when it was still in its photo-darkened state. Lastly, we let the sample bleach back to its transparent state for 20 hours, after which we performed a final measurement. Each measurement takes 32 minutes to complete, and starts at 20° and ends at 70°.

5.3.1. Single-layer XRD

In figure 5.31, the red line shows the measured XRD pattern for both 400nm samples. As explained in section 4.4.2, the measured data was analysed by Rietveld refinement to determine the characteristics of the material structure.

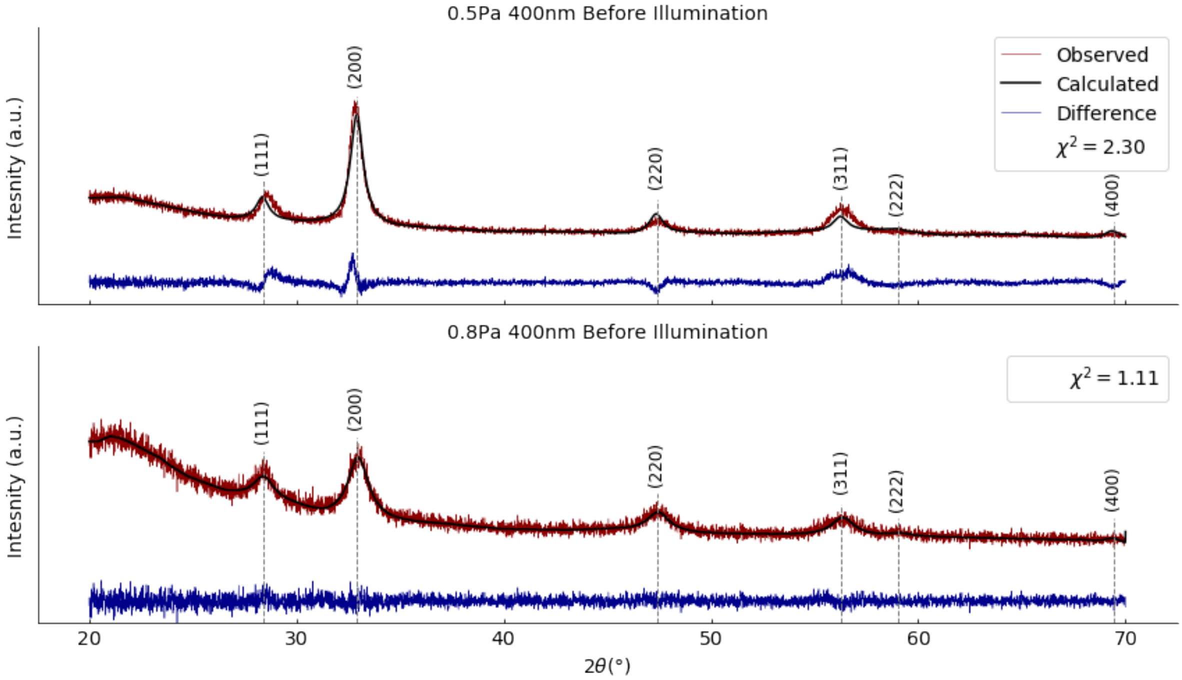

Figure 5.31: XRD measurements of 400nm samples before illumination, showing observed and calculated data along with the difference (blue) for samples deposited at 0.5Pa (top) and 0.8Pa (bottom). The corresponding χ^2 values are shown for each sample.

The XRD pattern displays several characteristic peaks associated with YOH lattice orientations. The most significant difference between the two samples is observed in the (200) peak, which is substantially higher for the 0.5Pa sample. This does not align with the findings of Chuan You et al. [52], who saw increased (200) peaks with increasing oxidation.

Sample	Transparent	150 min of Illumination	After Bleaching
0.5Pa 400nm	5.400 ± 0.001	5.372 ± 0.001	5.369 ± 0.001
0.8Pa 400nm	5.391 ± 0.002	5.388 ± 0.002	5.399 ± 0.002
0.8Pa 600nm	5.393 ± 0.002	5.390 ± 0.001	5.400 ± 0.001
0.8Pa 800nm	5.404 ± 0.001	5.402 ± 0.001	5.403 ± 0.001

Table 5.7: Measurements of various samples at different stages: transparent, after 150 minutes of illumination, and after bleaching. The values represent the measurements in Å along with their respective uncertainties.

Our refinement results indicate the presence of a fcc cubic (Fm-3m) crystal structure for all samples before, during and after photo-darkening. This aligns with multiple other articles that reported XRD measurements on YOH thin films [11, 50, 55, 21]. In previous research by Montero et al. [16], it is mentioned that the lattice constant of YH_2 increases from 5.20Å to 5.40Å when exposed to oxygen and transforms the YH_2 film to YOH. Thus, the incorporation of oxygen in the lattice shows an increasing effect on the lattice constant. This relation between deposition pressure and lattice constant was also researched by Colombi et al. [9], and is depicted in figure 2.8.

Our measurements indicate a value for the lattice constant similar to that reported in previous research, approximately 5.40Å. In all samples, a small decrease in lattice constant is observed after illumination. Comparing our results to the lattice constants of transparent YOH (5.40Å) and metallic YH_2 (5.20Å), a decreasing lattice constant could be expected for a phase shift to a darker state if anions are removed from the crystal lattice during photo-darkening[21, 27]. The difference between the 0.8Pa samples and the 0.5Pa sample, where the latter undergoes a higher decrease in lattice constant, can possibly be attributed to the higher photochromic contrast visible in the 0.5Pa sample. Additionally, the escape of hydrogen from the YOH crystal structure, reported by Moldarev et al. [26], could give an explanation for the decreasing lattice constant.

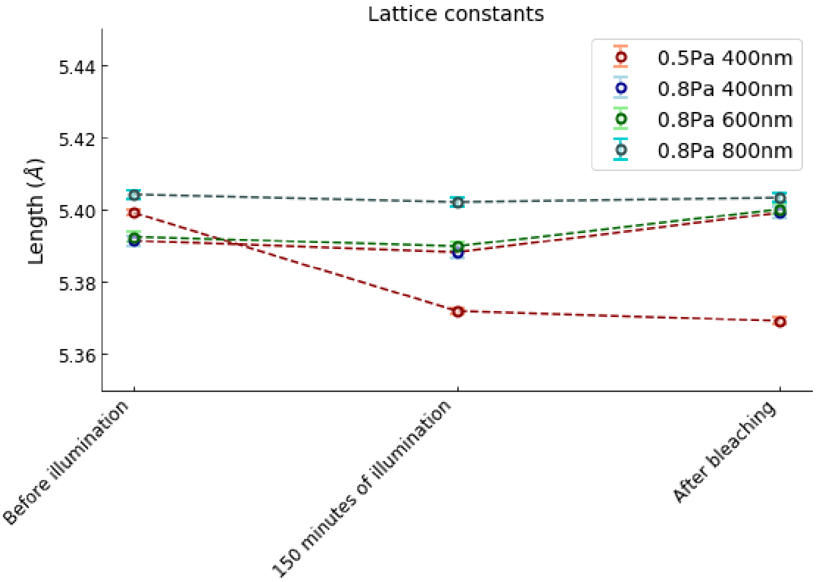

Figure 5.32: Lattice constants for samples before illumination, after 150 minutes of illumination, and after bleaching from table 5.7. The graph shows changes in lattice length (Å) for samples deposited at 0.5Pa and 0.8Pa with various thicknesses.

After bleaching, the lattice constant of the 0.5Pa sample does not increase back to the original length. As for the 0.8Pa samples, the lattice constants increase back to 5.40Å. Nonetheless, The decrease and increase in the 0.8Pa samples are so small that no accurate conclusions can be made.

5.3.2. Double-layer XRD

The XRD patterns for the double-layer samples in their transparent state are plotted in figure 5.33. The characteristic peaks, also detected for the single-layers in figure 5.31 for YOH, are visible in both patterns.

Compared to the single-layer samples, we see a difference in relative peak intensity between the (111) and (200) peaks. This difference was also detected in figure 5.31 and indicated a higher presence of one lattice orientation relative to the other.

The Rietveld refinement in our research is made with YH_2 data as a reference. This data tells the FullProf Software to have a certain ratio between orientation peaks, which prevents the Rietveld refinement from making an optimal fit since the (111) peak is underestimated in all models, increasing the models' MSE. Compared to the single-layer samples, the overall increase in MSE could also imply that the stacking of the second layer on the first layer will result in a less constant crystal lattice parameter. Apart from the minor difference observed in intensity of the (111) peak, the XRD pattern for the DL-2 sample closely resembles that of the 0.8Pa samples discussed in section 5.3.1.

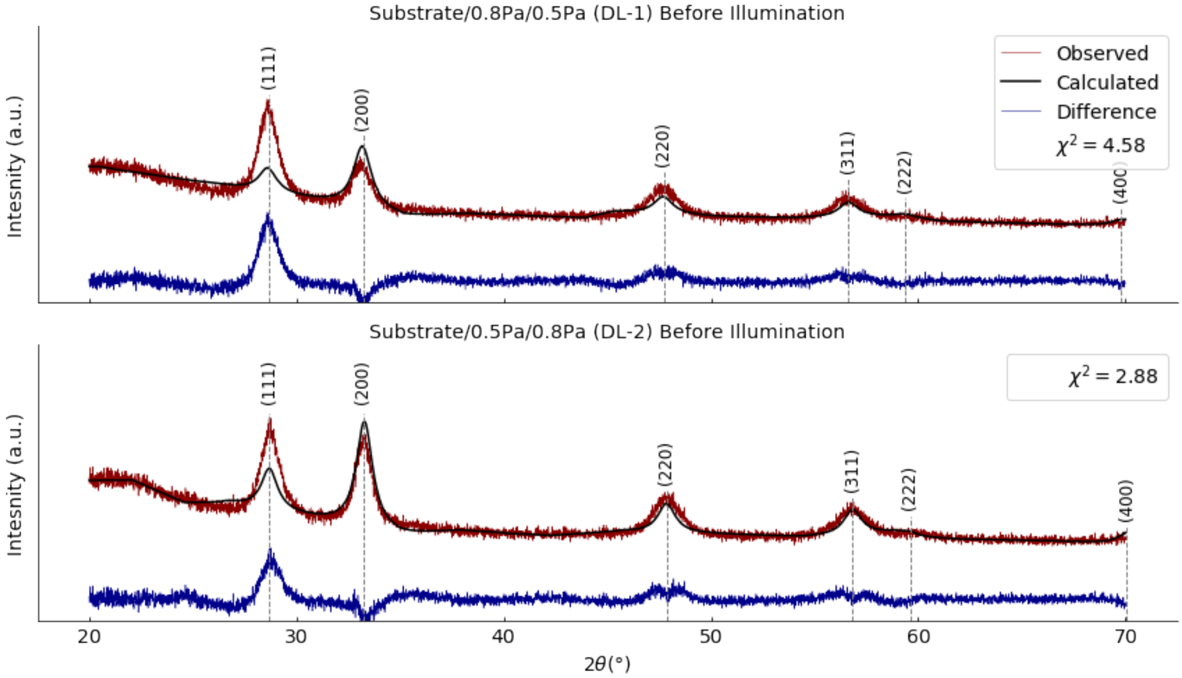

Figure 5.33: RD measurements of double-layer samples before illumination, showing observed and calculated data with the difference (blue) for samples deposited at 0.8Pa/0.5Pa (DL-1, top) and 0.5Pa/0.8Pa (DL-2, bottom). The corresponding χ^2 values are shown for each sample.

When comparing the double-layer samples, the MSE (χ^2) for the DL-1 sample is significantly higher than that for the DL-2 sample. This difference is not entirely unexpected since the sample looked visually different and inhomogeneous.

Since we also prepared single-layers of every double-layer deposition, the individual top layers of both samples were also analysed using XRD. The resulting lattice constants are presented in table 5.8 and follow the expected trend where the more oxidized layer (i.e. 0.8Pa) has the highest lattice constant. Measurements of the double-layer sample, are also shown in the table. The transparent state shows a lattice constant of 5.373 ± 0.004Å and 5.354 ± 0.002Å for DL-1 and DL-2, respectively.

The DL-1 sample shows an increased lattice constant for the top 0.5Pa layer compared to its respective single-layer. This increase may be attributed to a higher degree of oxidation, likely resulting from the more porous structure since it was deposited on a 0.8Pa YOH thin film instead of a bare f-Si substrate. The DL-2 sample, on the other hand, shows a small decrease in lattice constant.

Sample	**Transparent**	**150 min of Illumination**	**After Bleaching**
Substrate/0.8Pa/0.5Pa (DL-1)	5.373 ± 0.004	5.383 ± 0.004	5.382 ± 0.004
Single-layer - 0.5Pa	5.347 ± 0.001	n.a.	n.a.
Substrate/0.5Pa/0.8Pa (DL-2)	5.354 ± 0.002	5.356 ± 0.002	5.358 ± 0.002
Single-layer - 0.8Pa	5.365 ± 0.003	n.a.	n.a.

Table 5.8: Measurements of various samples at different stages: initial, after 150 minutes of illumination, and after bleaching. The values represent the measurements in Å along with their respective uncertainties.

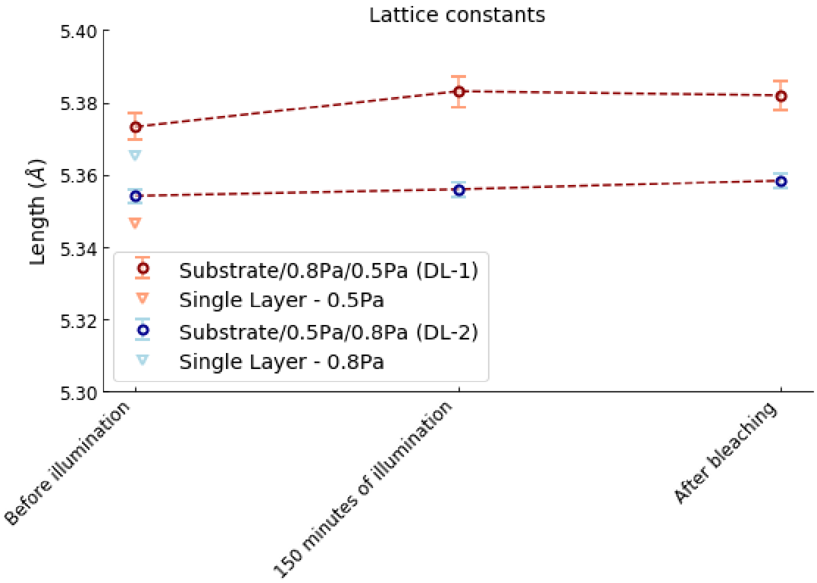

Figure 5.34: Lattice constants for samples before illumination, after 150 minutes of illumination, and after bleaching from table 5.8. The graph shows changes in lattice length (Å) for both double-layer samples and the corresponding single-layers.

After illumination, the DL-1 sample shows a slight increase, while the DL-2 sample remains almost constant. The same goes for the bleaching process, where the lattice seems almost constant.

In general, we see an evident influence of the double-layer method on the lattice constant of the top layer. This influence is caused by the bottom layer, which serves as a base for the top layer, and may influence its porosity and thus the oxidation grade. During and after illumination, the lattice constants do not change significantly, something also observed for the 0.8Pa single-layer samples in section 5.3.1.

5.4. Doppler Broadening Positron Annihilation Spectroscopy

The Doppler Broadening Positron Annihilation Spectroscopy (DB-PAS) measurements were conducted over a variable energy range from 0.1 to 22 keV. Using the results of DB-PAS measurements we hope to gain a better understanding of the microscopic changes within the thin film which may play a role in the memory effect. The samples were measured before and after three illumination cycles. Due to minor problems with the setup, we made some changes in-between the single- and double-layer measurements. The detector was initially placed behind the sample. However, due to the inconsistency of the positron beam and small samples, some of the positrons missed the sample. They annihilated within the vacuum chambers' wall, significantly influencing the measurement data since this wall was closer to the detector. This was solved by moving the detector to the side, increasing the distance to the sample - and decreasing the count rate significantly. This change in the count rate led to a measurement time of almost three days per sample for a full depth profile.

Due to the improved accuracy, we have chosen to focus solely on the measurements conducted after the setup modification. Consequently, this analysis will concentrate on the results for the double-layer samples, as the measurements for the single-layer samples are considered unreliable.

5.4.1. Double-layer DB-PAS

Previous work by Wu et al. [50, 51] on DB-PAS measurements of YOH photochromic samples focused on single-layer thin films. Measurements were performed on on a wide variety of samples deposited at different pressures. Most notably, the S- and W-parameters for Y_2O_3 and $YH_{2-\delta}$ were obtained, showing the consequences of oxygen incorporation into the crystal lattice. A decrease in the S-parameter and increase in the W-parameter was observed when comparing $YH_{2-\delta}$ to Y_2O_3. This noticeable shift, which is also reported in the research by Plokker et al. [38], can be attributed to the strongly localized upper valence electrons between the Y^{3+} and O^{2-} bonds. Given the above, we will expect a decreasing S-parameter with higher deposition pressures.

Measurements conducted by Wu et al. [51] investigated the illumination and bleaching effects on 0.5Pa thin films. Before illumination the DB-PAS measurements yielded a S-parameter of 0.526 and a W-parameter of 0.048. After three cycles of 2.5 hours of illumination and 20 hours of bleaching, these parameters changed to 0.541 and 0.046, respectively. This noticeable increase in the S-parameter indicates the annihilation of lower-momentum electrons, which could be attributed to the formation of vacancies within the crystal lattice. Both the metallic domains (2.5.1) and Anderson-Mott (2.5.2) mechanism underline the importance of H^- mobility for the photochromic effect, which could play a role in the permanent creation of the vacancies [50]. Additionally, the effusion of weakly bound hydrogen could also induce a permanent increase in S-parameter. A similar observation was reported by Colombi et al. [9], who conducted DB-PAS measurements on 0.4, 0.5, and 0.6Pa thin films before and after illumination. In addition to the increase in the S-parameter following illumination, the samples exhibited the previously mentioned trend, where the more oxidized sample (0.6Pa) had the lowest S-parameter.

	S-parameter		**W-parameter**	
Sample	**0.5Pa layer**	**0.8Pa layer**	**0.5Pa layer**	**0.8Pa layer**
Substr./0.8Pa/0.5Pa (DL-1)	0.531 ± 0.003	0.529 ± 0.002	0.047± 0.001	0.055 ± 0.001
Substr./0.5Pa/0.8Pa (DL-2)	0.523 ± 0.005	0.494 ± 0.002	0.056 ± 0.002	0.067 ± 0.001

Table 5.9: S-parameters and W-parameters for double-layer samples before illumination.

The implantation profiles for the Variable Energy Positron (VEP) measurements of our double layers are shown in figure 5.35. With the associated average bulk parameter for each layer before and after illumination given in table 5.9 and 5.10, respectively.

When comparing the obtained parameters for each layer to the implantation profile, it is evident that the parameters do not always directly correspond to the profile. For instance, an S-parameter of 0.523 was modelled for the 0.5Pa layer in the DL-2 sample, yet the implantation profile does not show any mea-

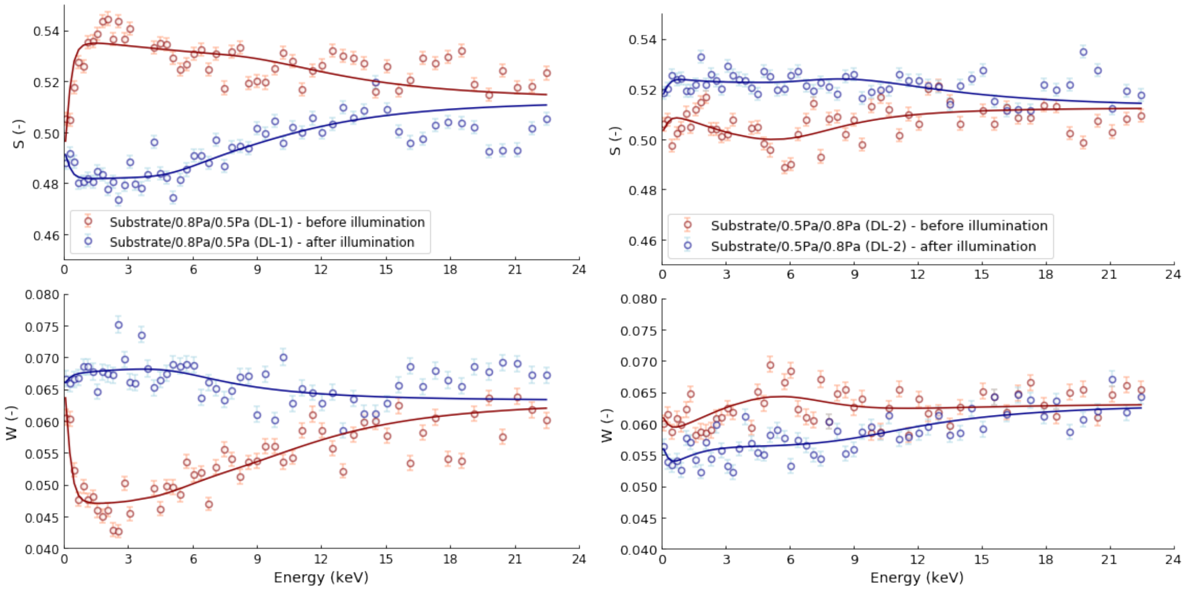

(a) S- and W-parameters for the Substrate/0.8Pa/0.5Pa (DL-1) sample, measured before illumination and after illumination.

(b) S- and W-parameters for the Substrate/0.5Pa/0.8Pa (DL-2) sample, measured before illumination and after illumination.

Figure 5.35: S- and W-parameters for double-layer samples (DL-1 and DL-2), measured before illumination and after three illumination cycles of 150 minutes each, followed by 1200 minutes of bleaching.

sured or modelled data near this value before illumination. This discrepancy arises from the positrons' ”drunkard's walk” within the material, which results in their annihilation at different depths in different layers, causing multiple layers to contribute to the observed parameter at the same implantation energy. The fraction of each layer contributing to the S-parameter is modelled using the VEPFIT software, and these fractional contributions for the ’before illumination’ models are presented in figure 5.36. The ’after illumination’ fractional contribution graphs can be found in appendix C.1.

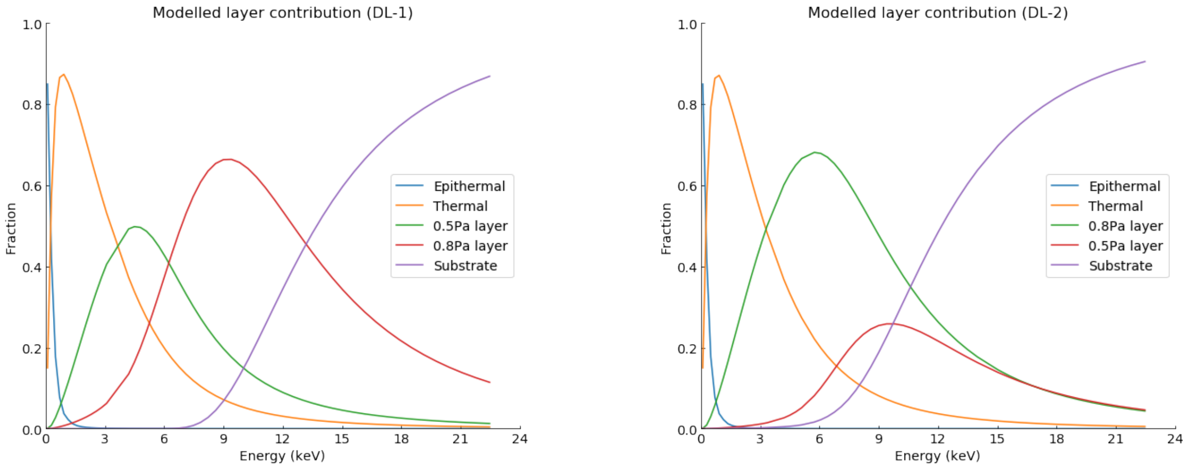

(a) Fraction distribution for DL-1 sample before illumination

(b) Fraction distribution for DL-2 sample before illumination

Figure 5.36: Fraction distribution of positron annihilations in each layer contributing to S-parameter

Before illumination both samples show a high S-parameter for energy values around 2keV, indicating a high level of vacancies near the surface layer. When analysing the parameters of both samples, a higher S-parameter is modelled for the 0.5Pa layer compared to the 0.8Pa layer. This is in line with previous findings and supported by the higher oxidation grade of 0.8Pa sample, thus creating more Y^{3+} and O^{2-} bonds with localized electrons, decreasing the S-parameter.

The S-parameter of the 0.5Pa layers in both samples are 0.531 $\pm$ 0.003 and 0.523 $\pm$ 0.005 for the DL-1 and DL-2 samples, respectively. This is approximately in line with the 0.526 S-parameter obtained by Wu et al. [51]. We are confident that the 0.5Pa layer in the DL-2 sample exhibits the same properties as previous researched thin films. The 0.5Pa layer in the DL-1 sample, however, does not exhibit a direct resemblance in either the measured or visible characteristics.

As for the 0.8Pa layers, no comparable measurements where found in previous research. The S-parameter of both different samples also don't give the same value. The DL-1 sample has a S-parameter of 0.529 ± 0.002, whereas the DL-2 samples is 0.494 ± 0.002. This difference in parameters could be attributed to variations in oxidation levels. However, it remains unclear whether the 0.8Pa layer in the DL-1 sample is insufficiently oxidized or if the DL-2 sample has a higher oxidation grade. Depositing a layer on top of another, as is the case for the 0.8Pa layer in DL-2, may result in a more porous thin film due to the impact of the layer on which it is deposited. Such a porous thin film could exhibit higher oxidation, leading to a reduction in the S-parameter. However, if this mechanism caused the observed difference in the S-parameter, a similar effect would be expected in the 0.5Pa top layer in DL-1, which is not the case.

	S-parameter		**W-parameter**	
Sample	**0.5Pa layer**	**0.8Pa layer**	**0.5Pa layer**	**0.8Pa layer**
Substr./0.8Pa/0.5Pa (DL-1)	0.482 ± 0.001	0.502 ± 0.002	0.068 ± 0.001	0.064 ± 0.001
Substr./0.5Pa/0.8Pa (DL-1)	0.528 ± 0.002	0.523 ± 0.001	0.058 ± 0.001	0.057 ± 0.001

Table 5.10: S-parameters and W-parameters for double-layer samples after three illumination cycles.

The VEP measurements performed after three illumination cycles are shown by the blue line in figure 5.35. For the DL-2 sample we see an overall increase in S-parameter for both layers. This was also observed in previous research by Wu et al. [51], and could point to the creation of vacancies attributed to H^{-} mobility in the thin film. As for the W-parameter, which tells us more about the high momentum electrons, a steep decrease was modelled for the 0.8Pa layer, from 0.067 ± 0.001 before illumination to 0.057 ± 0.001 after illumination. This decrease suggests a reduction in high-momentum electrons, potentially associated with Y^{3+} and O^{2-} bonds. The 0.5Pa layer exhibits a slight increase in the S-parameter but remains relatively constant.

The DL-1 sample, on the other hand seems to have a clear decrease in the S-parameter. This decrease is unexpected since we would expect the formation of vacancies within the thin film. However, looking at other measurement methods performed on this sample, we already see a total different behaviour in the optical properties during the transparent and photo-darkened state. These include lower-than-expected transmission, photochromic contrast, and reflection. The modelled decrease in the S-parameter, and consequently the increase in high-momentum electrons, suggests a higher oxidation level for both layers. This higher oxidation could also explain the observed decrease in photochromic contrast after each illumination cycle, as the O:H ratio plays a critical role in the photo-darkening process.

Figure 5.37 illustrates the modelled S- and W-parameters for each layer, compared to previous research on the oxidation of YOH [38]. In general, all double-layer samples exhibit a lower-than-expected S-parameter and a higher-than-expected W-parameter compared to the measured trend of Y-based thin films shown in figure 5.37, indicating higher oxidation levels. Among our modelled layers, only the 0.8Pa layer in the DL-2 sample demonstrates the expected behaviour with increasing and decreasing S- and W-parameters after illumination, respectively. The deviation in the other layers, particularly in the DL-1 sample, may be attributed to inhomogeneities or higher porosity, as discussed in previous sections. Such characteristics could lead to variations in hydrogen mobility and bonding, ultimately influencing the measured S- and W-parameters.

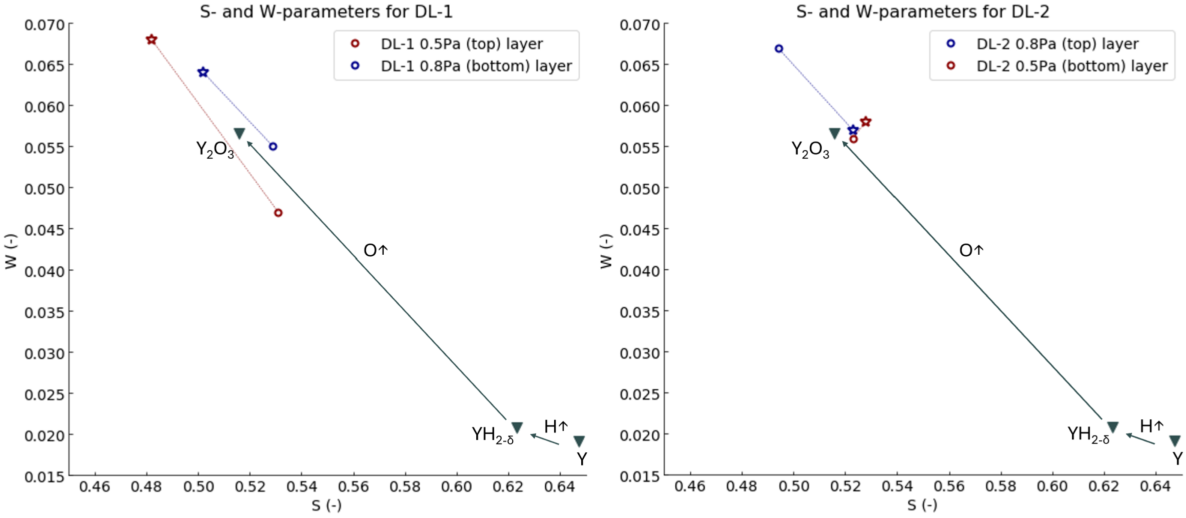

(a) S- and W-parameters for the layers in the DL-1 sample, measured before (o) and after illumination (⋆).

(b) S- and W-parameters for the layers in the DL-2 sample, measured before (o) and after illumination (⋆).

Figure 5.37: S- and W-parameters for the different layers within the double-layer samples, showing measurements before and after illumination for Substrate/0.8Pa/0.5Pa (DL-1) and Substrate/0.5Pa/0.8Pa (DL-2). Including the S- and W-parameters of Y-based thin films measured by Plokker et al. [38]

6

Discussion

Optical Measurements

For single-layer samples deposited at pressures of 0.5Pa and 0.8Pa, photochromic contrasts of 53.0 ± 0.4% and 11.4 ± 0.4% were observed for the 400nm thin films, respectively. This inverse relationship between deposition pressure and photochromic contrast is consistent with prior studies [31, 7, 9, 52]. Additionally, the bleaching time constant also exhibited a pressure-dependent trend. The measured bleaching time constants for the 0.5Pa and 0.8Pa 400nm samples are 5.1 and 0.6 hours, respectively. These observations align with earlier findings by Baba et al. [3], Beek [5] and Colombi et al. [9]. While our results show that film thickness influences photochromic contrast, the bleaching time constant remained unaffected by increased thickness.

The 800nm samples deposited at 0.8Pa looks visible different from the thinner samples, which is possibly caused by inhomogeneity of the sample. In his research [31] Montero-Amenedo suggest that thicker films deposited at higher pressures are more porous, exhibit greater phase diversity, and experience enhanced inhomogeneity. Additionally, Banerjee et al. [4] propose that uneven pore distribution in thicker films may facilitate the formation of hydride-rich and hydride-poor regions, potentially contributing to the observed inhomogeneity. However, they note that the influence of film thickness remains uncertain and requires further investigation to confirm its validity.

For 0.8Pa samples, the photochromic contrast decreased over repeated illumination cycles. This degrading of the photochromic thin film has not yet been mentioned in other reports. Moldarev et al. [26] observed that weakly bound hydrogen atoms effuse from the YOH thin film during the the first photo-darkening cycle. While the exact explanation for the decreasing photochromic contrast remains unclear, a correlation could be drawn between the higher porosity and its probable effect on hydrogen effusion in the 0.8Pa samples. The higher porosity films could have a higher level of weakly bound hydrogen, which does not all leave the thin film in the first photo-darkening cycle. Subsequent hydrogen effusion during repeated cycles raises the O:H ratio, which could degrade photochromic contrast due to hydrogen's critical role in photo-darkening. However, further research will be necessary to make any definite conclusion.

In double-layers, the DL-1 sample (T_0 = 31.6 ± 0.2%) demonstrated significantly lower transmission in the transparent state compared to the DL-2 sample (T_0 = 79.5 ± 0.2%). Using Formula 5.2, the DL-2 sample's transmission during three cycles closely matched the theoretical prediction, indicating that both layers may have retained their intrinsic photochromic properties. The photochromic contrast for DL-2 (55.2 ± 0.4%) deviated only slightly from the expected $\approx$ 52%, possibly due to higher oxidation in the 0.8Pa top layer, increasing T_0 compared to the theoretical T_0 of $\approx$73%. In contrast, the DL-1 sample's transmission did not align with the theoretical curve and exhibited a reduced photochromic contrast of 29.7 ± 0.4%.

Reflection measurements for the DL-1 sample revealed a low reflection of (2.7± 0.2%). The deviating optical properties of this sample influence the calculated bandgap. This discrepancy may result from limitations in the measurement setup, which detects reflection and transmission at a single point, assuming that all transmitted and reflected light travels in a straight line from the source to the detectors. Given the observed inhomogeneity of the thin film (figure 3.2), it is possible that the surface layer exhibits increased roughness, leading to enhanced light scattering. This scattering effect could reduce the measured reflection and transmission values. Another possibility involves a lower oxidation grade in the top layer, reducing reflection and transmission while enhancing absorption. However, a lower oxidation grade would typically be accompanied by an increase in photochromic contrast and bleaching time constant, which was not observed in this case, making this explanation less plausible.

The double-layer samples' bleaching time constants exceeded those of their respective bottom layer, measured as separate single-layers. Since these bottom layers seem to dominate the double-layer samples' optical characteristics, we infer that the capping of the bottom layer impacts the bleaching time constant negatively. The capping of these layers likely influences the hydrogen movement in the sample, but more research is required to draw any definite conclusions.

Overall, the DL-1 sample shows clear signs of the presence of the 0.8Pa bottom layer and its characteristic effects, such as the degradation of the photochromic contrast. The 0.5Pa top layer seems to be affected by the higher porosity of the bottom layer and may have an increased porosity and oxidation level, also causing the inhomogeneity. The DL-2 sample shows perfect stacking of the two layers, and in contrast to the DL-1 sample, it has the least porous layer at the bottom. This probably has had minimal effect on the second layer.

Spectroscopic Ellipsometry

For single-layer samples in the transparent state, spectroscopic ellipsometry analysis was performed using simple one-layer models unless more complex fits were warranted, given their decrease in MSE. The Cauchy, GenOsc, and B-spline models were applied (see table 5.3). Ideally, the Cauchy model would suffice for transparent thin films; however, deviations in the 0.5Pa layer prevented a successful fit. This contrasts with earlier studies by Montero [29] and Beek [5], where Cauchy models were applied effectively. Since our thin films show characteristics of a lower O:H ratio, such as the increased photochromic contrast and bleaching time, it is probable that samples with a lower oxidation grade are harder to fit with a Cauchy model. In the photo-darkened state, the effective medium approximation (EMA) model accounted for contributions from voids and YH_x. This model was previously identified as a good fit model for describing the photo-darkened state [5].

In the single-layer samples deposited at pressures of 0.5Pa and 0.8Pa, metallic cluster contents of 4.9% and 1.1%, were observed for the 400nm thin films after 150 minutes of illumination. The 0.5Pa sample is approximately consistent with the 6% modelled fraction in research done by Montero et al. [30]. Compared to Beek's model [5] (2.4% metal cluster fraction), we have a two times higher metallic cluster content, which is significant. Although, it should be noted that our 0.5Pa sample also shows a higher photochromic contrast of 53.0 $\pm$ 0.4% compared to 34%.

A direct correlation is laid between the absorption coefficient, transmission and the modelled metallic clusters, confirming the usage of formula's 5.4 and 5.5. The derived C-values, associated with the metallic cluster cross-section, ranged between $3.5 \cdot 10^7\,\mathrm{m}^{-1}$ and $4.5 \cdot 10^7\,\mathrm{m}^{-1}$, except for the inhomogeneous 800nm sample, which showed C-values of $5.58 \cdot 10^7$ and $2.12 \cdot 10^7\,\mathrm{m}^{-1}$ for the optical and SE obtained absorption coefficients, respectively. No direct correlation was observed between deposition pressure and metallic cluster cross-section.

No SE data could be extracted from the DL-1 sample due to its low reflection, limiting the detector in retrieving the Ψ and Δ data. If the low detected reflection is caused by the higher absorption of the thin film and not by scattering, further research in the same thin film would need a SE setup with a higher maximum light source intensity. For the DL-2 sample, a three-layer model comprising the two deposited layers and an intermediate boundary layer provided the best fit. While Cauchy models effectively described the deposited layers, a B-spline model was required for the boundary region. The ability to use the Cauchy model for the 0.5Pa layer is noteworthy, since all single 0.5Pa layers produced in this research could only be modelled using the B-spline approach. The model's thickness suggests that part of the 0.5Pa layer may be included within the boundary region, potentially indicating that the top of the 0.5Pa layer is best modelled with the B-spline, which prevents the single-layer models from a low MSE Cauchy fit. However, it did not result in a usable fit when trying to model 0.5Pa single-layer with both a B-spline and Cauchy layer. This would indicate that the used B-spline layer is a direct result of the double-layer deposition. The modelled boundary layer may be attributed to the 0.8Pa top layer. As observed in other models, the surface of deposited thin films often shows a degree of roughness. This roughness can affect the uniformity of the layer deposited on top, creating a small disordered region responsible for the B-spline modelled boundary region.

The absorption coefficient for the 0.5Pa layer within DL-2 (figure 5.28) continued increasing after 150 minutes, consistent with the photochromic contrast of the single-layer 0.5Pa sample, which also still increases after 150 minutes. In contrast, the 0.8Pa layer reached stable absorption values within 10 minutes, consistent with its higher oxidation levels and faster photo-darkening [9].

The metallic cluster content in the double-layer sample, derived as a weighted average of the three modelled layers, falls between the values observed for single-layer samples. Individual layer analysis showed higher metallic cluster content in the 0.8Pa top layer and lower content in the 0.5Pa bottom layer, potentially due to hydrogen transport across layers or model-fitting limitations. Further investigation is required to confirm these findings.

The obtained C-values for the double-layer sample are also in approximately the same range we saw for the single-layer samples. The optical measurement's C-value ($4.16 \cdot 10^7 m^{-1}$), which considers the whole thin film, is right in the middle of the SE composed C-values for both separate layers ($3.87 \cdot 10^7 m^{-1}$ - $4.64 \cdot 10^7 m^{-1}$), which would also be expected. Again, the single- and double-layer C-values do not show a correlation with the deposition pressure.

X-Ray Diffraction

XRD patterns for the single-layers revealed no clear correlation between oxygen content and lattice constants. Both the 0.5Pa and 0.8Pa samples exhibited lattice constants of approximately $\approx$5.40Å in the transparent state, equal to previous obtained values [11, 50, 55, 21]. Colombi et al. [9] reported a similar lattice constant of 5.395 $\pm$ 0.002Å for the 0.5Pa sample but observed a decreasing lattice constant with increasing oxygen ratios for pressures above 0.5Pa, a trend that was not observed in this study. Upon illumination, the 0.5Pa sample decreased to 5.372 $\pm$ 0.001Å, which remained almost constant after bleaching. This lower lattice constant for the 0.5Pa sample sounds reasonable since it has a lower oxygen content than the 0.8Pa samples. If there is a decrease in the lattice constant, this could indicate the effusion of hydrogen to the surroundings, which would have a decreasing effect on the lattice constant. However, since the 0.8Pa sample did not exhibit similar behaviour, it is more likely that the transparent state lattice constant of the 0.5Pa sample was actually lower than obtained from our measurement. An apparent reason for this difference in expected and measured value is hard to find but could be caused by a higher oxidised region in the sample, which we measured by coincidence.

Rietveld refinement for double-layer samples yielded higher Mean Squared Error (MSE) values compared to single-layers. Some X-rays will travel further into the thin film, reaching the bottom layer, which will contribute slightly to the measured pattern. Since the measurement now shows the contribution of two layers with different lattice constants, making a conclusive fit will be more challenging. Additionally, during the Rietveld refinement, YH_2 powder data was used as a reference. The atomic structure of YH_2 includes hydrogen ions occupying tetrahedral sites, which does not apply to YO_xH_{3-2x}. Consequently, YO_xH_{3-2x} could exhibits different peak intensities. Since this is relevant for all samples analysed in this study, it does not fully account for the increased MSE observed in the double-layer samples.

We see a significant increase of 0.026 $\pm$ 0.005Å in lattice constants when comparing the DL-1 sample with the single-layer 0.5Pa sample. We expect the top 0.5Pa layer of the double-layer sample to have the highest contribution to the measurement and not to see a big difference between both lattice constants. The higher lattice constant for DL-1 would support the statement that the top layer is highly oxidised. A similar increase is not visible for the DL-2 sample, where the 0.8Pa single-layer lattice constant is slightly higher than that of the DL-2 sample, which is not a conclusive difference and could be caused by the contribution of the bottom 0.5Pa layer to the measurement. We also do not see a significant change in lattice constants for the double-layer samples during illumination and bleaching.

Doppler Broadening Positron Annihilation Spectroscopy

During the Doppler Broadening Positron Annihilation Spectroscopy (DB-PAS) measurements on the single-layer samples in this study, the S- and W-parameters exhibited inconsistencies across repeated measurements of the same sample, making direct comparisons before and after illumination challenging. During the measurement, positrons are guided by a magnetic field, which directs them toward the target. Slight deviations from the centre in the positron paths between each magnetic coil result in a Lorentz force that adjusts the positron's trajectory, forcing it to the centre. These deviations also occur when the positrons arrive at the sample, which is placed at the centre, causing the positrons with a high deviation to miss the target entirely. Precisely directing the positron beam to the centre is challenging, as the beam can have a full-width at half-maximum (FWHM) of up to 8mm, compared to the 10mm sample size. In the VEP measurements, different implantation energies resulted in varying deviations from the centre. Consequently, some implantation energies result in different count rates than others, especially when the magnetic field induced by the coils was not optimized for that specific energy. To account for this, the positron beam was tuned by adjusting the current through the coils for each implantation energy separately, optimizing the magnetic field to achieve a more accurate positron beam at the target. However, not at all energies the positron beam could be successfully tuned, leading to lower count rates for specific energies. Additionally, the $^{22}\mathrm{Na}$ source used for these measurements was relatively old, resulting in lower activity and a low count rate. To improve the count rate, the detector was initially placed directly behind the target, as shown in figure 6.1a, resulting in a four times increase in the count rate. However, this setup introduced new challenges: positrons missing the target annihilated in the metal wall, affecting the S- and W-parameters. Additionally, the close proximity of the metal wall to the detector further influenced the count rate, as positron annihilations in the metal wall had a higher probability of being detected, rendering the data unreliable. To address these issues, the detector was moved back to the side, and the distance between the metal wall and the target was increased, reducing the interference from positrons annihilating in the wall significantly (see figure 6.1b). While these adjustments improved data reliability, they also increased the measurement time, limiting the number of possible measurements within the remaining duration of this thesis.

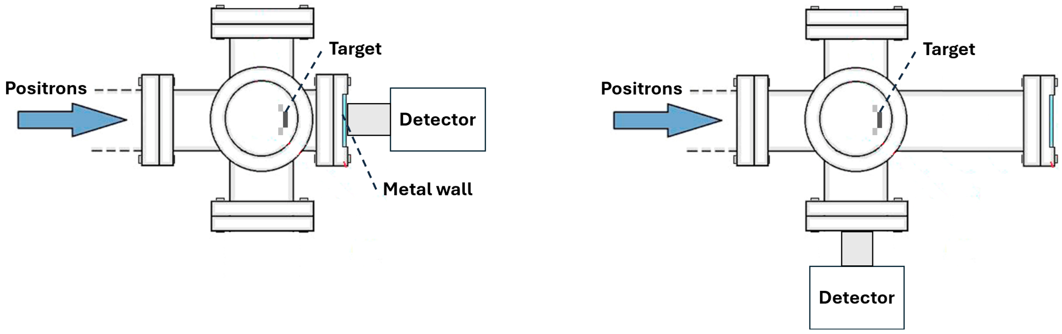

(a) DB-PAS setup with high count rate, but interference of positrons annihilating in the metal wall.

(b) DB-PAS setup with low count rate, but no significant interference from positrons missing the target.

Figure 6.1: Schematic top view setup of the two DB-PAS setups used.

The DB-PAS measurements we performed on double-layer samples resulted in the expected relation between the 0.5Pa and 0.8Pa layers before illumination, with the 0.5Pa layer having the higher S-parameter within each sample. In the DL-2 sample, a clear distinction is observed between the two layers, with the 0.5Pa layer modelled with an S-parameter of 0.523 ± 0.005, which is consistent with previous findings around 0.526 [51], while the 0.8Pa layer exhibits a significantly lower S-parameter of 0.494 ± 0.002. This trend is not observed in the DL-1 sample, where the modelled S-parameter for the 0.8Pa layer (0.529 ± 0.002) is only marginally lower and remains within the error margin of the 0.5Pa layer (0.531 ± 0.003). An apparent reason for the difference in the 0.8Pa layers is not obtained with the measuring method, but it could be caused by a lower oxidation grade in the 0.8Pa bottom layer since a second layer caps it off after 10 days of oxidation. If this were the case, a similar effect would be expected for the bottom 0.5Pa layer in the DL-2 sample. However, this behaviour was not observed. Alternatively, since the deposition of a 0.8Pa layer on top of a 0.5Pa layer could result in a higher porosity, the lower S-parameter for the top 0.8Pa layer in DL-2 could also be caused by a higher oxidation grade. A combination of both explanations cannot be ruled out. Additionally, the 0.5Pa top layer in the DL-1 sample has an S-parameter comparable to that found in previous research, even though the layer does not share any of the same characteristics. This S-parameter may also result from an increased number of vacancies in the presumably more oxidized 0.5Pa top layer.

Regarding the modelled fraction distribution, for both samples, the 0.8Pa layer has the highest contribution to the measured parameters. This could be attributed to the increased thickness of this layer, since a greater thickness means more positrons annihilate in this layer during their 'drunkard's walk'.

After illumination, a steep increase in the S-parameter is modelled for the top 0.8Pa layer in the DL-2 sample, as expected, while only a slight increase is observed for the bottom 0.5Pa layer. Based on previous research by Wu et al. [51], a 3% increase in the S-parameter for the 0.5Pa layer would be expected compared to the current 1.0 ± 1.4%. The limited increase in the S-parameter of the bottom layer is particularly notable, as significant hydrogen transport in the 0.5Pa layer would be expected, leaving behind vacancies in the crystal lattice. This aligns with our earlier discussion regarding the bleaching time of the DL-2 sample, where the higher bleaching time compared to the 0.5Pa single-layer samples could suggest that hydrogen movement within the bottom layer is affected. The still-lower S-parameter supports this hypothesis, indicating that hydrogen possibly remains trapped within the bottom thin film. As for the DL-1 sample, we modelled a decrease in the S-parameter, which could indicate the incorporation of more oxygen.

Double-Layers

The measurements performed on the double-layer samples highlighted the critical role of the bottom layer and its influence on the top layer. Both optical and XRD measurements indicated that the top 0.5Pa layer in the DL-1 sample is more oxidized compared to a 0.5Pa layer deposited directly on a clean substrate. In the optical measurements, no contribution was observed from the strong photochromic contrast or bleaching time constant typically associated with a 0.5Pa layer. Similarly, the XRD measurements revealed a higher-than-expected lattice constant (5.373 ± 0.004Å vs 5.347 ± 0.001Å), further supporting the presence of a higher oxidation grade.

Conversely, the DB-PAS measurements on DL-1 resulted in the expected S-parameter associated with 0.5Pa layers. However, the measurements did not provide insight into whether the higher-than-expected parameter in the 0.8Pa thin film is caused by a lower oxidation grade or an increased number of vacancies or nano porosity within the thin film. Based on the optical and XRD results, the increased oxidation and corresponding porosity of the 0.5Pa top layer appear to have influenced the homogeneity of the thin film, reducing its transparency.

The DL-2 sample featured a 0.8Pa top layer that closely resembled the 0.8Pa layer deposited on an empty substrate. While it is possible that this top layer experienced slight additional oxidation, the only evidence supporting this is the modelled S-parameter for the 0.8Pa layer (0.494 ± 0.002), which is significantly lower than the S-parameters of the 0.5Pa layer (0.523 ± 0.005) and the other 0.8Pa layer (0.529 ± 0.002).

When comparing the two double-layer samples, the porosity of the bottom layer likely has the most significant influence on the oxidation of the top layer. Increased porosity in the bottom layer appears to amplify the porosity of the deposited layer above. Figure 6.2 shows a schematic representation of this influence for both double-layer samples. Despite the impact on the top layer, the bottom layer retains its original photochromic contrast. However, a slight increase in the bleaching time constant is observed, which may be attributed to the effect of the bottom layer's capping on hydrogen transport.

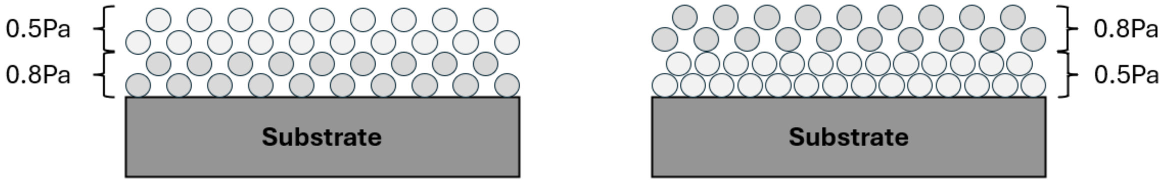

(a) Schematic porosity of DL-1 sample, with visible influence of 0.8Pa bottom layer on 0.5Pa top layer

(b) Schematic porosity of DL-2 sample, with little influence of 0.5Pa bottom layer on 0.8Pa top layer

Figure 6.2: Schematic porosity and effect of double-layer samples

The results provide insights into the influence that individual layers may exert on one another when deposited as part of a double-layer sample. However, the exact interaction between the two layers, particularly the hydrogen transport during photo-darkening and bleaching, remains unclear and needs further investigation. Additionally, determining the maximum allowable deposition pressure for the bottom layers before the top layer is influenced by its porosity would be an interesting area for further research. Based on the current findings, the 0.8Pa bottom layer in the DL-1 sample is too porous for a successful deposition of the second layer without affecting its properties.

7

Conclusion

The study of 0.8Pa thin films and the double-layers provides valuable insights into how deposition pressure, film thickness, and layer stacking influence photochromic properties of yttrium oxyhydride layers. 400nm thin films deposited at 0.8Pa show a lower photochromic contrast (11.4 ± 0.4%) than those deposited at 0.5Pa (53.0 ± 0.4%), confirming the inverse relationship between deposition pressure and photochromic performance. Previous research is further supported by the faster bleaching time constant observed in the 0.8Pa films (0.6 hours) compared to 0.5Pa films (5.1 hours). After multiple cycles, the observed reduction in photochromic contrast for the 0.8Pa samples could be attributed to their higher porosity, which could facilitate hydrogen effusion of weakly bound hydrogen even after the first cycle—leading to an increase in the O:H ratio and ultimately degrading photochromic performance over repeated illumination cycles. However, no conclusive cause was found through measurement methods, and further research is required.

Film thickness plays a significant role in determining photochromic properties. Thicker films (800nm) deposited at 0.8Pa show visible inhomogeneity and a greater phase diversity, leading to hydride-rich and hydride-poor regions, negatively influencing the photochromic contrast and visual characteristics. As expected, the photochromic contrast increased with thickness and the bleaching time constant remained unchanged. However, the maximum achievable photochromic contrast for 0.8Pa thin films appears to be constrained by the adverse effects of increased thickness on the film's homogeneity.

The results of the double-layers underline the bottom layer's influence on the top layer's properties. In the DL-1 sample, which features a 0.8Pa bottom layer, the 0.5Pa top layer shows significant oxidation and inhomogeneity, resulting in reduced photochromic contrast (29.7 ± 0.4%) and altered optical properties. This suggests that the higher porosity of the 0.8Pa bottom layer increases the porosity and, consequently, the oxidation of the top layer. Additionally, a higher absorption was obtained for the sample, but it remains unclear whether this is due to light scattering—which could not be measured due to a limitation in the experimental setup—or a higher presence of metallic clusters.

In contrast, the DL-2 sample, which features a 0.5Pa bottom layer, demonstrates minimal influence on the 0.8Pa top layer. The top layer retains its intrinsic photochromic properties, achieving a total photochromic contrast of 55.2 ± 0.4%, closely matching the theoretical prediction. The transmission and reflection measurements align well with expectations, and the lattice parameters show minimal changes compared to single-layer 0.8Pa films. This possibly indicates that the lower porosity of the 0.5Pa bottom layer has little effect on the top 0.8Pa layer, which initially has higher porosity, allowing it to maintain its structural and optical characteristics seen for a single 0.8Pa layer deposited on f-SiO_2. This is further supported by the DB-PAS measurements, which show an anticipated rise in the S-parameter for both layers following three illumination cycles.

The spectroscopic ellipsometry measurements on the DL-2 sample indicated that the weighted metallic cluster content was approximately the average between both single-layer samples, measured separately. However, the model exhibited differing metallic cluster fractions for the 0.5Pa and 0.8Pa layers compared to their single-layer counterparts, potentially suggesting hydrogen transport between the layers. Further investigation is required to confirm this hypothesis and draw definitive conclusions.

Additionally, the bleaching time constant in the DL-1 and DL-2 samples is higher than that of their bottom single-layer counterpart, indicating that the capping effect of the top layer could influence hydrogen transport in the bottom layer, slowing the bleaching process.

The porosity of the bottom layer emerges as a key factor in determining the properties of the top layer in double-layer configurations produced in two (sequential) deposition-oxidation cycles. Increased porosity in the bottom layer, as seen in the DL-1 sample, enhances the porosity and oxidation of the top layer, leading to reduced photochromic performance (lower photochromic contrast). In contrast, the lower porosity of the 0.5Pa bottom layer in the DL-2 sample minimizes its influence on the top layer, allowing it to retain its intrinsic properties. These findings highlight the importance of layer sequencing and the need to carefully control deposition pressures to optimize the performance of double-layer thin films.

In conclusion, this study demonstrates the critical role of deposition pressure, film thickness, and layer stacking in determining the photochromic properties of single- and double-layer thin films. Films deposited at higher pressures (0.8 Pa) exhibit faster bleaching, greater porosity, reduced photochromic performance, and increased inhomogeneity, the latter of which is only observed in thicker films. The bottom layer's porosity significantly influences the top layer's oxidation and homogeneity in double-layer configurations.

8

Recommendations

In this thesis, the photochromic properties of single- and double-layer thin films were observed using different measurement methods. Due to time restrictions there was no room to further expand on certain findings or subjects, thus in this sections some recommendations for future research are given.

First, the thickness of the higher-porosity single layers (0.8Pa) was shown to significantly impact both the photochromic contrast and the potential inhomogeneity of the thin film. Further investigation is needed to determine the exact influence of increasing thickness on inhomogeneity and to establish the critical thickness beyond which this effect occurs. Understanding how to mitigate inhomogeneity in these samples could make thicker porous films a viable solution for window applications, as they exhibit higher photochromic contrast and short bleaching time constants.

Second, the degradation of the photochromic effect after multiple cycles in the 0.8Pa thin films has not been previously reported and needs further investigation. Our research indicates that this degradation occurs in the 0.8Pa Pa films, whereas the 0.5Pa films remain unaffected, possibly suggesting that the porosity of the 0.8Pa Pa thin films could be a contributing factor. Future studies should explore deposition pressures between 0.5Pa and 0.8Pa Pa to determine whether this effect occurs at intermediate pressures and conduct a more detailed analysis of the samples using DB-PAS measurements. Additionally, extending the measurement period beyond 18 cycles could provide a definitive conclusion on whether the degradation stabilizes between 20% and 40%.

Third, the optical properties of various double-layer configurations could be investigated more extensively. This includes constructing samples with different deposition pressures in varying layer configurations to further examine the influence of the bottom layer on the characteristics of the top layer and determining the maximum pressure at which this effect occurs. Additionally, a broader range of samples will be required to draw definitive conclusions regarding the impact of bottom-layer capping on the bleaching time constant. A clearer understanding of the underlying mechanism driving the photochromic effect will provide further insight into the factors influencing the bleaching time constant.

Fourth, the interaction between the two layers in double-layer samples should be further investigated using spectroscopic ellipsometry (SE) models. In this study, lower and higher modelled metallic cluster content was observed for the 0.5Pa and 0.8Pa layers within the DL-2 sample, respectively, compared to their corresponding single-layer samples deposited in the same batch. This could indicate possible hydrogen transport between the two layers; however, as this conclusion is based on a single model, no definitive statement can be made. Further SE measurements on double-layer samples could provide additional insight into whether hydrogen transport occurs. Additionally, DB-PAS measurements during illumination could help identify vacancies created by hydrogen transport within double-layer samples, giving further insight in this interaction.

References

[1] H.P. Urbach A.P. Konijnenberg A.J.L. Adam. *BSc Optics*. Second Edition. TU Delft Open, 2022. ISBN: 978-94-6366-396-0.

[2] Elbruz Murat Baba et al. “Light-induced breathing in photochromic yttrium oxyhydrides”. In: *Physical Review Materials* 4.2 (2020), p. 025201.

[3] Elbruz Murat Baba et al. “Temperature-Dependent Photochromic Performance of Yttrium Oxyhydride Thin Films”. In: *physica status solidi (RRL)–Rapid Research Letters* 15.1 (2021), p. 2000459.

[4] Shrestha Banerjee et al. “Exploring multi-anion chemistry in yttrium oxyhydrides: solid-state NMR studies and DFT calculations”. In: *The Journal of Physical Chemistry C* 127.29 (2023), pp. 14303–14316.

[5] Melanie L.M. Beek. “Studying the evolution of photochromic rare-earth metal oxyhydride films with UV exposure & cycling using optical transmission, X-ray diffraction, positron annihilation & ellipsometry”. MA thesis. Delft University of Technology, 2022.

[6] J.A. Woollam Co. *CompleteEASE Software Manual*. Tech. rep. Lincoln, 2020.

[7] G Colombi. “Photochromism and photoconductivity in rare-earth oxyhydride thin films”. In: (2022).

[8] Giorgio Colombi et al. “Energy, metastability, and optical properties of anion-disordered RO x H 3- 2 x (R= Y, La) oxyhydrides: A computational study”. In: *Physical Review B* 105.5 (2022), p. 054208.

[9] Giorgio Colombi et al. “Influence of cation (RE= Sc, Y, Gd) and O/H anion ratio on the photochromic properties of REO x H3–2 x thin films”. In: *ACS photonics* 8.3 (2021), pp. 709–715.

[10] Giorgio Colombi et al. “Structure model for anion-disordered photochromic gadolinium oxyhydride thin films”. In: *The Journal of Physical Chemistry C* 124.25 (2020), pp. 13541–13549.

[11] Steffen Cornelius et al. “Oxyhydride nature of rare-earth-based photochromic thin films”. In: *The journal of physical chemistry letters* 10.6 (2019), pp. 1342–1348.

[12] Bernard Dam et al. “Perspective on the photochromic and photoconductive properties of Rare-Earth Oxyhydride thin films”. In: *Solar Energy Materials and Solar Cells* 273 (2024), p. 112921.

[13] Errol P EerNisse. “Compaction of ion-implanted fused silica”. In: *Journal of Applied Physics* 45.1 (1974), pp. 167–174.

[14] Rolf Enderlein and Norman JM Horing. *Fundamentals of semiconductor physics and devices*. World Scientific, 1997.

[15] Soniya Gahlawat et al. “Exploring Burstein–Moss type effects in nickel doped hematite dendrite nanostructures for enhanced photo-electrochemical water splitting”. In: *Physical Chemistry Chemical Physics* 21.36 (2019), pp. 20463–20477.

[16] Ragnhild Svellingen Hallaråker. “Temperature-and irradiation-dependent properties of photochromic thin films of YHx: O”. MA thesis. Norwegian University of Life Sciences, Ås, 2018.

[17] Christoph Hugenschmidt. “Positrons in surface physics”. In: *Surface Science Reports* 71.4 (2016), pp. 547–594. ISSN: 0167-5729. DOI: `https://doi.org/10.1016/j.surfrep.2016.09.002`. URL: `https://www.sciencedirect.com/science/article/pii/S0167572916300231`.

[18] Matt Hughes. *What is DC Sputtering?* `https://www.semicore.com/news/94-what-is-dc-sputtering`. Accessed: 14/09/24.

[19] Nahum Kipnis. *History of the Principle of Interference of Light*. Vol. 5. Birkhäuser, 2012.

[20] GG Libowitz and AJ Maeland. “Hydrides”. In: *Handbook on the physics and chemistry of rare earths* 3 (1979), pp. 299–336.

[21] Jan Petter Maehlen et al. “Lattice contraction in photochromic yttrium hydride”. In: *Journal of alloys and compounds* 580 (2013), S119–S121.

[22] Mahadevappa Mahesh. “The essential physics of medical imaging”. In: *Medical physics* 40.7 (2013), p. 077301.

[23] Patrycja Makuła, Michał Pacia, and Wojciech Macyk. *How to correctly determine the band gap energy of modified semiconductor photocatalysts based on UV–Vis spectra*. 2018.

[24] Ian H Malitson. “Interspecimen comparison of the refractive index of fused silica”. In: *Josa* 55.10 (1965), pp. 1205–1209.

[25] Thomas G Mayerhöfer, Susanne Pahlow, and Jürgen Popp. “The Bouguer-Beer-Lambert law: Shining light on the obscure”. In: *ChemPhysChem* 21.18 (2020), pp. 2029–2046.

[26] Dmitrii Moldarev et al. “a”. In: *Journal of Applied Physics* 129.15 (2021).

[27] Trygve Mongstad et al. “A new thin film photochromic material: Oxygen-containing yttrium hydride”. In: *Solar Energy Materials and Solar Cells* 95.12 (2011), pp. 3596–3599. ISSN: 0927-0248. DOI: `https://doi.org/10.1016/j.solmat.2011.08.018`. URL: `https://www.sciencedirect.com/science/article/pii/S0927024811004764`.

[28] José Montero, Augustinas Galeckas, and Smagul Z Karazhanov. “Photoluminescence properties of photochromic yttrium hydride films containing oxygen”. In: *physica status solidi (b)* 255.8 (2018), p. 1800139.

[29] José Montero and Smagul Z Karazhanov. “Spectroscopic Ellipsometry and Microstructure Characterization of Photochromic Oxygen-Containing Yttrium Hydride Thin Films”. In: *physica status solidi (a)* 215.19 (2018), p. 1701039.

[30] José Montero et al. “Photochromic mechanism in oxygen-containing yttrium hydride thin films: An optical perspective”. In: *Physical review B* 95.20 (2017), p. 201301.

[31] José Montero-Amenedo. “Photochromism in rare earth oxyhydrides for large-area transmittance control”. In: *Solar Energy Materials and Solar Cells* 272 (2024), p. 112900.

[32] Multiple. *Wave Interference*. `https://en.wikipedia.org/wiki/Wave_interference`. Accessed: 25/07/24.

[33] F Nafezarefi et al. “Effect of the addition of zirconium on the photochromic properties of yttrium oxy-hydride”. In: *Solar Energy Materials and Solar Cells* 200 (2019), p. 109923.

[34] F Nafezarefi et al. “Photochromism of rare-earth metal-oxy-hydrides”. In: *Applied Physics Letters* 111.10 (2017).

[35] TU Delft) Nafezarefi Fahimeh (PhD thesis. “Photochromic Properties of Rare-Earth Oxyhydrides”. In: (2020).

[36] KK Ng et al. “Electronic structure of lanthanum hydrides with switchable optical properties”. In: *Physical review letters* 78.7 (1997), p. 1311.

[37] James M Palmer. “The measurement of transmission, absorption, emission, and reflection”. In: *Handbook of optics* 2 (1995), pp. 25–1.

[38] MP Plokker et al. “Electronic structure and vacancy formation in photochromic yttrium oxy-hydride thin films studied by positron annihilation”. In: *Solar Energy Materials and Solar Cells* 177 (2018), pp. 97–105.

[39] Biswajit Sahoo. *Study of effect of cold working on Ni using Positron Annihilation Spectroscopy*. June 2014. DOI: `10.13140/RG.2.1.1981.8965`.

[40] MT Sakata and MJ Cooper. “An analysis of the Rietveld refinement method”. In: *Journal of Applied Crystallography* 12.6 (1979), pp. 554–563.

[41] Henk Schut. *Introduction to Nuclear Engineering*. 2023.

[42] Scott A Speakman. “Introduction to high resolution x-ray diffraction of epitaxial thin films”. In: *MIT Center for Materials Science and Engineering, Cambridge* (2012).

[43] H Stanjek and WJHl Häusler. “Basics of X-ray Diffraction”. In: *Hyperfine interactions* 154 (2004), pp. 107–119.

[44] CZ Tan. “Determination of refractive index of silica glass for infrared wavelengths by IR spectroscopy”. In: *Journal of Non-Crystalline Solids* 223.1-2 (1998), pp. 158–163.

[45] unkown. *Bandgap types*. `https://upload.wikimedia.org/wikipedia/commons/thumb/0/0b/Band_gap_comparison.svg/2000px-Band_gap_comparison.svg.png`. Accessed: 16/07/24.

[46] P Vajda. “Hydrogen in rare-earth metals, including RH2+ x phases”. In: *Handbook on the physics and chemistry of rare earths* 20 (1995), pp. 207–291.

[47] A van Veen et al. “Analysis of positron profiling data by means of ‘‘VEPFIT’’”. In: *AIP conference proceedings*. Vol. 218. 1. American Institute of Physics. 1991, pp. 171–198.

[48] Jakobus Hubertus Lambertus Voncken. *The rare earth elements: an introduction*. Springer, 2016.

[49] TU Delft) Wu Ziying (PhD thesis. “Formation of metallic-like nanodomains and vacancy defects in photochromic rareearth oxyhydride films”. In: (2024).

[50] Ziying Wu et al. “Formation of vacancies and metallic-like domains in photochromic rare-earth oxyhydride thin films studied by in-situ illumination positron annihilation spectroscopy”. In: *Physical review materials* 6.6 (2022), p. 065201.

[51] Ziying Wu et al. “Memory effect in photochromic rare-earth oxyhydride thin films studied by in situ positron annihilation spectroscopy upon photodarkening-bleaching cycling”. In: *Physical Review Materials* 8.4 (2024), p. 045201.

[52] Chang Chuan You et al. “The dependence of structural, electrical and optical properties on the composition of photochromic yttrium oxyhydride thin films”. In: *Materialia* 6 (2019), p. 100307.

[53] Andrew Zangwill. *Modern electrodynamics*. Cambridge University Press, 2013.

[54] Shaoqiang Zhang and Rongfu Xiao. “Yttrium oxide films prepared by pulsed laser deposition”. In: *Journal of applied physics* 83.7 (1998), pp. 3842–3848.

[55] M Zubkins et al. “Optical properties of oxygen-containing yttrium hydride thin films during and after the deposition”. In: *Vacuum* 203 (2022), p. 111218.

A

Appendix: Optical Measurements

A.1. Bleaching Time Constant

In figure A.1 the bleaching time constants are calculated using equation 2.14 in a python plot or all single layer samples from batch one and two. The measurement cycle depicted is the first type of measurement, with three cycles of 2.5 hours of illumination followed by 20 hours of bleaching.

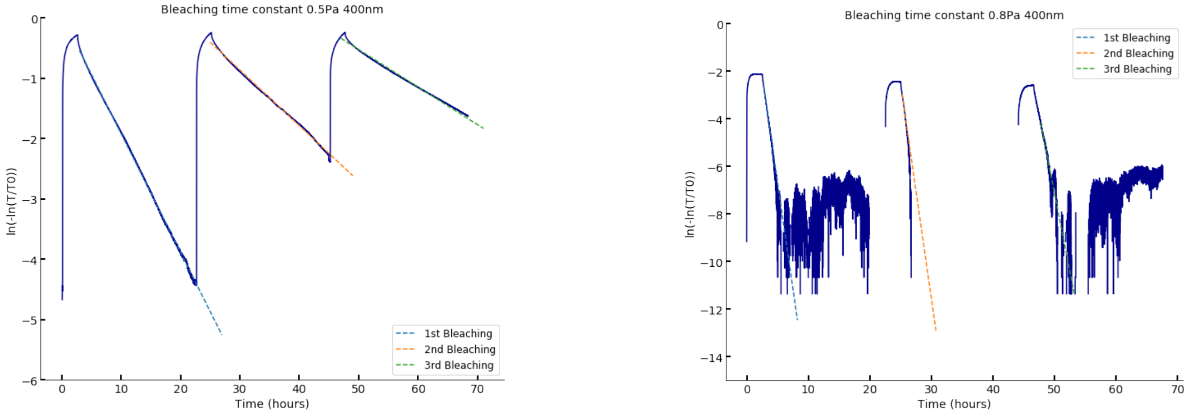

(a) 0.5Pa 400nm sample bleaching time constants of 5.08, 10.85 and 16.07 hours, respectively.

(b) 0.8Pa 400nm sample bleaching time constants of 0.56, 0.55 and 0.76 hours, respectively.

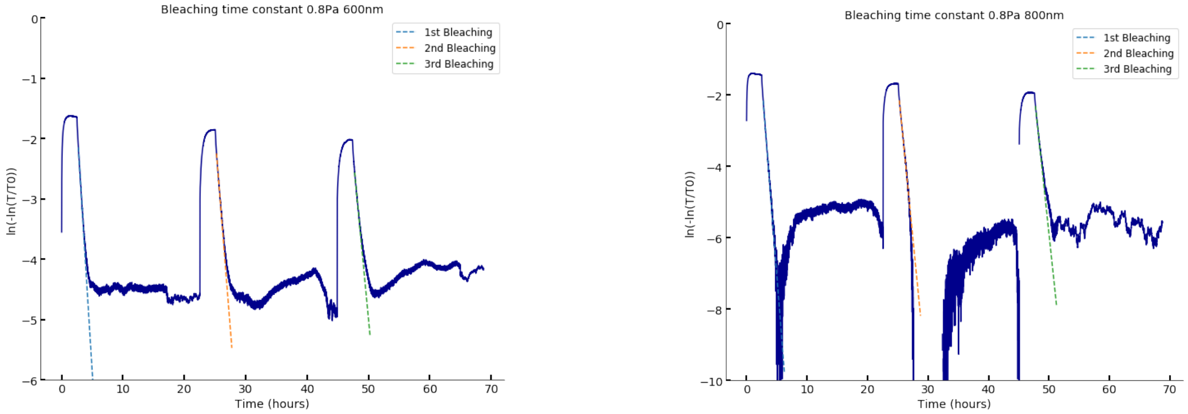

(c) 0.8Pa 600nm sample bleaching time constants of 0.61, 0.78 and 0.93 hours, respectively.

(d) 0.8Pa 800nm sample bleaching time constants of 0.46, 0.58 and 0.62 hours, respectively.

Figure A.1: Bleaching time constants of single layer samples

Below, in figure A.2 the bleaching time constants for the same illumination cycles as on the previous page are shown, but now for the third batch containing the double-layer samples and their respective bottom single-layers.

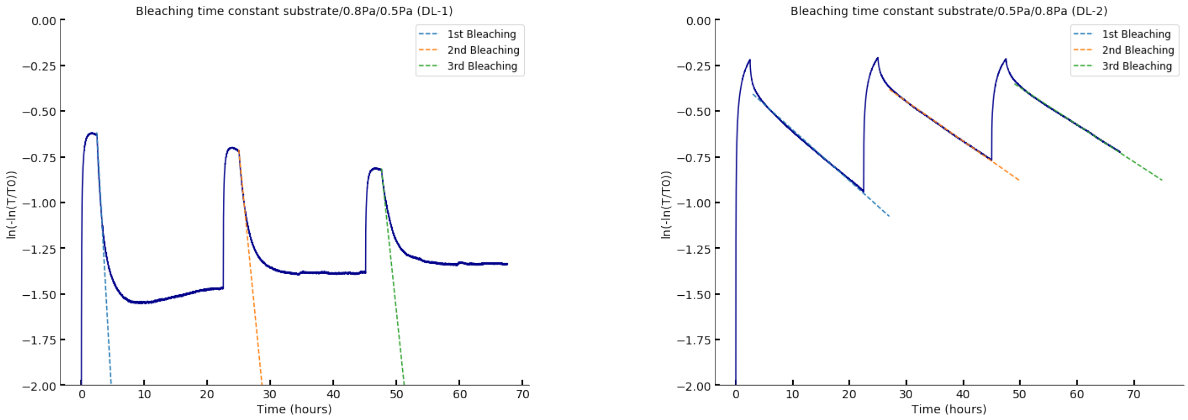

(a) DL-1 bleaching time constants of 1.64, 2.86 and 3.05 hours, respectively.

(b) DL-2 bleaching time constants of 35.85, 45.95 and 49.21 hours, respectively

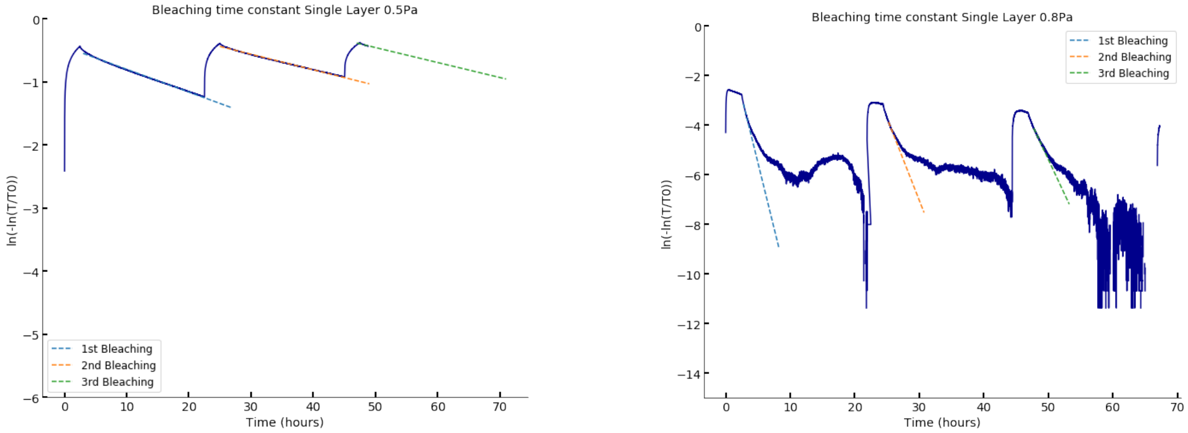

(c) 0.5Pa single-layer bleaching time constants of 27.72, 40.54 and 42.11 hours, respectively.

(d) 0.8Pa single-layer bleaching time constants of 0.95, 1.51 and 1.80 hours, respectively.

Figure A.2: Bleaching time constants of double layer samples

In figure A.3 the bleaching time constants for second type of measurement are shown. In this measurement the samples were illuminated for 2 hours after which they were given 2 hours to bleach back. The samples shown are a combination of the second and third batch.

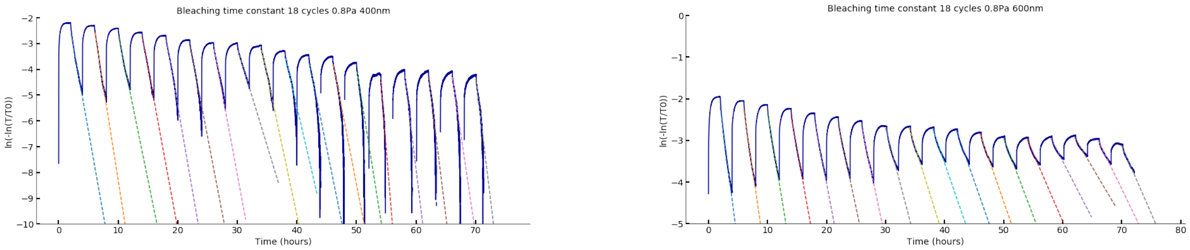

(a) Bleaching time constants of 0.8Pa 400nm sample, for 18 cycles.

(b) Bleaching time constants of 0.8Pa 600nm sample, for 18 cycles.

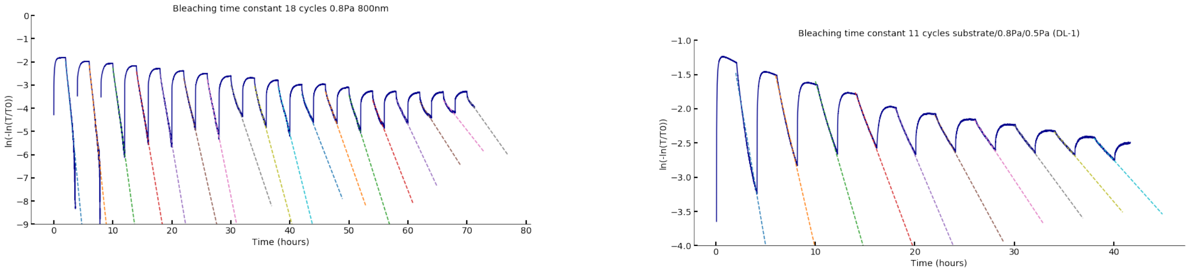

(c) Bleaching time constants of 0.8Pa 800nm sample, for 18 cycles.

(d) Bleaching time constants of DL-1 sample, for 11 cycles.

Figure A.3: Bleaching time constants of multiple cycle measurements.

A.2. Darkening Time Constant

The darkening time constants for all samples containing a 0.5Pa layer were extracted from the graphs in figure A.4. These constants were calculated with formula 2.17.

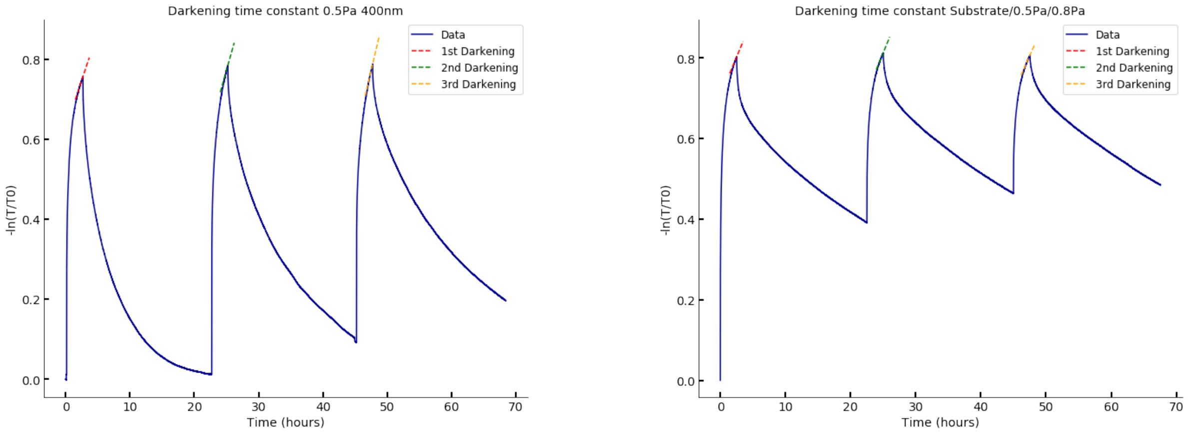

(a) 0.5Pa 400nm darkening time constants of 20.59, 17.49 and 14.67 hours, respectively.

(b) DL-2 darkening time constants of 25.85, 25.47 and 27.45 hours, respectively.

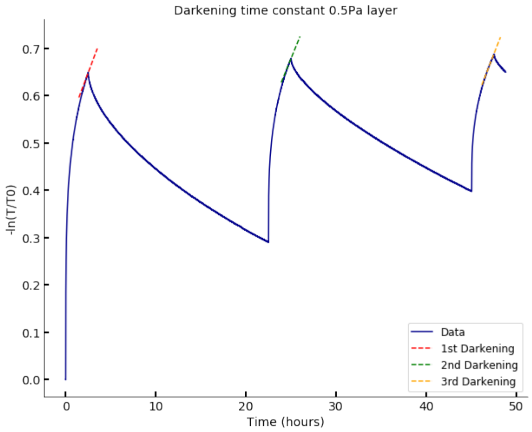

(c) 0.5Pa single-layer darkening time constants of 19.68, 21.42 and 20.46 hours, respectively.

Figure A.4: Darkening time constants of single layer samples

A.3. Tauc Plots

The Tauc plots for all samples are shown in this section. These tauc plots are calculated with formula 2.20.

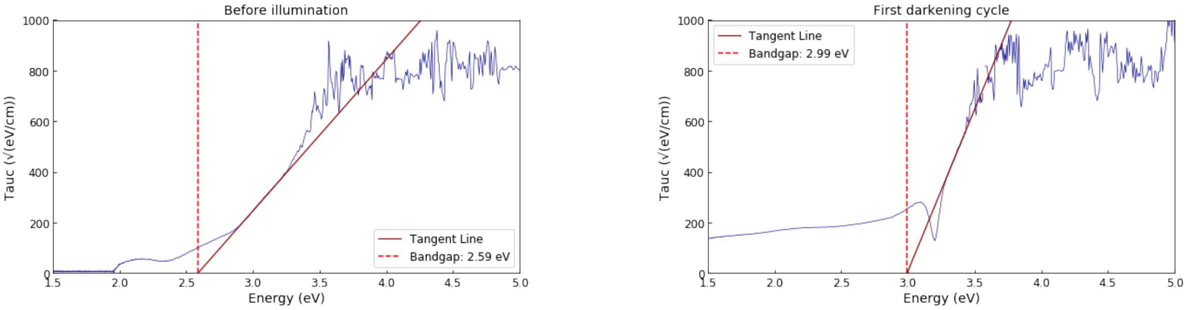

(a) Before illumination measurement with bandgap of 2.59 eV

(b) First darkening cycle with bandgap of 2.99 eV

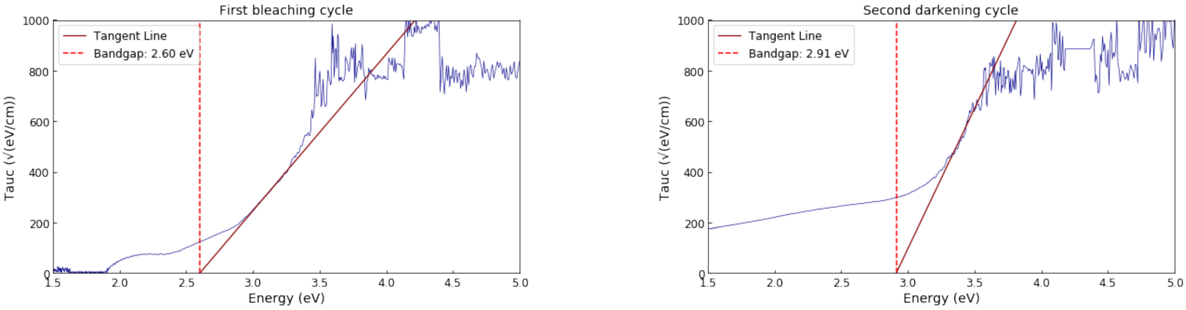

(c) First bleaching cycle with bandgap of 2.60 eV

(d) Second darkening cycle with bandgap of 2.91 eV

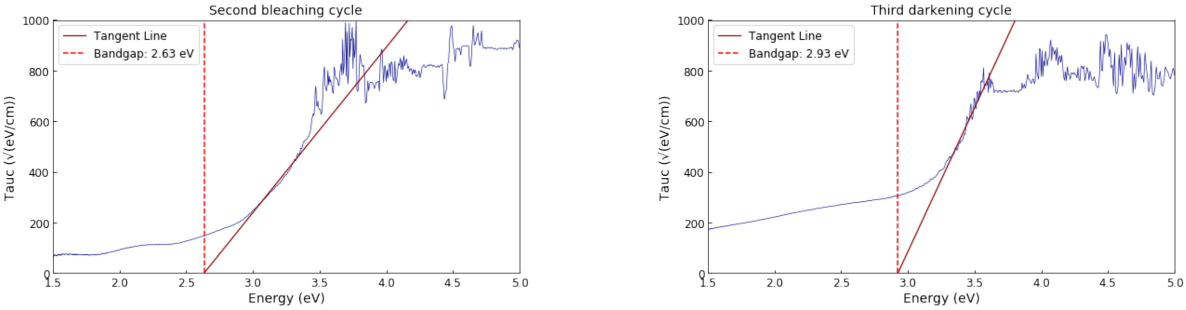

(e) Second bleaching cycle with bandgap of 2.63 eV

(f) Third darkening cycle with bandgap of 2.93 eV

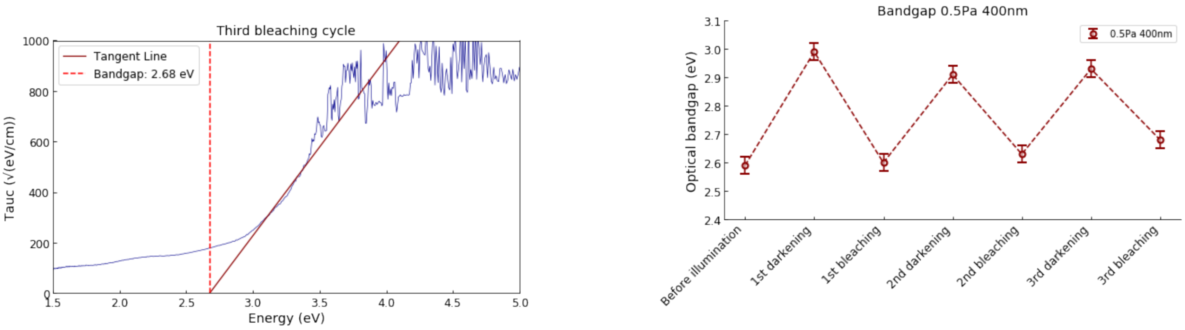

(g) Third bleaching cycle with bandgap of 2.68 eV

(h) All measured bandgaps of the 0.5Pa 400nm sample

Figure A.5: Tauc plots of 0.5Pa 400nm sample, giving the bandgap.

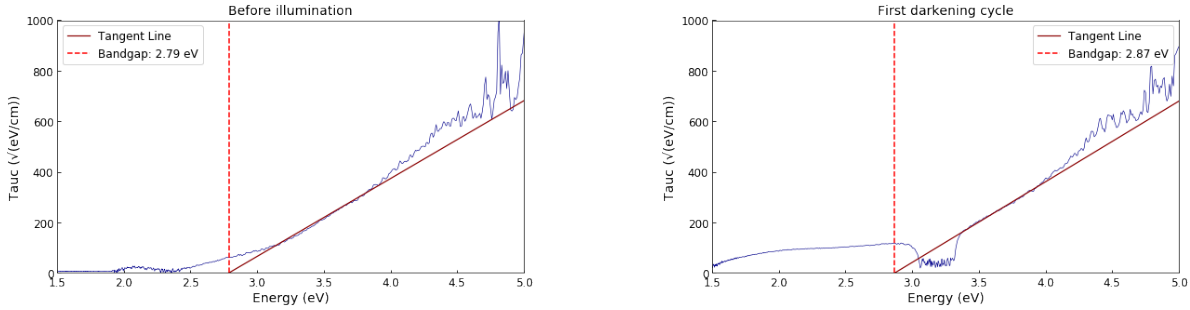

(a) Before illumination measurement with bandgap of 2.79 eV

(b) First darkening cycle with bandgap of 2.87 eV

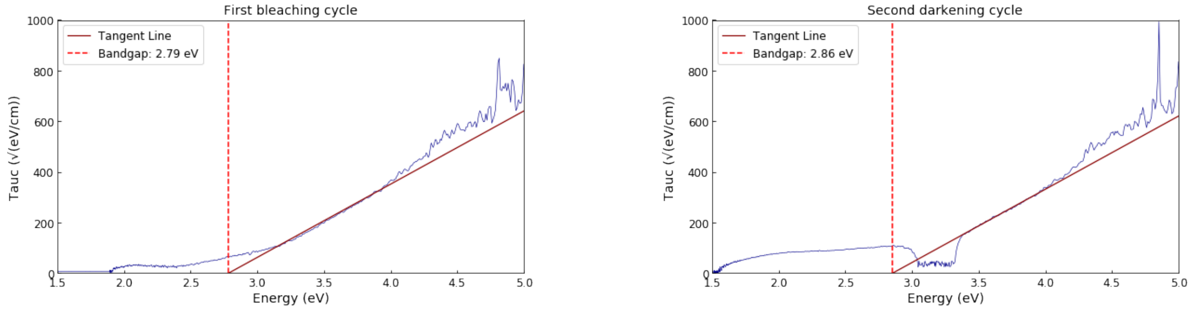

(c) First bleaching cycle with bandgap of 2.79 eV

(d) Second darkening cycle with bandgap of 2.86 eV

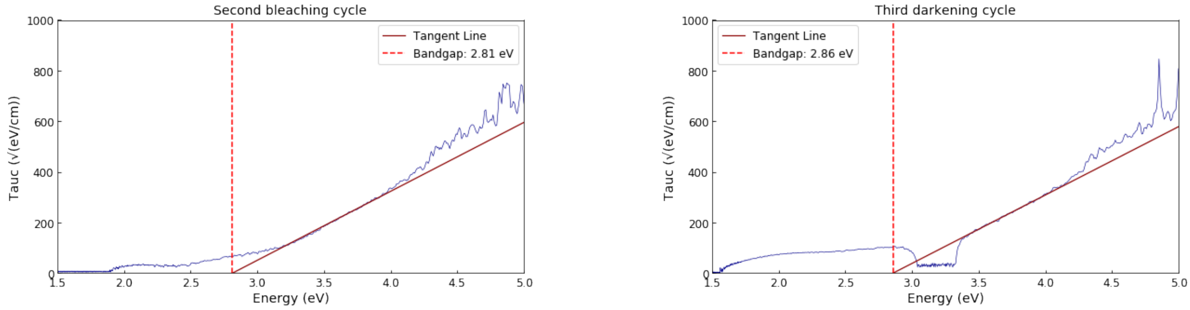

(e) Second bleaching cycle with bandgap of 2.81 eV

(f) Third darkening cycle with bandgap of 2.86 eV

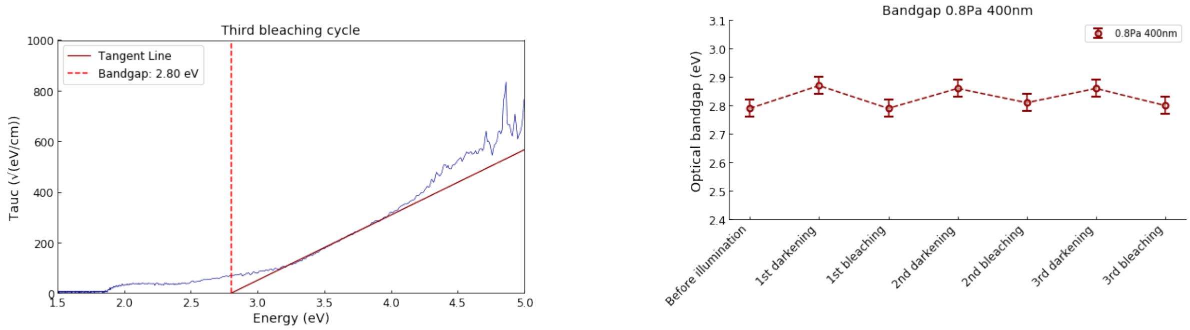

(g) Third bleaching cycle with bandgap of 2.81 eV

(h) All measured bandgaps of the 0.8Pa 400nm sample

Figure A.6: Tauc plots of 0.8Pa 400nm sample, giving the bandgap.

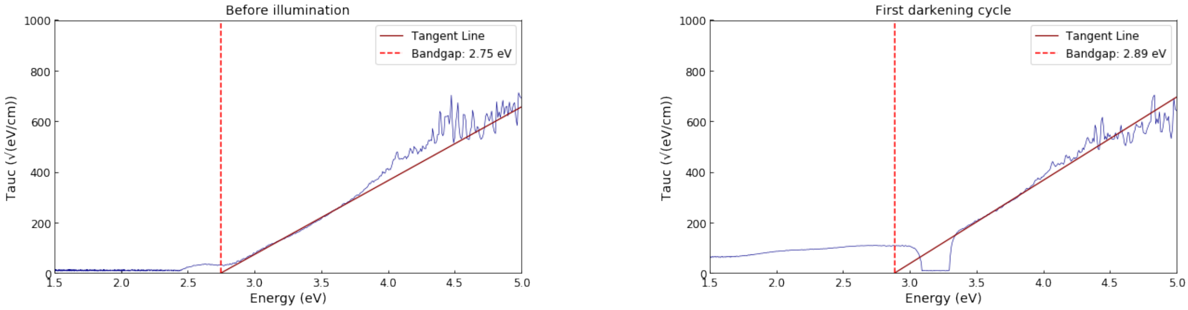

(a) Before illumination measurement with bandgap of 2.75 eV

(b) First darkening cycle with bandgap of 2.89 eV

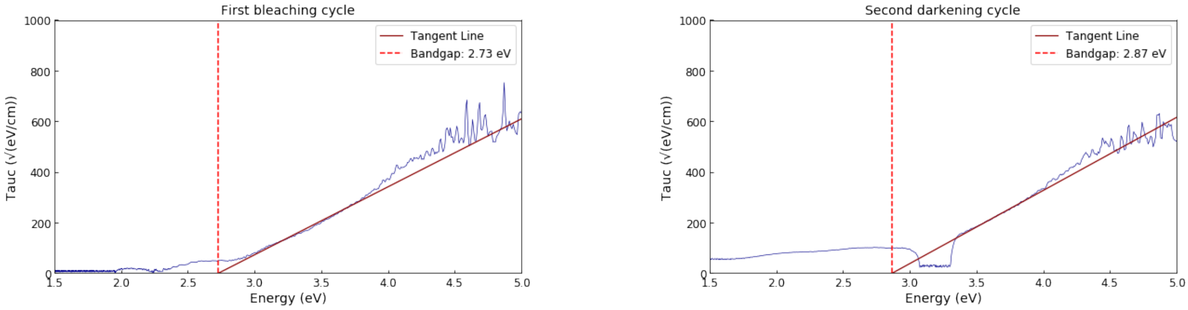

(c) First bleaching cycle with bandgap of 2.73 eV

(d) Second darkening cycle with bandgap of 2.87 eV

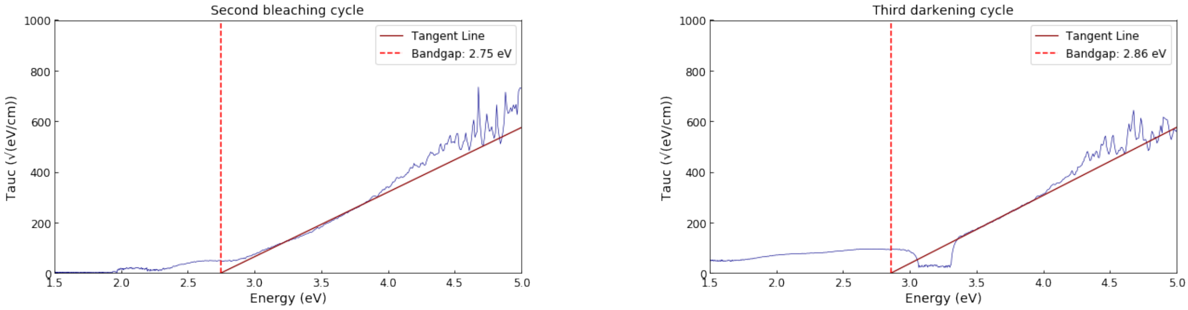

(e) Second bleaching cycle with bandgap of 2.75 eV

(f) Third darkening cycle with bandgap of 2.86 eV

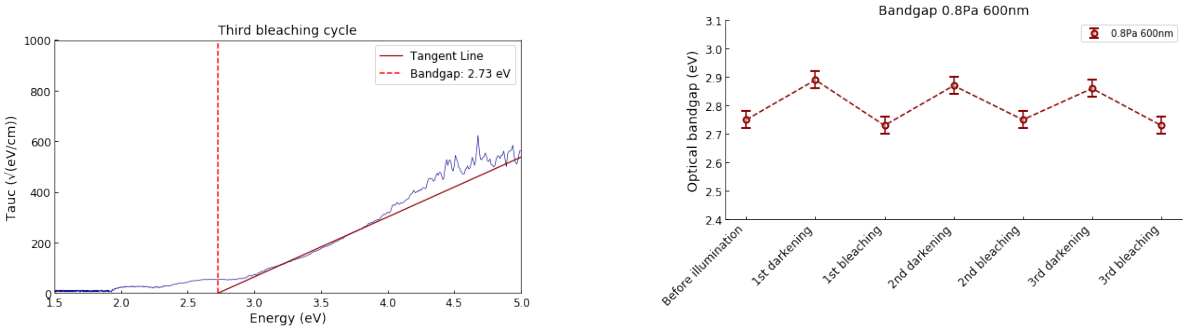

(g) Third bleaching cycle with bandgap of 2.75 eV

(h) All measured bandgaps of the 0.8Pa 600nm sample

Figure A.7: Tauc plots of 0.8Pa 600nm sample, giving the bandgap.

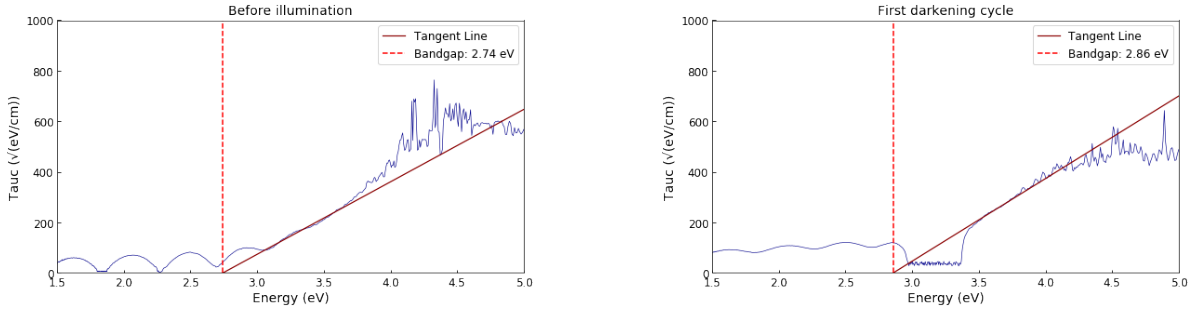

(a) Before illumination measurement with bandgap of 2.74 eV

(b) First darkening cycle with bandgap of 2.86 eV

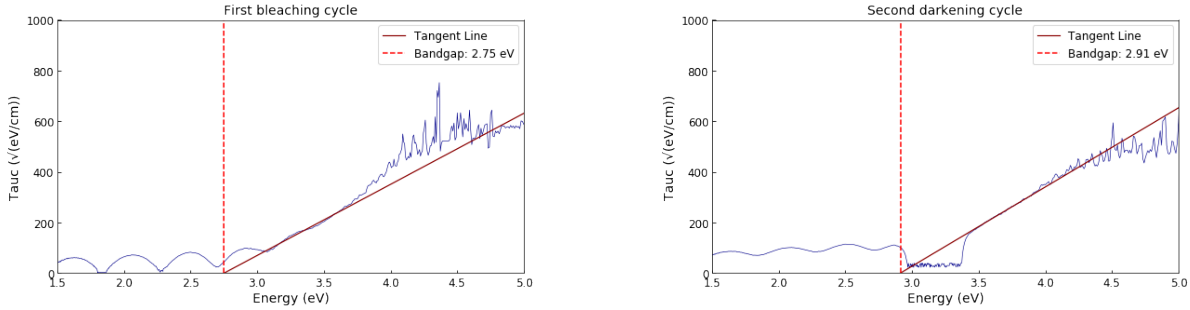

(c) First bleaching cycle with bandgap of 2.75 eV

(d) Second darkening cycle with bandgap of 2.91 eV

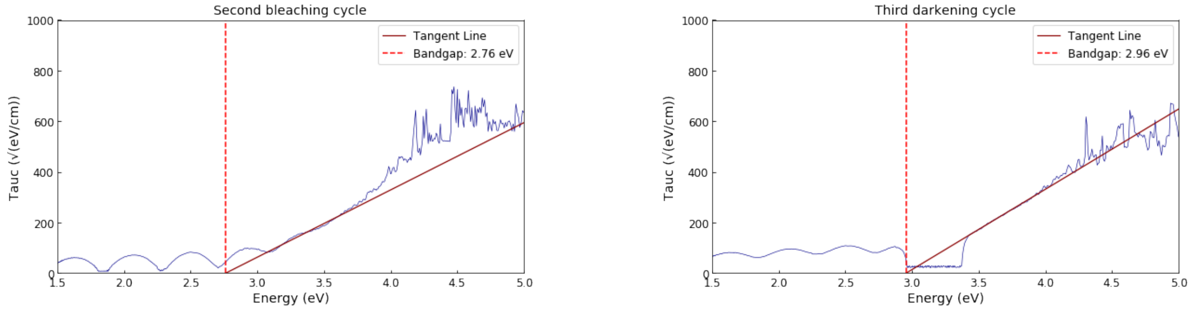

(e) Second bleaching cycle with bandgap of 2.76 eV

(f) Third darkening cycle with bandgap of 2.96 eV

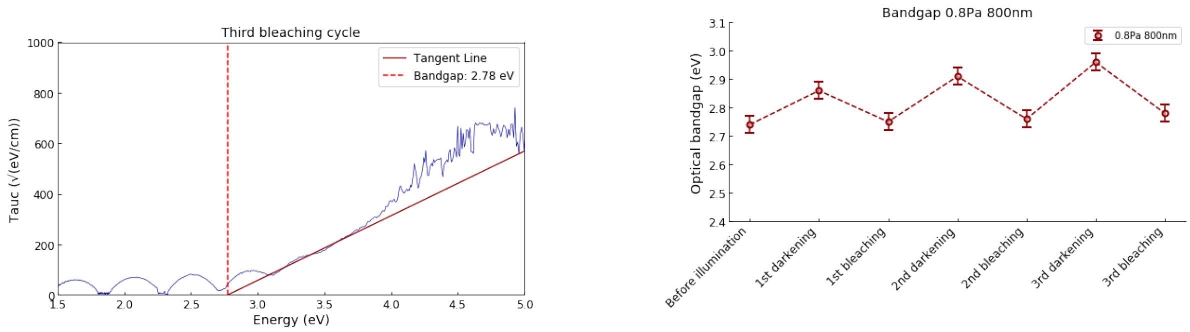

(g) Third bleaching cycle with bandgap of 2.78 eV

(h) All measured bandgaps of the 0.8Pa 800nm sample

Figure A.8: Tauc plots of 0.8Pa 800nm sample, giving the bandgap.

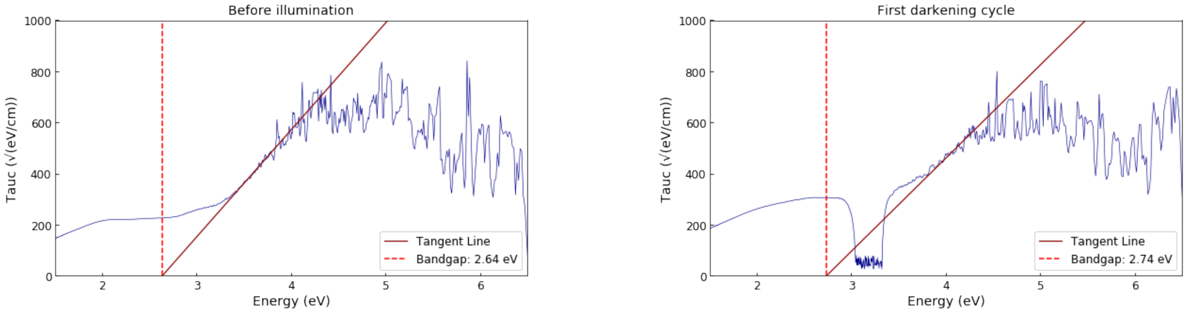

(a) Before illumination measurement with bandgap of 2.64 eV

(b) First darkening cycle with bandgap of 2.74 eV

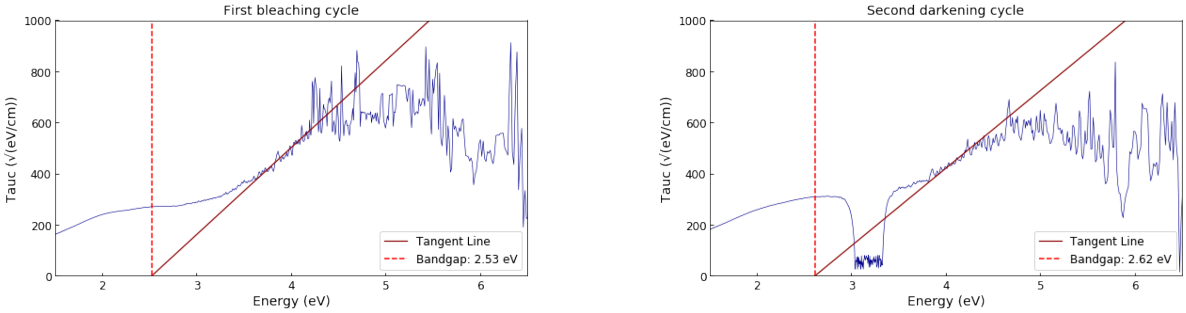

(c) First bleaching cycle with bandgap of 2.53 eV

(d) Second darkening cycle with bandgap of 2.62 eV

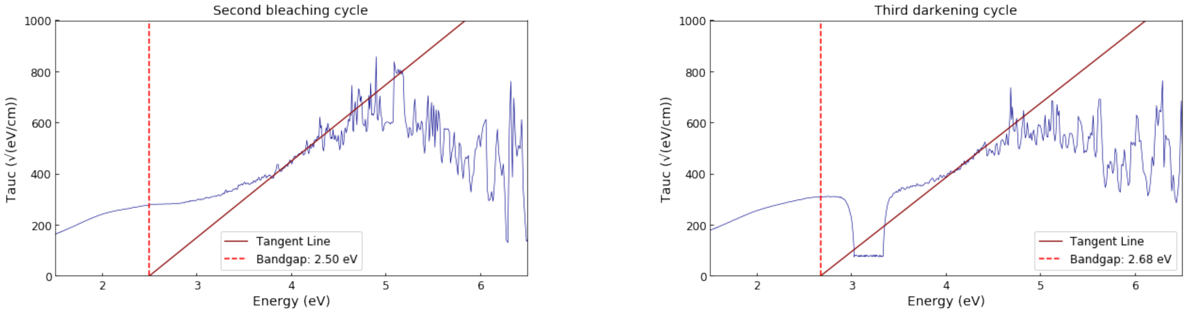

(e) Second bleaching cycle with bandgap of 2.50 eV

(f) Third darkening cycle with bandgap of 2.68 eV

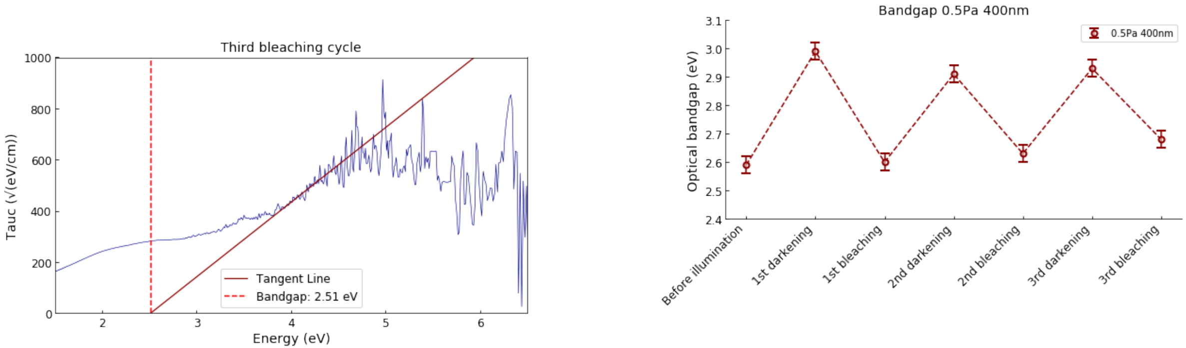

(g) Third bleaching cycle with bandgap of 2.51 eV

(h) All measured bandgaps of the double-layer substrate/0.8Pa/0.5Pa sample

Figure A.9: Tauc plots of substrate/0.8Pa/0.5Pa sample, giving the bandgap.

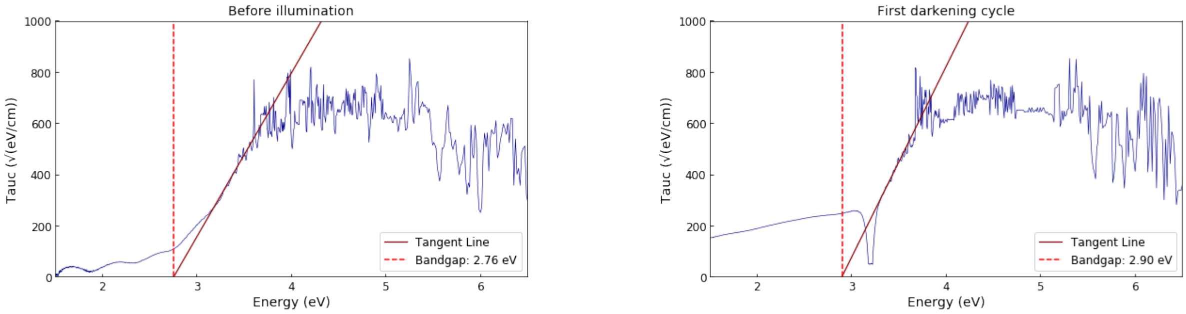

(a) Before illumination measurement with bandgap of 2.76 eV

(b) First darkening cycle with bandgap of 2.90 eV

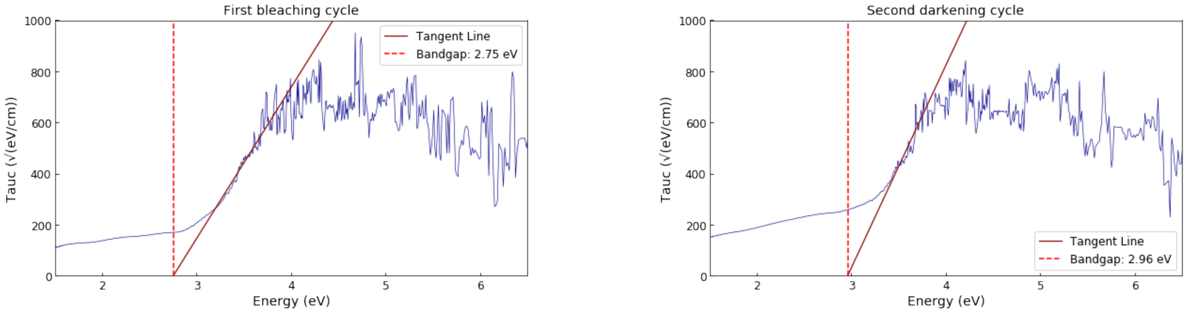

(c) First bleaching cycle with bandgap of 2.75 eV

(d) Second darkening cycle with bandgap of 2.96 eV

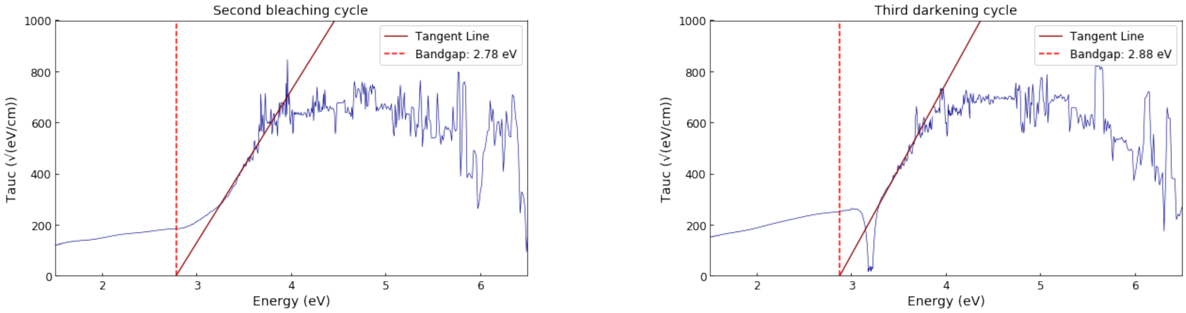

(e) Second bleaching cycle with bandgap of 2.78 eV

(f) Third darkening cycle with bandgap of 2.88 eV

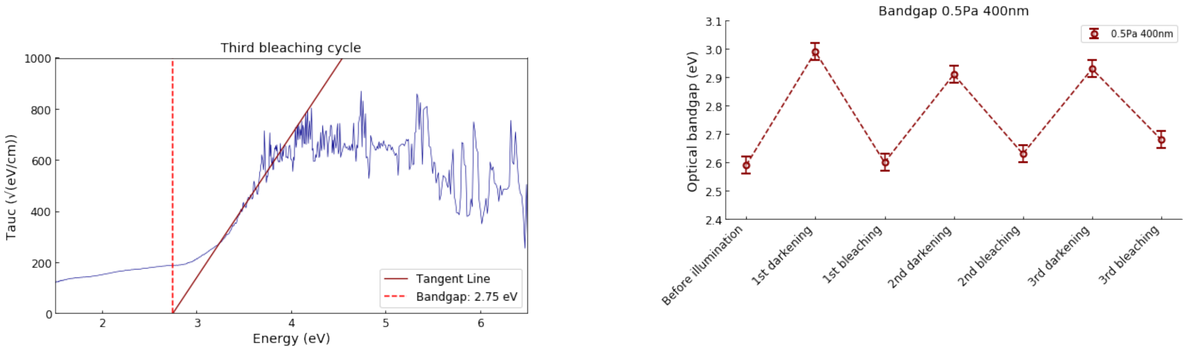

(g) Third bleaching cycle with bandgap of 2.75 eV

(h) All measured bandgaps of the double-layer substrate/0.5Pa/0.8Pa sample

Figure A.10: Tauc plots of Substrate/0.5Pa/0.8Pa sample, giving the bandgap.

A.4. Three Cycle Illumination

The transmission, reflection and absorption parameters from our first type of measurement for all samples are shown in the figures below. During this cycle the samples were illuminated for 2.5 hours, after which they were given the time to bleach back for 20 hours. The transmission and reflection are obtained with the PHOCS 2 setup, whereas the absorption was obtained with formula 2.1.

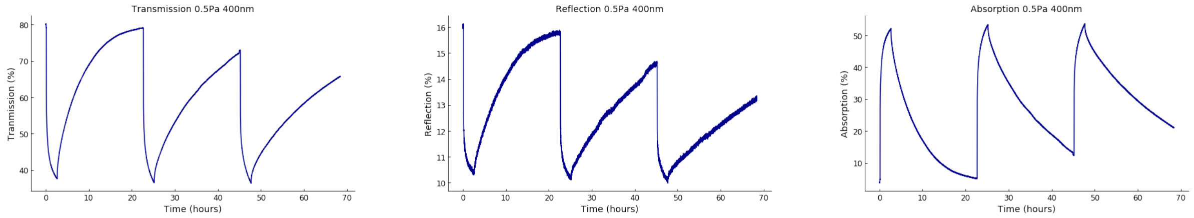

(a) Transmission coefficient **(b)** Reflection coefficient **(c)** Absorption coefficient

Figure A.11: Optical coefficients of 0.5Pa 400nm sample after three illumination cycles of 150 minutes of illumination and 1200 minutes of bleaching

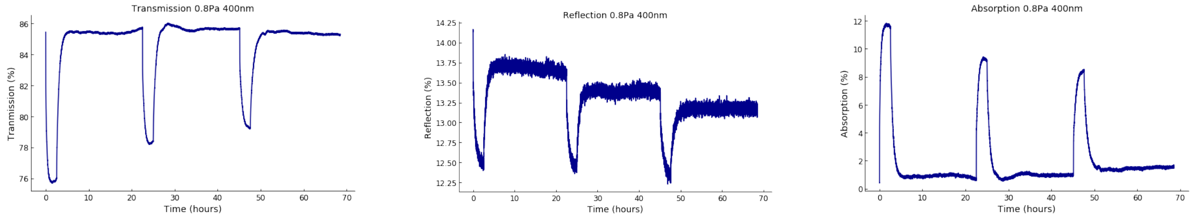

(a) Transmission coefficient **(b)** Reflection coefficient **(c)** Absorption coefficient

Figure A.12: Optical coefficients of 0.8Pa 400nm sample after three illumination cycles of 150 minutes of illumination and 1200 minutes of bleaching

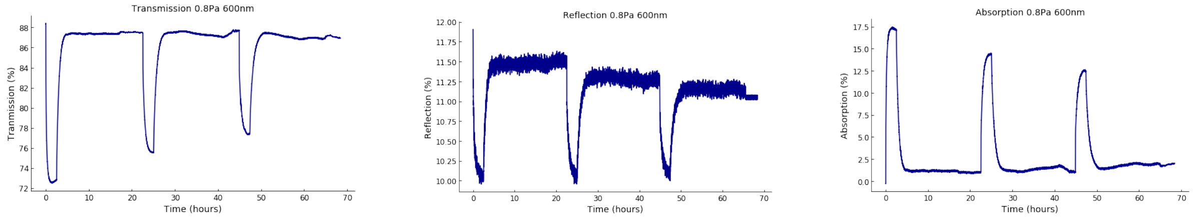

(a) Transmission coefficient **(b)** Reflection coefficient **(c)** Absorption coefficient

Figure A.13: Optical coefficients of 0.8Pa 600nm sample after three illumination cycles of 150 minutes of illumination and 1200 minutes of bleaching

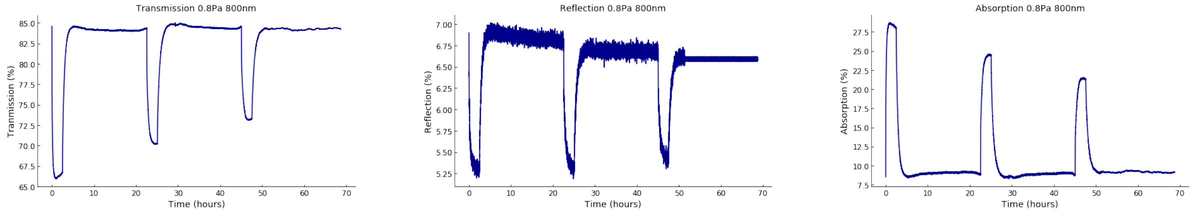

(a) Transmission coefficient **(b)** Reflection coefficient **(c)** Absorption coefficient

Figure A.14: Optical coefficients of 0.8Pa 800nm sample after three illumination cycles of 150 minutes of illumination and 1200 minutes of bleaching

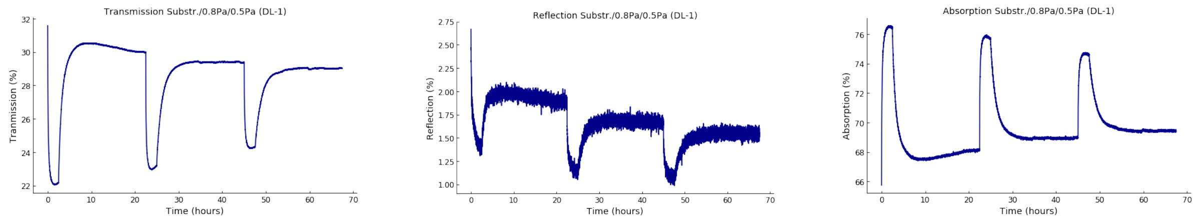

(a) Transmission coefficient **(b)** Reflection coefficient **(c)** Absorption coefficient

Figure A.15: Optical coefficients of substr./0.8Pa/0.5Pa sample after three illumination cycles of 150 minutes of illumination and 1200 minutes of bleaching

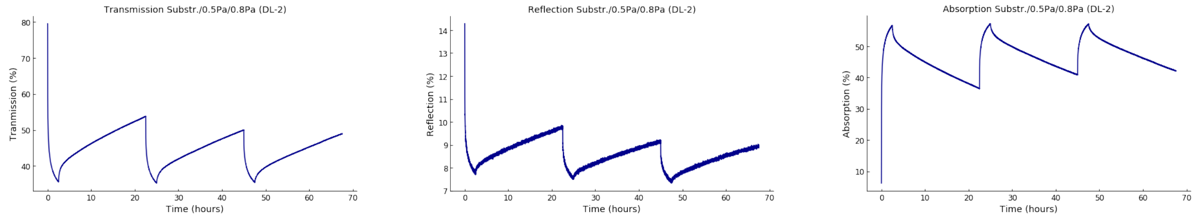

(a) Transmission coefficient **(b)** Reflection coefficient **(c)** Absorption coefficient

Figure A.16: Optical coefficients of substr./0.5Pa/0.8Pa sample after three illumination cycles of 150 minutes of illumination and 1200 minutes of bleaching

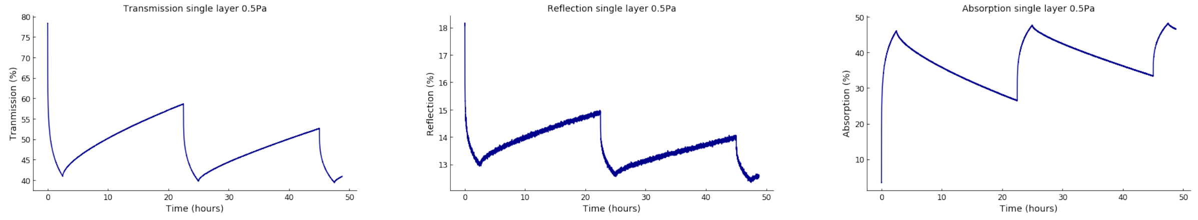

(a) Transmission coefficient **(b)** Transmission coefficient **(c)** Transmission coefficient

Figure A.17: Optical coefficients of 0.5Pa single layer sample used in double layers after three illumination cycles of 150 minutes of illumination and 1200 minutes of bleaching

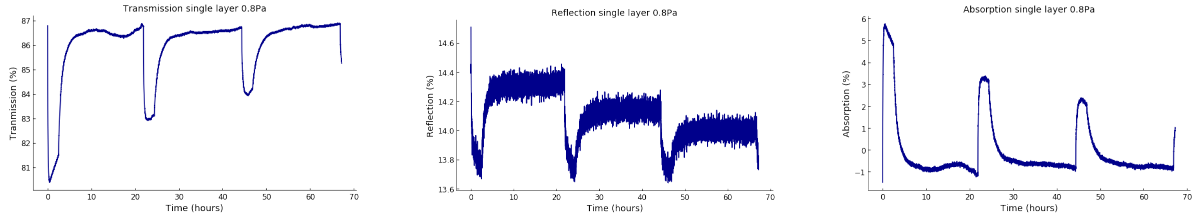

(a) Transmission coefficient **(b)** Transmission coefficient **(c)** Transmission coefficient

Figure A.18: Optical coefficients of 0.8Pa single layer sample used in double layers after three illumination cycles of 150 minutes of illumination and 1200 minutes of bleaching

A.5. Multiple Cycle Illumination

The transmission, reflection and absorption parameters from our second type of measurement are shown in the figures below. During this cycle the samples were illuminated for 2 hours, after which they were given the time to bleach back for another 2 hours. The transmission and reflection are obtained with the PHOCS 2 setup, whereas the absorption was obtained with formula 2.1.

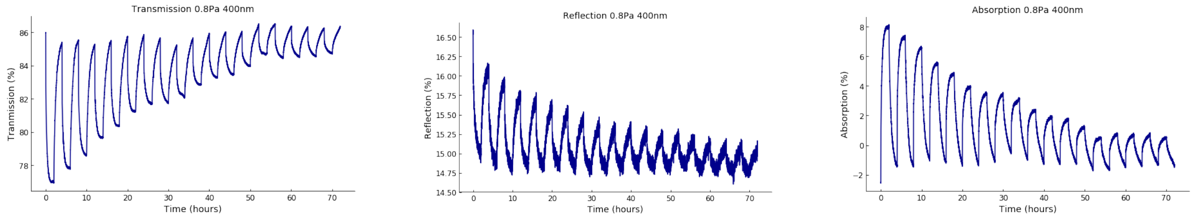

(a) Transmission coefficient **(b)** Reflection coefficient **(c)** Absorption coefficient

Figure A.19: Optical coefficients of 0.8Pa 400nm sample after eighteen illumination cycles of 120 minutes of illumination and 120 minutes of bleaching

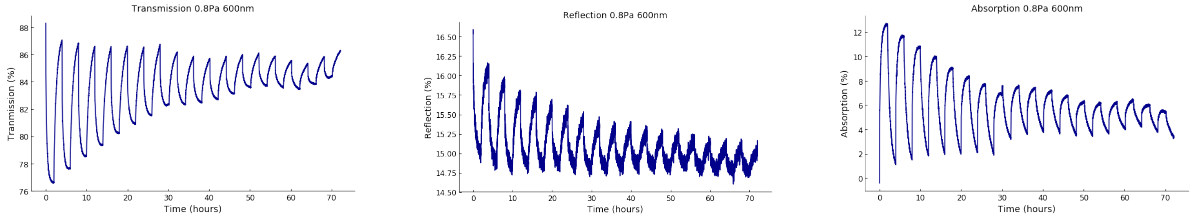

(a) Transmission coefficient **(b)** Reflection coefficient **(c)** Absorption coefficient

Figure A.20: Optical coefficients of 0.8Pa 600nm sample after eighteen illumination cycles of 120 minutes of illumination and 120 minutes of bleaching

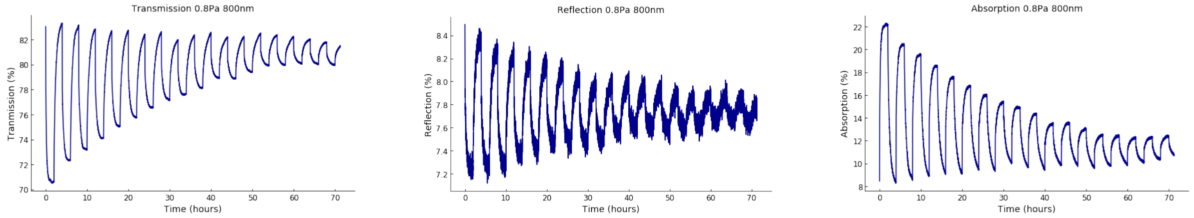

(a) Transmission coefficient **(b)** Reflection coefficient **(c)** Absorption coefficient

Figure A.21: Optical coefficients of 0.8Pa 800nm sample after eighteen illumination cycles of 120 minutes of illumination and 120 minutes of bleaching

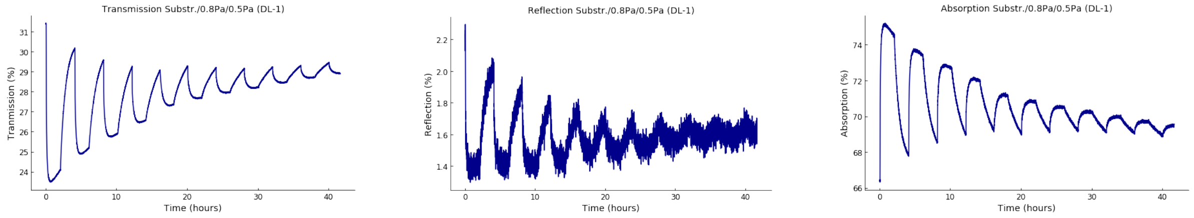

(a) Transmission coefficient **(b)** Reflection coefficient **(c)** Absorption coefficient

Figure A.22: Optical coefficients of substr./0.8Pa/0.5Pa sample after eleven illumination cycles of 120 minutes of illumination and 120 minutes of bleaching

A.6. Absorption coefficient

The absorption coefficient are calculated using formula 2.4 with the transmission and reflection which were extracted after 0, 10, 30, 60, 90, 120 and 150 minutes of illumination.

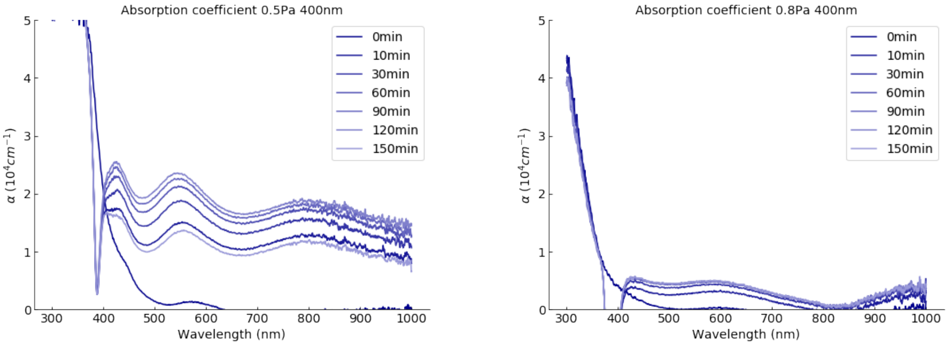

(a) Absorption coefficient 0.5Pa 400nm

(b) Absorption coefficient 0.8Pa 400nm

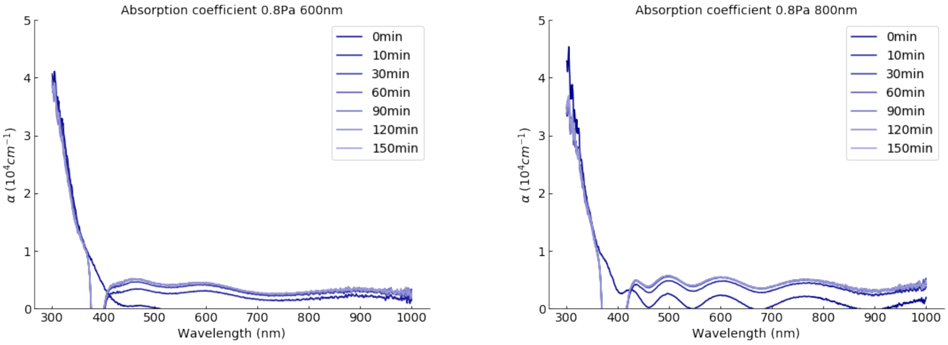

(c) Absorption coefficient 0.8Pa 600nm

(d) Absorption coefficient 0.8Pa 800nm

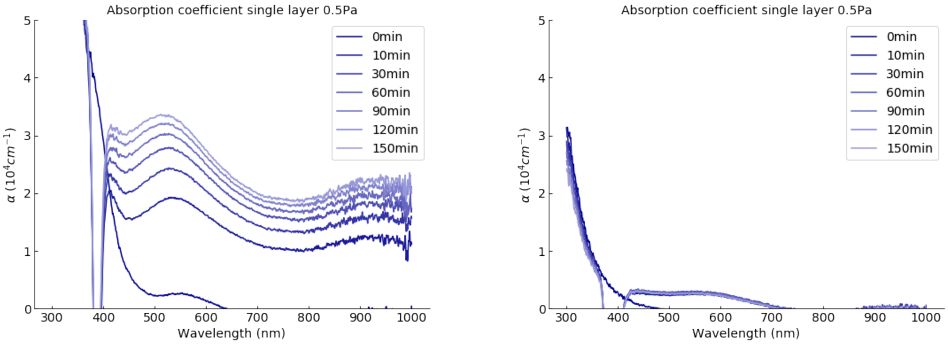

(e) Absorption coefficient single layer 0.5Pa

(f) Absorption coefficient single layer 0.8Pa

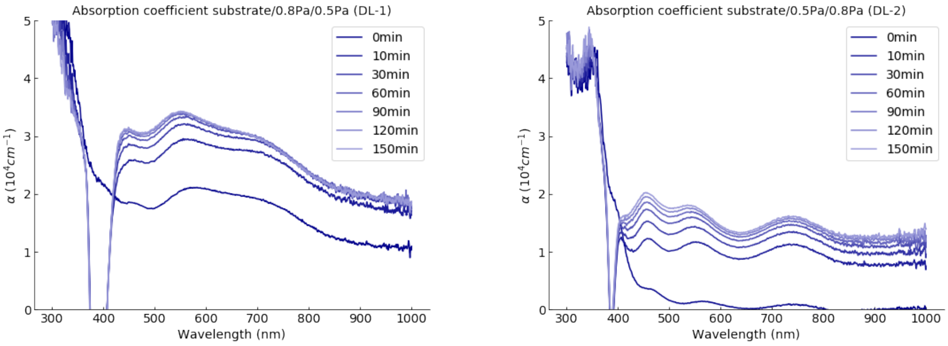

(g) Absorption coefficient substr./0.8Pa/0.5Pa

(h) Absorption coefficient substr./0.5Pa/0.8Pa

Figure A.23: Absorption coefficient samples over wavelength.

A.7. Measurement data

In the tables in this section, the measurment data for all three cycle measurements are given.

	Transparent	**Illu.**	**Bleaching**	**Illu.**	**Bleaching**	**Illu.**	**Bleaching**
T (%)	80.0	37.6	79.0	36.5	73.0	36.4	65.7
R (%)	16.0	10.4	15.8	10.2	14.6	10.0	13.2
A (%)	4.0	52.0	5.2	53.3	12.4	53.6	21.1
ΔT (%)	–	42.4	–	43.5	–	43.6	–
E_g (eV)	2.59	2.99	2.60	2.91	2.63	2.93	2.68
BTC (h)	–	–	5.08	–	10.85	–	16.07
$\frac{\Delta T}{T_0}$ (%)	–	53.0	–	54.4	–	54.5	–

Table A.1: Optical properties of the 0.5Pa 400nm sample over three cycles.

	Transparent	**Illu.**	**Bleaching**	**Illu.**	**Bleaching**	**Illu.**	**Bleaching**
T (%)	85.4	75.7	85.5	78.2	85.7	79.2	85.5
R (%)	14.2	12.5	13.7	12.4	13.4	12.3	13.2
A (%)	0.4	11.8	0.8	9.4	0.9	8.5	1.3
ΔT (%)	–	9.7	–	7.2	–	6.2	–
E_g (eV)	2.79	2.87	2.79	2.86	2.81	2.86	2.80
BTC (h)	–	–	0.56	–	-0.55	–	0.75
$\frac{\Delta T}{T_0}$ (%)	–	11.4	–	8.4	–	7.3	–

Table A.2: Optical properties of the 0.8Pa 400nm sample over three cycles.

	Transparent	**Illu.**	**Bleaching**	**Illu.**	**Bleaching**	**Illu.**	**Bleaching**
T (%)	88.4	72.5	87.4	75.7	87.7	77.4	87.2
R (%)	11.8	10.0	11.5	10.0	11.3	10.1	11.1
A (%)	-0.2	17.5	1.1	14.3	1.0	12.5	1.7
ΔT (%)	–	15.9	–	12.7	–	11.0	–
E_g (eV)	2.75	2.89	2.73	2.87	2.75	2.86	2.73
BTC (h)	–	–	0.61	–	0.78	–	0.93
$\frac{\Delta T}{T_0}$ (%)	–	18.0	–	14.4	–	12.4	–

Table A.3: Optical properties of the 0.8Pa 600nm sample over three cycles.

	Transparent	**Illu.**	**Bleaching**	**Illu.**	**Bleaching**	**Illu.**	**Bleaching**
T (%)	84.5	66.1	84.3	70.3	84.4	73.2	85.1
R (%)	6.8	5.4	6.8	5.4	6.7	5.3	6.7
A (%)	8.7	28.5	8.9	24.3	8.9	21.5	8.2
ΔT (%)	–	18.4	–	14.2	–	11.3	–
E_g (eV)	2.74	2.86	2.75	2.91	2.76	2.96	2.78
BTC (h)	–	–	0.46	–	0.58	–	0.62
$\frac{\Delta T}{T_0}$ (%)	–	21.8	–	16.8	–	13.4	–

Table A.4: Optical properties of the 0.8Pa 800nm sample over three cycles.

	Transparent	**Illu.**	**Bleaching**	**Illu.**	**Bleaching**	**Illu.**	**Bleaching**
T (%)	31.6	22.2	30.0	23.2	29.4	24.3	29.0
R (%)	2.7	1.5	1.9	1.1	1.7	1.1	1.5
A (%)	65.8	76.4	68.2	75.7	68.9	74.6	69.4
ΔT (%)	–	9.4	–	8.4	–	7.3	–
E_g (eV)	2.64	2.74	2.53	2.62	2.50	2.68	2.51
BTC (h)	–	–	1.64	–	2.86	–	3.05
$\frac{\Delta T}{T_0}$ (%)	–	29.7	–	26.5	–	23.1	–

Table A.5: Optical properties of the substrate/0.8Pa/0.5Pa (DL-1) sample over three cycles.

	Transparent	**Illu.**	**Bleaching**	**Illu.**	**Bleaching**	**Illu.**	**Bleaching**
T (%)	79.5	35.6	53.8	35.3	50.0	35.5	48.9
R (%)	14.2	7.7	9.8	7.5	9.2	7.4	8.9
A (%)	6.3	56.7	36.4	57.2	40.8	57.1	42.2
ΔT (%)	–	43.9	–	44.2	–	44.0	–
E_g (eV)	2.76	2.90	2.75	2.96	2.78	2.88	2.75
BTC (h)	–	–	35.85	–	45.95	–	49.21
$\frac{\Delta T}{T_0}$ (%)	–	55.2	–	55.6	–	55.4	–

Table A.6: Optical properties of the substrate/0.5Pa/0.8Pa (DL-2) sample over three cycles.

B

Appendix: Spectroscopic Ellipsometry

B.1. CompleteEASE Software fit

The modelled CompleteEASE Software fits for all samples are shown in the graphs below. These figures show how the Ψ and Δ change for different wavelengths, for all three angles we measured.

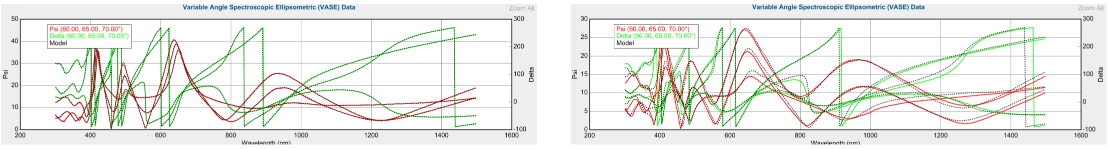

(a) Before illumination B-spline and Cauchy EMA model, 7.02 MSE.

(b) 10 minutes of illumination B-spline and Cauchy EMA model, 33.02 MSE.

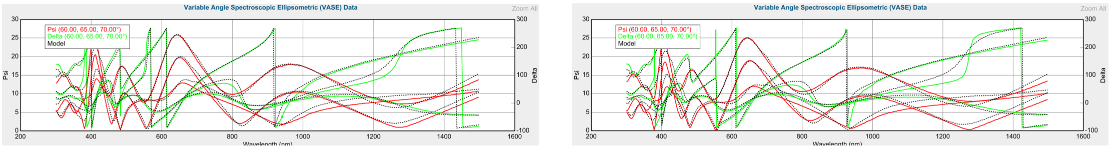

(c) 30 minutes of illumination B-spline and Cauchy EMA model, 32.19 MSE.

(d) 60 minutes of illumination B-spline and Cauchy EMA model, 31.27 MSE.

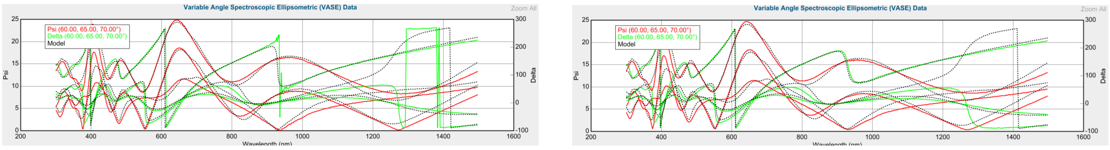

(e) 90 minutes of illumination B-spline and Cauchy EMA model, 31.18 MSE.

(f) 120 minutes of illumination B-spline and Cauchy EMA model, 31.44 MSE.

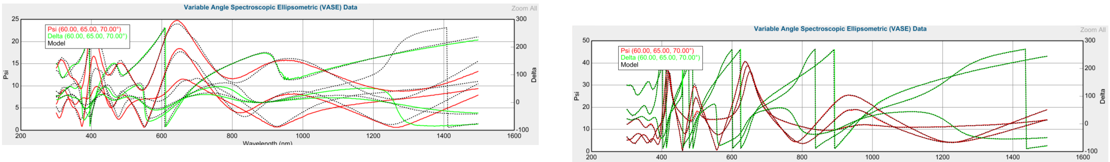

(g) 150 minutes of illumination B-spline and Cauchy EMA model, 31.85 MSE.

(h) Bleached B-spline and Cauchy EMA model, 13.88 MSE.

Figure B.1: CompleteEase Software model mode for substrate/0.5Pa/0.8Pa sample using a B-spline and Cauchy model

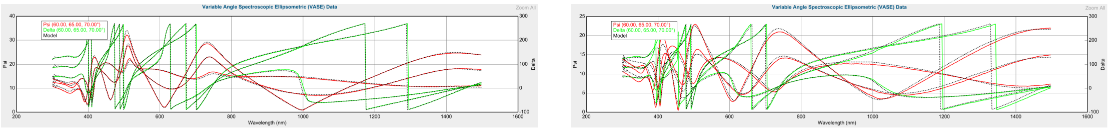

(a) Before illumination B-spline EMA model, 11.64 MSE.

(b) 10 minutes of illumination B-spline EMA model, 23.49 MSE.

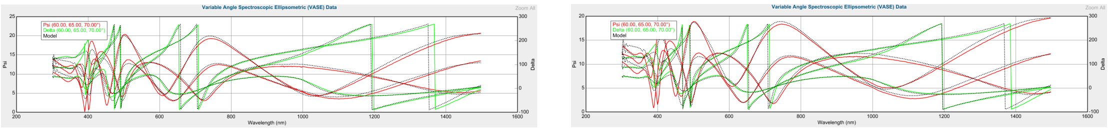

(c) 30 minutes of illumination B-spline EMA model, 24.22 MSE.

(d) 60 minutes of illumination B-spline EMA model, 23.48 MSE.

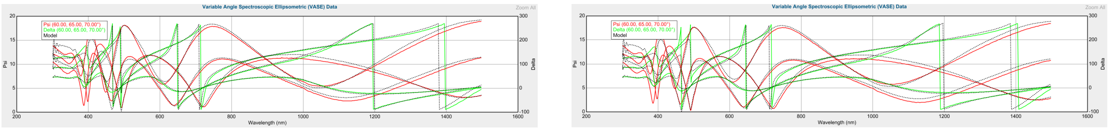

(e) 90 minutes of illumination B-spline EMA model, 22.93 MSE.

(f) 120 minutes of illumination B-spline EMA model, 22.64 MSE.

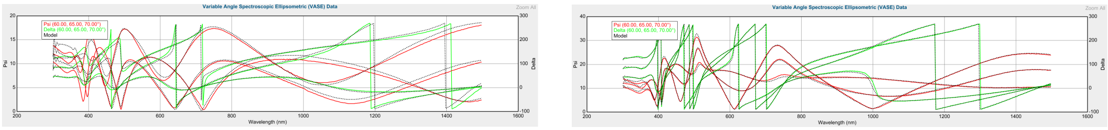

(g) 150 minutes of illumination B-spline EMA model, 22.55 MSE.

(h) Bleached B-spline EMA model, 12.06 MSE.

Figure B.2: CompleteEase Software model mode for 0.5Pa 400nm sample using B-spline layer

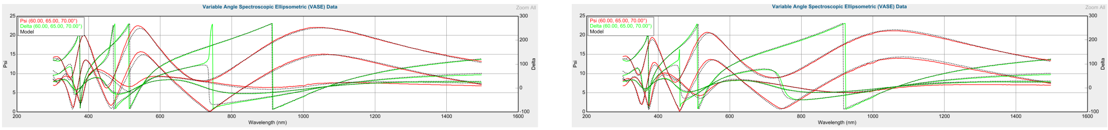

(a) Before illumination Cauchy EMA model, 12.94 MSE.

(b) 10 minutes of illumination Cauchy EMA model, 11.24 MSE.

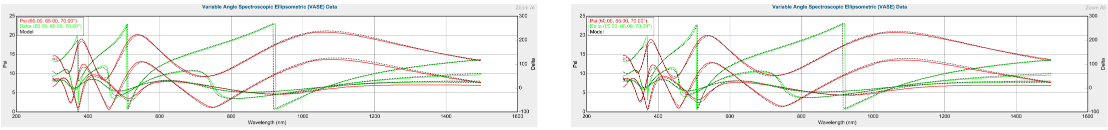

(c) 30 minutes of illumination Cauchy EMA model, 11.03 MSE.

(d) 60 minutes of illumination Cauchy EMA model, 11.39 MSE.

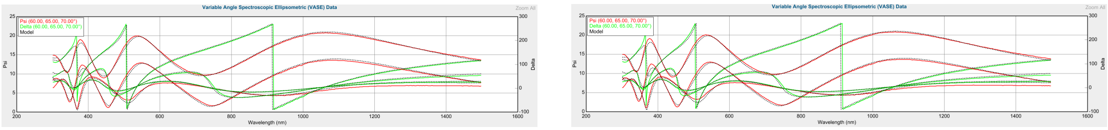

(e) 90 minutes of illumination Cauchy EMA model, , 11.99 MSE.

(f) 120 minutes of illumination Cauchy EMA model, 12.65 MSE.

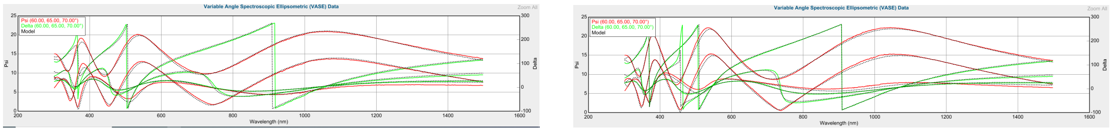

(g) 150 minutes of illumination Cauchy EMA model, 13.34MSE.

(h) Bleached Cauchy EMA model, 11.49 MSE.

Figure B.3: CompleteEase Software model mode for 0.8Pa 400nm sample using B-spline layer

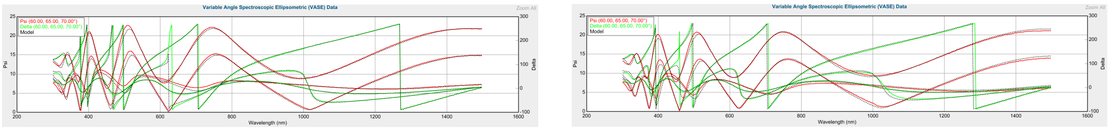

(a) Before illumination Cauchy EMA model, 13.82 MSE.

(b) 10 minutes of illumination Cauchy EMA model, 12.65 MSE.

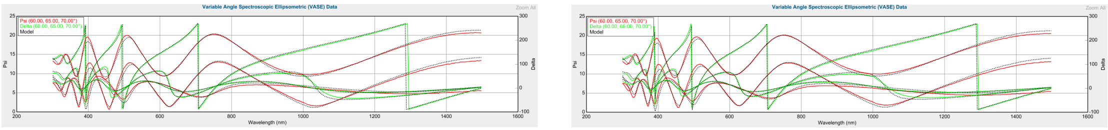

(c) 30 minutes of illumination Cauchy EMA model, 13.17 MSE.

(d) 60 minutes of illumination Cauchy EMA model, 13.90 MSE.

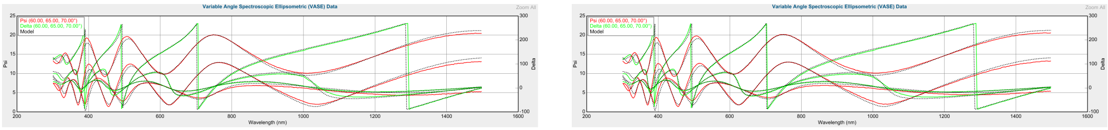

(e) 90 minutes of illumination Cauchy EMA model, 14.61 MSE.

(f) 120 minutes of illumination Cauchy EMA model, 15.17 MSE.

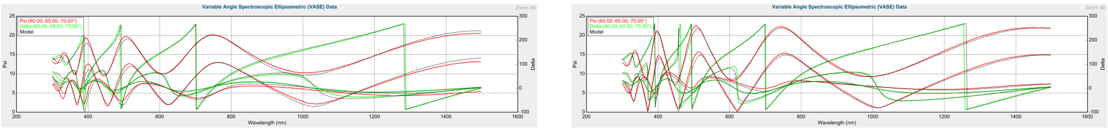

(g) 150 minutes of illumination Cauchy EMA model, 15.89 MSE.

(h) Bleached Cauchy EMA model, 12.41 MSE.

Figure B.4: CompleteEase Software model mode for 0.8Pa 600nm sample using B-spline layer

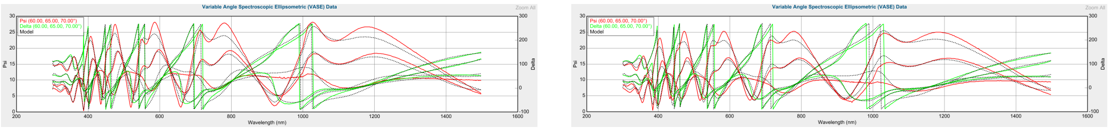

(a) Before illumination B-spline EMA model, 40.19 MSE.

(b) 10 minutes of illumination B-spline EMA model, 36.16 MSE.

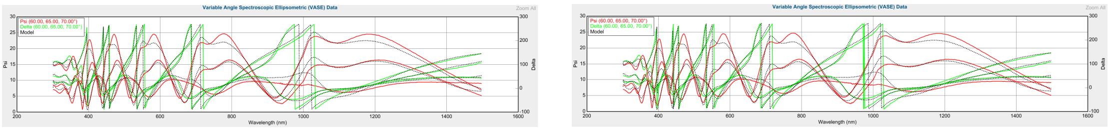

(c) 30 minutes of illumination B-spline EMA model, 36.26 MSE.

(d) 60 minutes of illumination B-spline EMA model, 36.74 MSE.

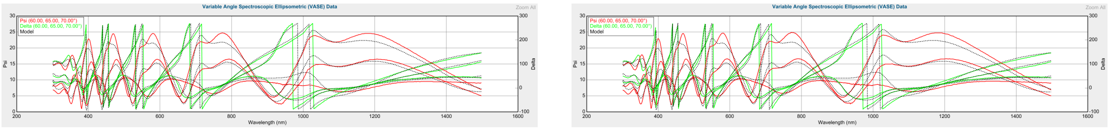

(e) 90 minutes of illumination B-spline EMA model, 37.65 MSE.

(f) 120 minutes of illumination B-spline EMA model, 38.59 MSE.

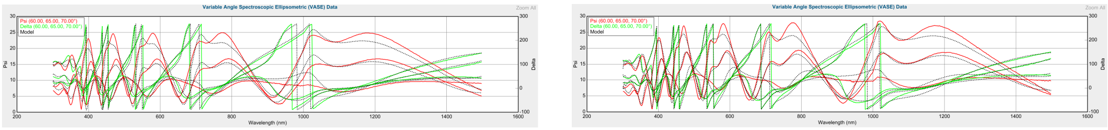

(g) 150 minutes of illumination B-spline EMA model, 39.57 MSE.

(h) Bleached B-spline EMA model, 39.13 MSE.

Figure B.5: CompleteEase Software model mode for 0.8Pa 800nm sample using B-spline layer

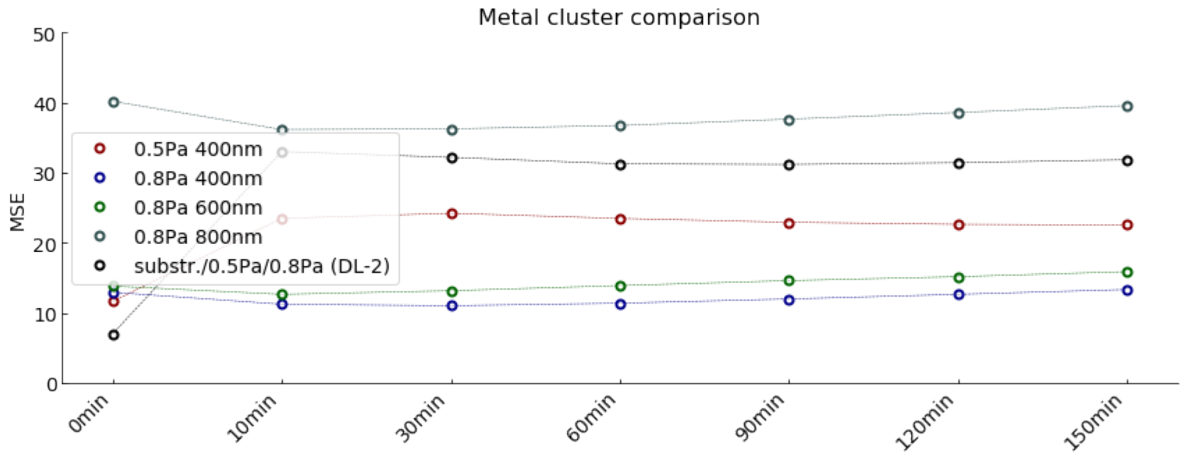

Figure B.6: MSE of all models

The MSE for all models from figures B.1 to B.5 are plotted in this graph.

B.2. Absorption coefficient

The absorption coefficients in figure B.7 are extracted from the modelled extinction coefficients and formula 2.21.

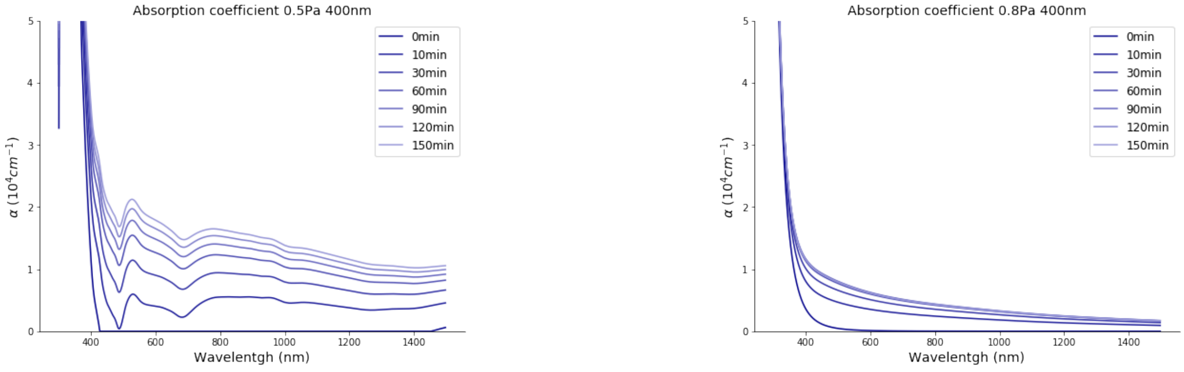

(a) Absorption coefficient 0.5Pa 400nm

(b) Absorption coefficient 0.8Pa 400nm

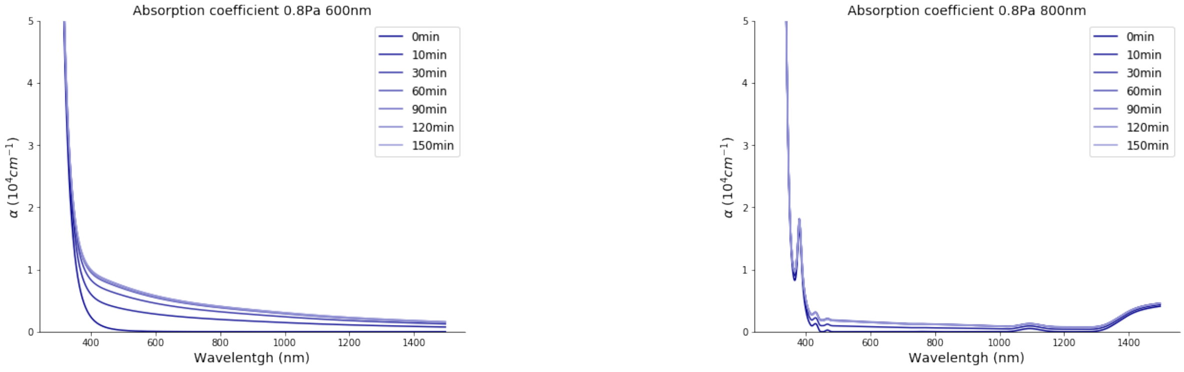

(c) Absorption coefficient 0.8Pa 600nm

(d) Absorption coefficient 0.8Pa 800nm

Figure B.7: absorption coefficient samples over wavelength

B.3. Measurement data

	10 min	**30 min**	**60 min**	**90 min**	**120 min**	**150 min**
YHx (%)	2.2	3.1	3.8	4.3	4.6	4.9
Voids (%)	1.2	1.7	2.1	2.3	2.6	2.7
ΔT (%)	36.3	43.5	48.0	50.3	51.8	53.0
$\Delta\alpha$-SE ($\cdot 10^5 m^{-1}$)	8.98	13.4	16.6	18.5	20.0	21.2
$\Delta\alpha$-Optical ($\cdot 10^5 m^{-1}$)	11.4	14.3	16.2	17.3	18.0	20.0

Table B.1: Spectroscopic ellipsometry and optical data used in section 4.3 for 0.5Pa 400nm sample.

	10 min	**30 min**	**60 min**	**90 min**	**120 min**	**150 min**
YHx (%)	0.6	0.9	1.0	1.1	1.1	1.1
Voids (%)	0.9	1.6	2.0	2.2	2.5	2.5
ΔT (%)	7.4	10.1	11.2	11.4	11.3	11.1
$\Delta\alpha$-SE ($\cdot 10^5 m^{-1}$)	2.89	4.21	4.97	5.20	5.14	3.03
$\Delta\alpha$-Optical ($\cdot 10^5 m^{-1}$)	2.36	3.38	3.79	3.89	3.93	3.90

Table B.2: Spectroscopic ellipsometry and optical data used in section 4.3 for 0.8Pa 400nm sample.

	10 min	**30 min**	**60 min**	**90 min**	**120 min**	**150 min**
YHx (%)	0.6	1.0	1.2	1.3	1.2	1.3
Voids (%)	0.9	1.5	2.0	2.4	2.5	2.8
ΔT (%)	12.7	16.6	17.7	17.9	17.8	17.6
$\Delta\alpha$-SE ($\cdot 10^5 m^{-1}$)	2.35	3.83	4.59	4.85	4.66	4.87
$\Delta\alpha$-Optical ($\cdot 10^5 m^{-1}$)	2.78	3.70	4.00	4.07	4.05	4.05

Table B.3: Spectroscopic ellipsometry and optical data used in section 4.3 for 0.8Pa 600nm sample.

	10 min	**30 min**	**60 min**	**90 min**	**120 min**	**150 min**
YHx (%)	0.4	0.6	0.6	0.6	0.6	0.6
Voids (%)	1.2	1.8	2.1	2.5	2.6	2.8
ΔT (%)	17.6	21.3	21.9	21.7	21.4	21.1
$\Delta\alpha$-SE ($\cdot 10^5 m^{-1}$)	0.70	1.29	1.34	1.38	1.30	1.28
$\Delta\alpha$-Optical ($\cdot 10^5 m^{-1}$)	2.56	3.17	3.30	3.26	3.23	3.28

Table B.4: Spectroscopic ellipsometry and optical data used in section 4.3 for 0.8Pa 800nm sample.

	10 min	**30 min**	**60 min**	**90 min**	**120 min**	**150 min**
YHx-0.8Pa (%)	1.9	2.1	2.2	2.3	2.3	2.3
YHx-boundary (%)	3.2	4.1	4.9	4.5	5.8	6.1
YHx-0.5Pa (%)	2.5	3.2	3.9	4.4	4.7	5.0
Voids-0.8Pa (%)	2.0	2.1	2.5	2.9	3.3	3.7
Voids-boundary (%)	1.6	1.7	2.0	2.4	2.8	3.3
Voids-0.5Pa (%)	0.0	0.3	0.8	1.0	1.1	1.2
ΔT (%)	39.3	46.5	50.5	52.7	54.1	55.2
$\Delta\alpha$-0.8Pa-SE ($\cdot 10^5 m^{-1}$)	7.42	8.11	8.53	8.76	8.91	8.91
$\Delta\alpha$-0.5Pa-SE ($\cdot 10^5 m^{-1}$)	11.9	15.0	18.1	20.1	21.6	22.8
$\Delta\alpha$-Optical ($\cdot 10^5 m^{-1}$)	8.89	11.1	12.5	13.2	13.8	14.2

Table B.5: Spectroscopic ellipsometry and optical data used in section 4.3 for DL-2 sample.

	10 min	**30 min**	**60 min**	**90 min**	**120 min**	**150 min**
YHx (%)	3.7	4.9	5.8	6.1	6.1	6.1
Voids (%)	1.8	2.7	3.5	4.0	4.3	4.5
ΔT (%)	36.6	42.8	46.8	49.5	51.2	52.7
$\Delta\alpha$-SE ($\cdot 10^5 m^{-1}$)	12.10	17.60	21.10	22.37	22.54	22.51
$\Delta\alpha$-Optical ($\cdot 10^5 m^{-1}$)	13.46	17.33	19.93	21.63	23.05	24.15

Table B.6: Spectroscopic ellipsometry and optical data used in section 4.3 for 0.5Pa single-layer sample of DL-2.

	10 min	**30 min**	**60 min**	**90 min**	**120 min**	**150 min**
YHx (%)	0.5	0.6	0.6	0.6	0.6	0.6
Voids (%)	1.2	1.8	1.8	1.5	1.4	1.3
ΔT (%)	6.3	7.3	7.3	7.3	7.3	7.3
$\Delta\alpha$-SE ($\cdot 10^5 m^{-1}$)	1.92	2.08	1.91	1.73	1.58	1.41
$\Delta\alpha$-Optical ($\cdot 10^5 m^{-1}$)	2.14	2.49	2.42	2.34	2.25	2.17

Table B.7: Spectroscopic ellipsometry and optical data used in section 4.3 for 0.8Pa single-layer sample of DL-2.

C

Appendix: Doppler Broadening Positron Annihilation Spectroscopy

C.1. Fractional contribution

Fractional distribution plots from our modelled DB-PAS measurements. Showing the contribution every layer has to the measured parameters. The plots for the measurements before illumination are given in the results.

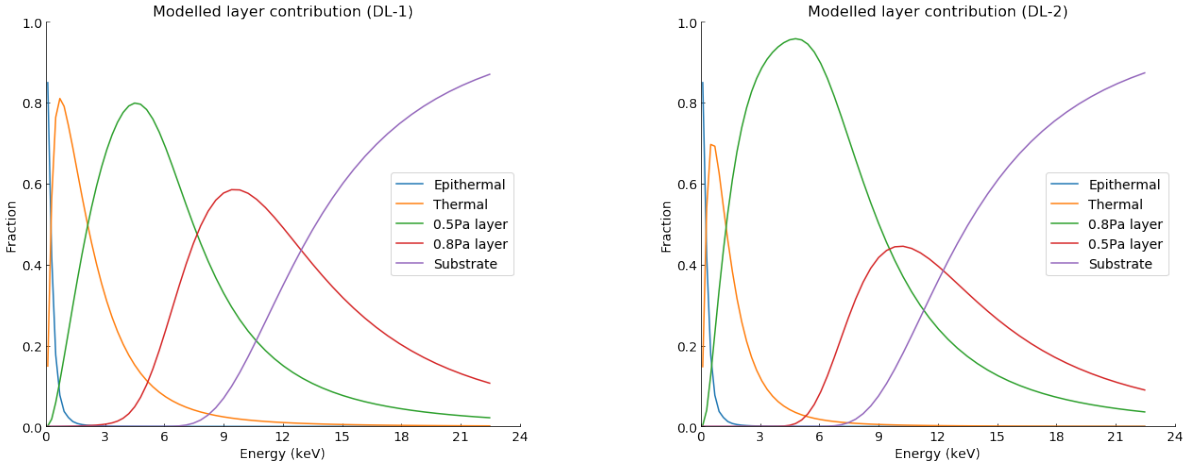

(a) Fraction distribution for DL-1 sample after illumination

(b) Fraction distribution for DL-2 sample after illumination

Figure C.1: Fraction distribution of positron annihilations in each layer contributing to parameters after illumination

C.2. Count rate measurements

Count rate per energy for all our DB-PAS measurements in section 5.4.1.

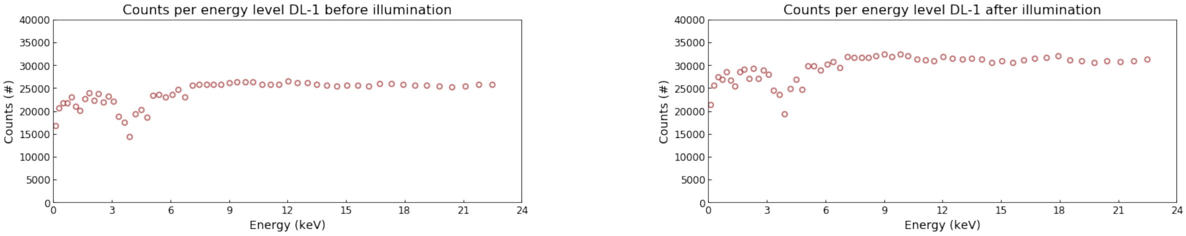

(a) Count rate for DL-1 sample before illumination

(b) Count rate for DL-1 sample after illumination

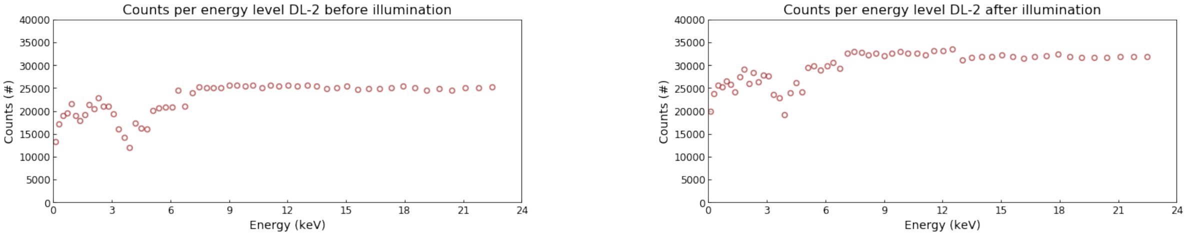

(c) Count rate for DL-2 sample before illumination

(d) Count rate for DL-2 sample after illumination

Figure C.2: Fraction distribution of positron annihilations in each layer contributing to parameters after illumination

D

Appendix: X-Ray Diffraction

D.1. Rietveld Refinement

The Rietveld refinement plots extracted from the XRD measurements. With the characteristic peaks for YOH indicated by a dotted line, along with the orientation.

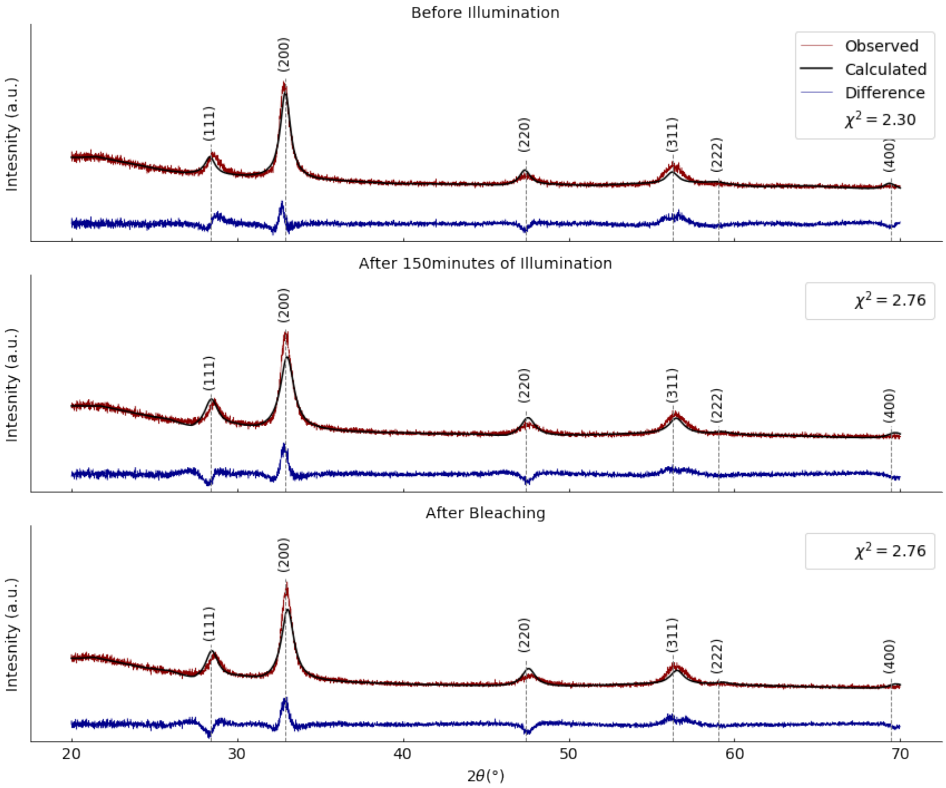

Figure D.1: XRD measurements 0.5Pa 400nm

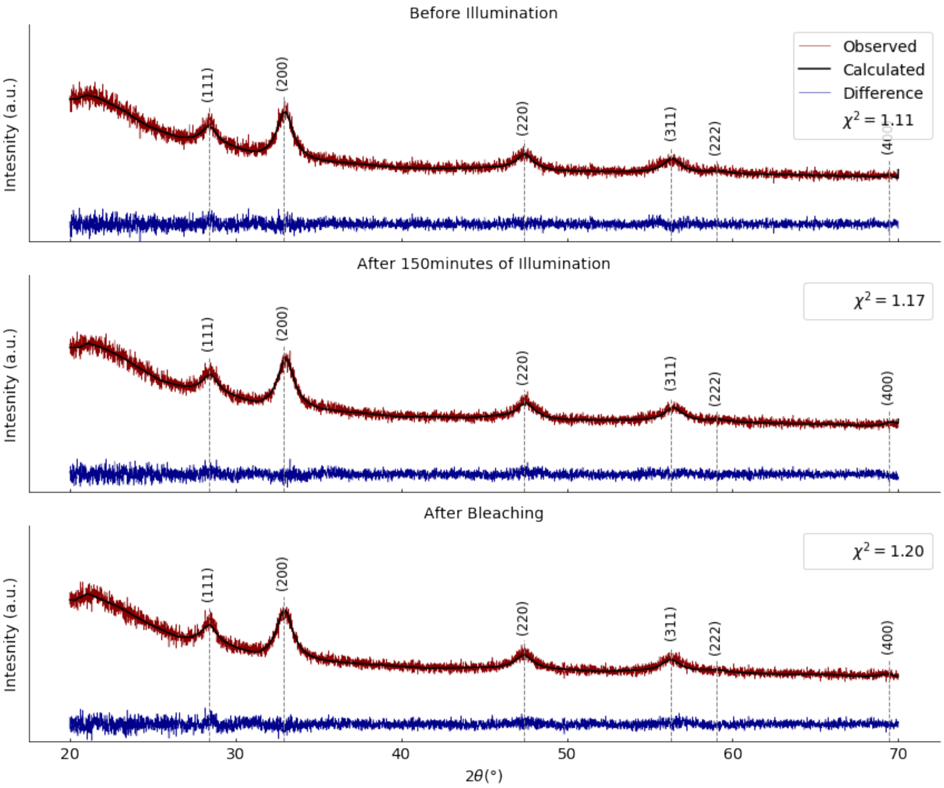

Figure D.2: XRD measurements 0.8Pa 400nm

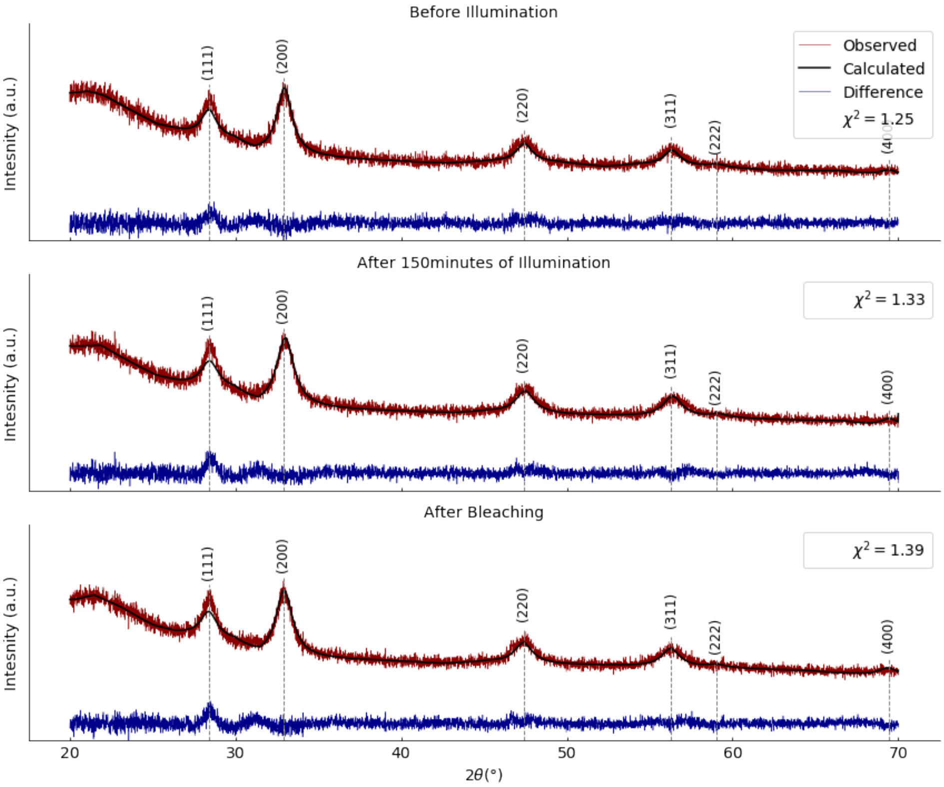

Figure D.3: XRD measurements 0.8Pa 600nm

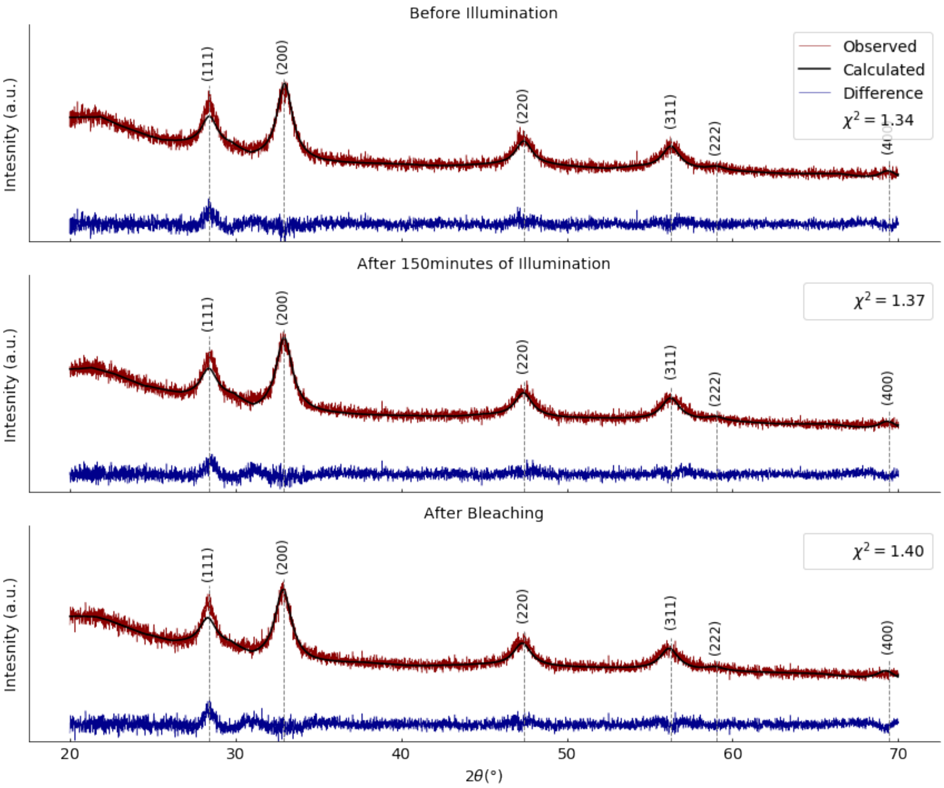

Figure D.4: XRD measurements 0.8Pa 800nm

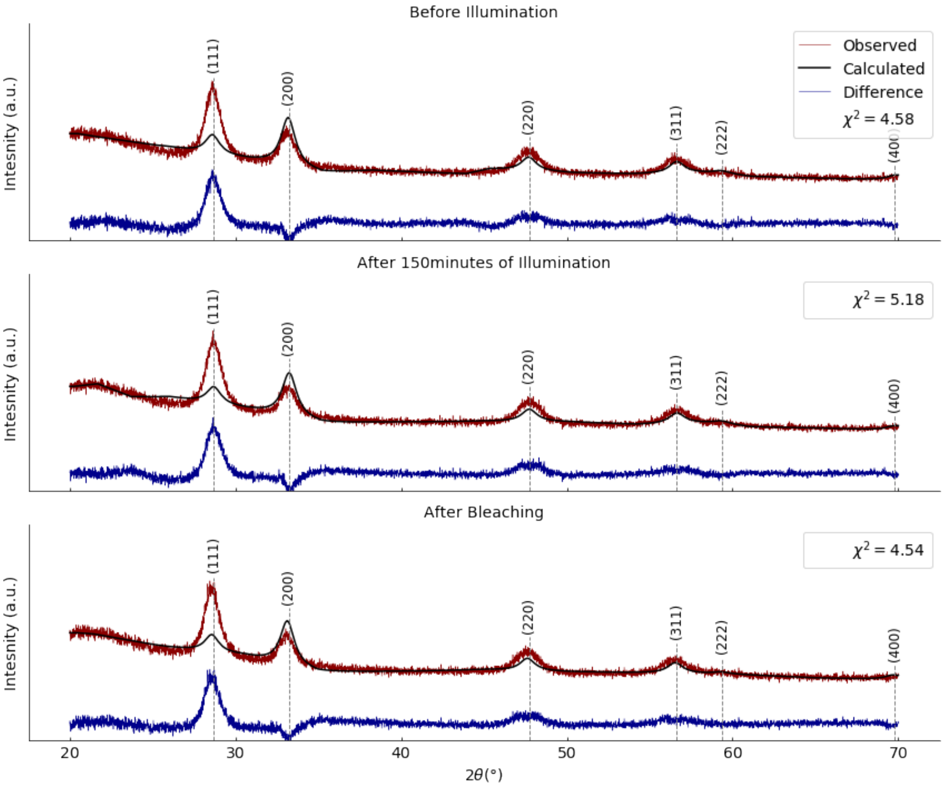

Figure D.5: XRD measurements substrate/0.8Pa/0.5Pa (DL-1)

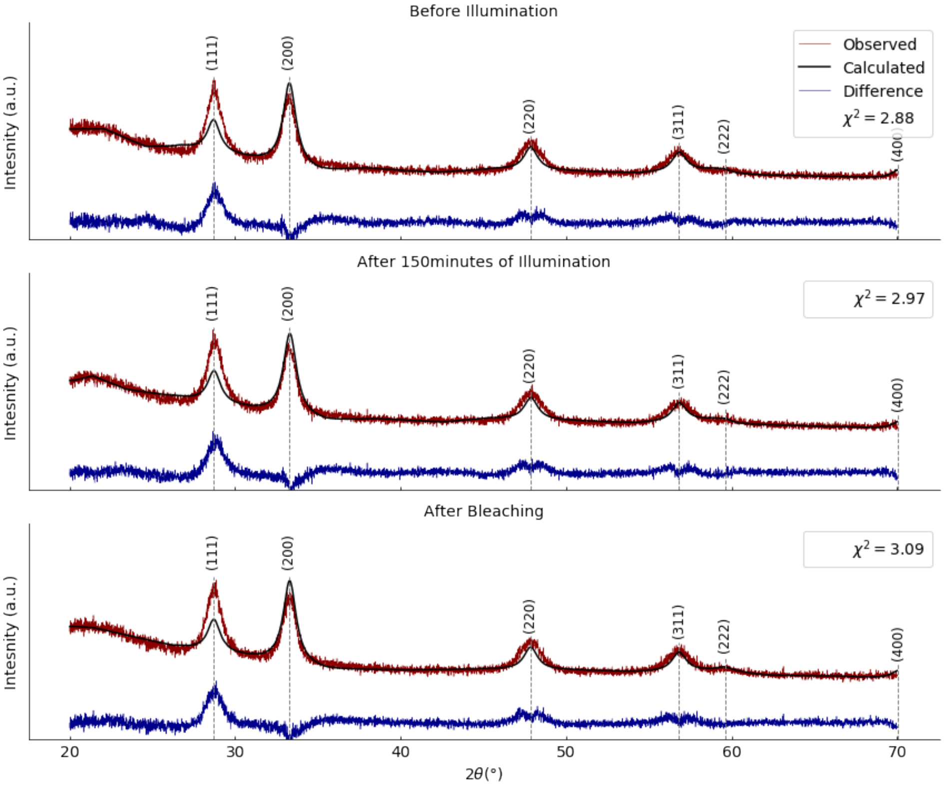

Figure D.6: XRD measurements substrate/0.5Pa/0.8Pa (DL-2)